DETERMINATION OF H_0 THROUGH MONITORING OF GRAVITATIONALLY LENSED QUASARS

A thesis submitted for the degree of

Doctor of Philosophy of Pondicherry University

Submitted by

S. Rathna Kumar

Department of Physics
Pondicherry University, Puducherry

April 2014

Declaration

I hereby declare that the material presented in this thesis entitled **"Determination of H_0 through monitoring of gravitationally lensed quasars"** is the result of investigations carried out by me at the Indian Institute of Astrophysics, Bangalore, under the supervision of Dr. C. S. Stalin. The results reported in this thesis are new and original, to the best of my knowledge, and has not been submitted in whole or part for the award of any Degree, Diploma, Associateship, Fellowship or other similar titles of any University or Institute. In keeping with the general practice of reporting scientific observations, due acknowledgement has been made whenever the work described is based on the findings of other investigators.

S. Rathna Kumar,
Indian Institute of Astrophysics,
Koramangala II Block,
Bangalore - 560034, India.

Certificate

This is to certify that the thesis entitled **"Determination of H_0 through monitoring of gravitationally lensed quasars"**, submitted by **Mr. S. Rathna Kumar** to **Pondicherry University, Puducherry, India** for the award of the degree of Doctor of Philosophy is absolutely based upon his own independent work under my supervision and that neither this thesis nor any part of it has been submitted for any Degree, Diploma, Associateship, Fellowship or other similar titles anywhere before.

I hereby forward the thesis for fulfilling the requirements for the award of the degree of Doctor of Philosophy in accordance with the regulations of Pondicherry University.

Dr. C. S. Stalin,
Indian Institute of Astrophysics,
Koramangala II Block,
Bangalore - 560034, India.

Acknowledgements

I thank my supervisor Dr. C. S. Stalin for providing me the opportunity to work on this thesis. Indian Institute of Astrophysics (IIA) is thanked for providing computational, library and all other facilities. Pondicherry University (PU) is thanked for allowing me to register my thesis under the MoU between IIA and PU. Board of Graduate Studies (BGS) of IIA is thanked for facilitating the registration process and all subsequent formalities. I thank Prof. T. P. Prabhu for initiating the photometric monitoring of gravitational lenses at the 2.0-m Himalayan Chandra Telescope (HCT) as early as October 2005, without which this thesis would not have been possible. Dr. Frederic Courbin and Prof. Georges Meylan are thanked for allowing me to use data obtained from other telescopes and also the data reduction and analysis tools developed within the framework of the COSmological MOnitoring of GRAvItational Lenses (COSMOGRAIL) collaboration. Dr. Malte Tewes is thanked for clarifying various aspects of the data reduction procedure and also numerous insightful discussions on the subtleties involved in curve-shifting analysis to determine time delays. I thank all my other collaborators as well and members of the Doctoral Committee for providing useful comments and suggestions at various stages. Prof. Leon Koopmans and Prof. Matthias Bartelmann are thanked for helpful discussions. I thank the numerous observers who contributed to the data from the Mercator and Maidanak telescopes, and I am grateful for the support provided by the staff at the Indian Astronomical Observatory, Hanle and CREST, Hosakote. Mr. Ravindra Pawase is specially thanked for collecting together the COSMOGRAIL monitoring data obtained using HCT till 2009. Dr. Chrisphin Karthick is thanked for being extremely helpful during my visits to PU. I acknowledge support from the Indo-Swiss Joint Research Programme (ISJRP). I thank my family members for their support and encouragement. Dr. Prashanth Mohan, Ms. P. Ramya, Mrs. G. Indu and all my other friends over the last five years are thanked for their invaluable help during various stages of this thesis work.

Publications

Refereed:

Eulaers, E.; Tewes, M.; Magain, P.; Courbin, F.; Asfandiyarov, I.; Ehgamberdiev, Sh.; **Rathna Kumar, S.**; Stalin, C. S.; Prabhu, T. P.; Meylan, G.; Van Winckel, H. **"COSMOGRAIL: the COSmological MOnitoring of GRAvItational Lenses. XII. Time delays of the doubly lensed quasars SDSS J1206+4332 and HS 2209+1914"** 2013, Astronomy & Astrophysics, 553, A121

Rathna Kumar, S.; Tewes, M.; Stalin, C. S.; Courbin, F.; Asfandiyarov, I.; Meylan, G.; Eulaers, E.; Prabhu, T. P.; Magain, P.; Van Winckel, H.; Ehgamberdiev, Sh. **"COSMOGRAIL: the COSmological MOnitoring of GRAvItational Lenses. XIV. Time delay of the doubly lensed quasar SDSS J1001+5027"** 2013, Astronomy & Astrophysics, 557, A44

Rathna Kumar, S.; Stalin, C. S.; Prabhu, T. P. **"H_0 from 11 well measured time-delay lenses"** *submitted to* Astronomy & Astrophysics (arXiv:1404.2920)

Non-refereed:

Malte Tewes; Frederic Courbin; Georges Meylan; Christopher S. Kochanek; Eva Eulaers; Nicolas Cantale; Ana M. Mosquera; Ildar Asfandiyarov; Pierre Magain; Hans Van Winckel; Dominique Sluse; **Rathna K. S. Keerthi**; Chelliah S. Stalin; Tushar P. Prabhu; Prasenjit Saha; Simon Dye **"COSMOGRAIL: Measuring Time Delays of Gravitationally Lensed Quasars to Constrain Cosmology"** 2012, The Messenger, 150, 49

Contents

1 Introduction **1**

1.1 A brief history of the universe 1

1.2 The Hubble constant 2

1.2.1 HST Key project 2

1.2.2 Supernovae and H_0 for the Equation of State (SH_0ES) program . . . 3

1.2.3 Wilkinson Microwave Anisotropy Probe and *Planck* 3

1.2.4 Megamaser Cosmology Project (MCP) 3

1.3 Gravitational lensing 4

1.4 The time delay method 5

1.4.1 Advantages of finding H_0 using the time delay method 7

1.4.2 H_0 from lensed quasars 7

1.5 The main goals of the present research work 8

2 Observations and Reductions **9**

2.1 Selection of the sample 9

2.1.1 SDSS J0806+2006 10

2.1.2 SDSS J1001+5027 10

2.2 Observations 13

2.2.1 Himalayan Chandra Telescope (HCT), India 13

2.2.2 Mercator telescope, Spain 13

2.2.3 Liverpool Robotic Telescope (LRT), Spain 13

2.2.4 Maidanak Observatory, Uzbekistan 14

2.2.5 Observations of SDSS J1001+5027 15

2.2.6 Observations of SDSS J0806+2006 15

2.3 Data Reduction 16

2.3.1 Preprocessing 16

2.3.2 Sky subtraction 18

2.3.3 Geometric Alignment 18

2.3.4 Photometry . . . 19
2.3.5 Normalisation . . . 20
2.3.6 Estimation of photometric error . . . 20
2.3.7 Combination of magnitudes in an epoch . . . 21
2.4 Light curves of SDSS J1001+5027 . . . 21
2.4.1 An apparent mismatch between the light curves . . . 25
2.5 Light curves of SDSS J0806+2006 . . . 25

3 Determination of time delays of SDSS J1001+5027 and SDSS J0806+2006 29
3.1 Background . . . 29
3.2 Methods of estimating time delays . . . 30
3.2.1 Cross-correlation method . . . 30
3.3 Difference-smoothing technique . . . 32
3.3.1 The uncertainty estimation procedure . . . 35
3.3.2 Application to SDSS J1001+5027 . . . 35
3.4 Time-delay measurement of SDSS J1001+5027 . . . 36
3.5 Time-delay measurement of SDSS J0806+2006 . . . 39

4 Homogeneous estimation of time delays of 24 gravitationally lensed quasars 42
4.1 Time delay determination . . . 42
4.1.1 Modification to the difference-smoothing technique . . . 43
4.1.2 Simulation of light curves . . . 43
4.1.3 Choice of free parameters . . . 45
4.1.4 Estimation of uncertainty . . . 45
4.2 Time delays of 24 gravitationally lensed quasars . . . 46

5 The Hubble constant from well-measured time-delay lenses 64
5.1 Sample selection . . . 64
5.2 H_0 from pixellated modelling of 12 gravitational lenses . . . 65

6 Conclusion and Future prospects 78
6.1 Time delay of SDSS J1001+5027 . . . 78
6.2 Time delay of SDSS J0806+2006 . . . 79
6.3 H_0 from well measured time-delay lenses . . . 80
6.4 Future prospects . . . 81

List of Figures

1.1 A schematic illustration of the time-delay method to infer H_0. 5

2.1 The 1.2-m Mercator Telescope. 11
2.2 The 2.0-m Liverpool Robotic Telescope (LRT). 11
2.3 The 1.5-m telescope of the Maidanak Observatory. 12
2.4 The 2.0-m Himalayan Chandra Telescope (HCT). 12
2.5 Distribution of the average observed FWHM and elongation ε of field stars in the images used to build the light curves of SDSS J1001+5027. 15
2.6 Distribution of the average observed FWHM and elongation ε of field stars in the images used to build the light curves of SDSS J0806+2006. 17
2.7 R-band image centered on SDSS J1001+5027. The image is the combination of the 210 best exposures from the Mercator telescope, for a total exposure time of 21 hours. 22
2.8 Two ways of modeling the light distribution for extended objects in SDSS J1001+5027 during the deconvolution process. 23
2.9 R-band light curves of the quasar images A and B in SDSS J1001+5027 from March 2005 to July 2011. 23
2.10 R-band image centered on SDSS J0806+2006. The image is the combination of the 58 best exposures from the HCT, for a total exposure time of 5 hours. 26
2.11 Simultaneous MCS deconvolution of HCT observations of SDSS J0806+2006. 27
2.12 R-band light curves of the quasar images A and B in SDSS J0806+2006 from September 2007 to April 2012. 27

3.1 Difference light curves of SDSS J1001+5027 as obtained by the new difference-smoothing technique. 33

3.2 Error analysis of the four time-delay measurement techniques, based on delay estimations on 1000 synthetic curves that mimic our SDSS J1001+5027 data. 36
3.3 Time-delay measurements of SDSS J1001+5027, following five different methods. 38
3.4 Difference light curve of SDSS J0806+2006 as obtained by the difference-smoothing technique. 39
3.5 Error analysis of the time-delay measurement using difference-smoothing technique, based on delay estimations on simulated light curves that mimic our SDSS J0806+2006 data. 40

4.1 *R*-band light curves of Q0142−100. 50
4.2 8 GHz light curves of JVAS B0218+357. 50
4.3 15 GHz light curves of JVAS B0218+357. 51
4.4 *R*-band light curves of HE 0435−1223. 51
4.5 *r*-band light curves of SBS 0909+532. 52
4.6 *I*-band light curves of RXJ 0911.4+0551. 52
4.7 *R*-band light curves of FBQ 0951+2635. 53
4.8 *r*-band light curves of Q0957+561. 53
4.9 *g*-band light curves of Q0957+561. 54
4.10 *R*-band light curves of SDSS J1001+5027. 54
4.11 Light curves of images A and B of SDSS J1004+4112. 55
4.12 *r*-band light curves of SDSS J1029+2623. 55
4.13 Light curves of HE 1104−1805. 56
4.14 *R*-band light curves of PG 1115+080. 56
4.15 *R*-band light curves of RX J1131−1231. 57
4.16 *R*-band light curves of SDSS J1206+4332. 57
4.17 *r*-band light curves of H1413+117. 58
4.18 15 GHz light curves of B1422+231. 58
4.19 *R*-band light curves of SBS 1520+530. 59
4.20 *I*-band light curves of CLASS B1600+434. 59
4.21 8.5 GHz light curves of CLASS B1600+434. 60
4.22 8.5 GHz light curves of CLASS B1608+656. 60
4.23 *R*-band light curves of SDSS J1650+4251. 61
4.24 8.6 GHz light curves of PKS 1830−211. 61
4.25 *R*-band light curves of WFI J2033−4723. 62

4.26 V-band light curves of HE 2149−2745. 62
4.27 R-band light curves of HS 2209+1914. 63

5.1 HST image of JVAS B0218+357. 65
5.2 The H_0 estimates and their 1σ uncertainties for 12 gravitational lenses and the best estimate of H_0 and its 1σ confidence interval, inferred through maximum-likelihood analysis. 66
5.3 HST image of HE 0435−1223. 71
5.4 HST image of RX J0911.4+0551. 71
5.5 HST image of Q0957+561. 72
5.6 HST image of SDSS J1004+4112. 73
5.7 HST image of HE 1104−1805. 74
5.8 HST image of PG 1115+080. 74
5.9 HST image of RX J1131−1231. 75
5.10 HST image of SBS 1520+530. 75
5.11 HST image of CLASS B1608+656. 76
5.12 HST image of WFI J2033−4723. 76
5.13 HST image of HE 2149−2745. 77
5.14 VLT image of SDSS J0806+2006 taken with adaptive optics. 77

List of Tables

2.1 Details of the lensed quasars monitored in this research study. 10
2.2 Summary of COSMOGRAIL observations of SDSS J1001+5027. 14
2.3 Summary of COSMOGRAIL observations of SDSS J0806+2006. 16

3.1 Time-delay measurements for SDSS J1001+5027. 37

4.1 Time delay measurements of 24 gravitationally lensed quasars. 48

5.1 Summary of input data to PixeLens and resulting H_0 estimates. 69

Chapter 1

Introduction

1.1 A brief history of the universe

Cosmology is the study of the universe as a whole, in particular its physical origin and evolution. According to the current understanding, the universe came into existence some 13.7 billion years ago in a Big Bang (a very hot and very dense state) and has expanded and cooled since then. After about 380,000 years, ions and electrons combined to form the first atoms. At the end of this recombination epoch, the universe became transparent to the photons that could then travel freely. The photons released after recombination formed a thermal radiation that is still observed today in the Cosmic Microwave Background (CMB), with a current temperature of 2.73 K and discovered by Penzias & Wilson (1965) . Matter then slowly assembled in the expanding universe. The first stars, galaxies and active galactic nuclei were formed and started to radiate photons, and thereby re-ionizing the universe. The large structures observed today were finally progressively created. There are three major observations that support the Big Bang theory, namely, CMB, primordial nucleosynthesis and the expansion of the universe.

In the current cosmological paradigm, only a handful of parameters seem necessary to describe the universe on the largest scales and its evolution over time. Testing this cosmological model requires a range of experiments, characterized by different sensitivities to these parameters. These experiments, or cosmological probes, are all affected by statistical and systematic errors and none of them on its own can uniquely constrain the cosmological models. This is due to the degeneracies inherent in each specific probe, implying that the probes become truly effective in constraining cosmology only when used in combination. The latest cosmology results by the *Planck* consortium beautifully illustrate this (Planck Collaboration 2013). In particular, the constraints obtained by *Planck* on the Hubble constant H_0, on the curvature Ω_k, and on the dark energy equation of state parameter w rely

mostly on the combination of measurements of the baryonic acoustic oscillations (BAO) with the observations of CMB.

1.2 The Hubble constant

In 1929, Edwin Hubble discovered that the universe was expanding. He noted that the recessional velocity v of a galaxy was roughly proportional to its distance d,

$$v = H_0 d. \tag{1.1}$$

Although he interpreted the redshifts of galaxies as due to Doppler effect, now they are understood to be arising from the expansion of space itself. Both interpretations lead to the same equation for the nearby universe and the equation stated above holds only for the nearby universe. The Hubble constant at the present epoch (H_0), the current expansion rate of the universe, is an important cosmological parameter. All extragalactic distances, age and size of the universe depend on H_0. It is also an important parameter in constraining the dark energy equation of state as well as used as input in many cosmological simulations (Freedman & Madore 2010; Planck Collaboration 2013). Therefore, precise estimation of H_0 is of utmost importance in cosmology.

Edwin Hubble initially estimated H_0 to be $\sim$500 km s^{-1} Mpc^{-1}, much higher than current estimates, due to errors in distance calibrations of the galaxies in his sample. Estimates of H_0 available in literature cover a wide range of uncertainties from $\sim$2% to $\sim$10% and the value ranges between 60 and 75 km s^{-1} Mpc^{-1}. We give below a brief summary of some of the most reliable measurements of H_0 that are known to date.

1.2.1 HST Key project

Following the launch of the Hubble Space Telescope (HST) in 1990, and the subsequent repair mission, substantial amounts of HST time were dedicated to measuring Cepheids in galaxies out to distances of 20 Mpc (Rowan-Robinson 2008), to try to measure the Hubble constant accurately and to give the different distance methods a secure and consistent calibration. One of the primary goals of the HST key project was to measure H_0 to an accuracy of $\pm$ 10%. Subsequently, they have measured Cepheid distances to 18 nearby spiral galaxies. Calibrating five secondary methods with the revised Cepheid distances, Freedman et al. (2001) found H_0 = 72 $\pm$ 3 (random) $\pm$ 7 (systematic) km s^{-1} Mpc^{-1} or H_0 = 72 $\pm$ 8 km s^{-1} Mpc^{-1}, by combining the systematic and random errors in quadrature.

1.2.2 Supernovae and H_0 for the Equation of State (SH_0ES) program

The Supernovae and H_0 for the Equation of State (SH_0ES) program was developed to improve upon the calibration of the luminosity of Type Ia Supernovae (SNe Ia) in order to better measure the Hubble constant. To achieve this, Cepheid variables in the host galaxies of a sample of SNe Ia were observed for few cycles of HST to calibrate the supernova magnitude-redshift relation. By improving upon the precision of the measurement of H_0 from Riess et al. (2009), the recent analysis by this program gives $H_0 = 73.8 \pm 2.4$ km s^{-1} Mpc^{-1}, which includes systematic errors (Riess et al. 2011).

1.2.3 Wilkinson Microwave Anisotropy Probe and *Planck*

The prediction of acoustic oscillations in CMB radiation by Sunyaev & Zeldovich (1970) and the subsequent measurements of these peaks by Wilkinson Microwave Anisotropy Probe (WMAP) is one of the successes of modern cosmology. Although measurements from the CMB power spectrum can be made to very high statistical precision, there are degeneracies which can limit the accuracy of the determination of the cosmological parameters such as the Hubble constant (Efstathiou & Bond 1999). From WMAP-9 year data, Hinshaw et al. (2013) report a value of $H_0 = 70.0 \pm 2.2$ km s^{-1} Mpc^{-1}. The subsequently launched *Planck* mission to study the CMB in more exquisite detail finds a value of $H_0 = 67.3 \pm 1.2$ km s^{-1} Mpc^{-1} (Planck Collaboration 2013). The value reported by *Planck* is highly model dependent. The data only measures the acoustic scale accurately, and the relation to underlying expansion parameters depends on the assumed cosmology. Even small changes in the model assumption can change H_0 noticeably.

1.2.4 Megamaser Cosmology Project (MCP)

Direct geometric distance measurements (that do not require a complex and uncertain ladder of calibration of "standard candles") to water masers in nuclear regions of galaxies provide a promising new and independent method for refining the value of H_0. The Megamaser Cosmology Project (MCP) is a systematic effort in this direction aimed at discovering suitable H_2O megamasers and determining their distances, and thereby measuring H_0 accurate to a few percent . From observations of H_2O maser in the galaxy UGC 3789, Reid et al. (2013) find $H_0 = 68.9 \pm 7.1$ km s^{-1} Mpc^{-1}. The project in the future will be able to observe more megamaser galaxies with the upcoming Square Kilometer Array (SKA).

Although the values of H_0 obtained from different methods are consistent with each other within 2σ given the current level of precision, all of the above methods of determina-

tion of H_0 suffer from systematic uncertainties and therefore as the measurements increase in precision, multiple approaches based on different physical principles need to be pursued to measure its value so as to be able to identify unknown systematic errors present in any given approach. Apart from the methods discussed above for the determination of H_0, there is yet another independent method, which is based on the phenomenon of gravitational lensing.

1.3 Gravitational lensing

Gravitational lensing refers to the deflection of light in a gravitational field. As a consequence of Einstein's General Theory of Relativity, it follows that light passing at a distance r from a point mass M gets deflected by an angle θ given by

$$\theta = \frac{4GM}{rc^2}, \tag{1.2}$$

where G is the gravitational constant and c is the speed of light. One of the first confirmations of General Relativity was the measurement of displacement of stars observed near the solar limb from their true positions during a total solar eclipse in 1919 by a team led by Arthur Eddington. Orest Chwolson in 1924 was the first to consider the formation of two images of a background star due to gravitational lensing by a foreground star. In 1936, Albert Einstein working on the same problem concluded that there is very little chance of observing this phenomenon since the angular seperation of images resulting from stellar-mass lenses is too small to be resolved by optical telescopes. Fritz Zwicky in 1937 pointed out that in case of galaxies acting as gravitational lenses, the angular seperation of the images of a background source will be large enough so that the images can be resolved by optical telescopes. The phenomenon of formation of multiple distorted and magnified images of a background luminous source by a foreground galaxy or galaxy cluster is known as strong gravitational lensing. The first case of strong gravitational lensing was observed by Walsh et al. (1979). They found the quasar QSO 0957+561 to be lensed into two images A and B seperated by $5.7''$ by a foreground galaxy, which resides in a cluster.

The two other regimes of gravitational lensing are

- weak gravitational lensing, wherein a distorted image of a background source is seen but not multiple imaging and

- microlensing, which happens in case of a stellar-mass lens when the resulting image separations are of the order of microarcseconds and hence the individual images are

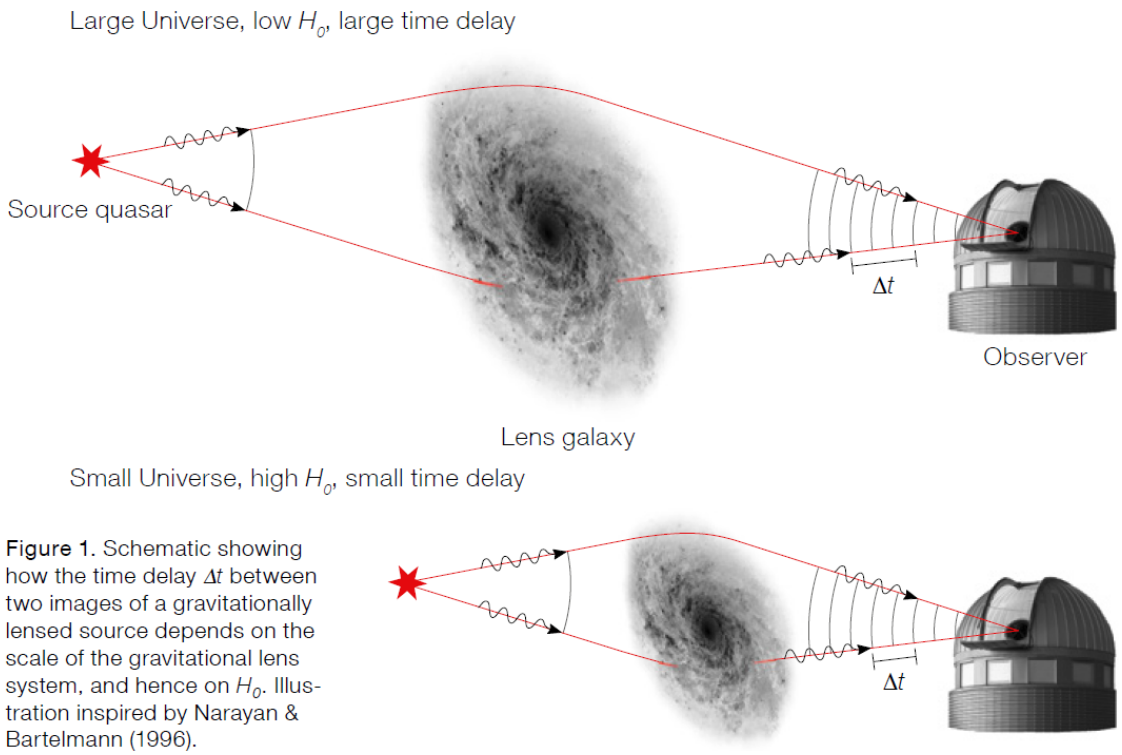

Figure 1. Schematic showing how the time delay Δt between two images of a gravitationally lensed source depends on the scale of the gravitational lens system, and hence on H_0. Illustration inspired by Narayan & Bartelmann (1996).

Figure 1.1: A schematic illustration of a quasar lensed into two images by a foreground galaxy. By measuring the time delay between the images, it is possible to infer the scale of the universe and thus H_0. (Figure credit: Tewes et al. 2012)

not resolvable, but the relative motion of the source and the lens causes the observed brightness of the background source to vary in time.

For a detailed introduction on gravitational lensing, the reader is referred to Narayan & Bartelmann (1996).

1.4 The time delay method

Strong gravitational lensing offers a valuable yet inexpensive complementary probe to independently constrain some of the cosmological parameters, through the measurement of the so-called time delays in quasars strongly lensed by a foreground galaxy (Refsdal 1964). The principle of the method is the following. The travel times of photons along the distinct optical paths forming the multiple images are not identical. This situation is illustrated in Fig. 1.1. These travel-time differences, called the time delays, depend on the geometrical differences between the optical paths, which contain the cosmological information, and on

the potential well of the lensing galaxy(ies). In practice, time delays can be measured from photometric light curves of the multiple images of lensed quasar: if the quasar shows photometric variations, these are seen in the individual light curves at epochs separated by the time delay.

The light travel time along the ray of a lensed image differs from that along an unperturbed ray from the source to the observer. This time delay has two components - geometrical and gravitational.

$$\tau(\vec{\theta},\vec{\beta}) = \frac{(1+z_L)}{c}\frac{D_L D_S}{D_{LS}}\left(\frac{1}{2}(\vec{\theta}-\vec{\beta})^2 - \psi(\vec{\theta})\right), \tag{1.3}$$

where $\vec{\beta}$ is the true angular position of the source and $\vec{\theta}$ is the apparent angular position of the source (Wambsganss 1998). D_L, D_S, and D_{LS} are the angular diameter distances to the lensing mass, to the source, and between the lensing mass and the source respectively. z_L is the lens redshift and $\psi(\vec{\theta})$ is the effective lensing potential (Narayan & Bartelmann 1996). The effective time delay between a pair of lensed images can be expressed in a simple form as

$$\Delta t = \frac{1}{H_0} F(z_L, z_S) G(lens\ mass\ profile) \tag{1.4}$$

The factors F and G are both dimensionless. F depends on the redshifts of the lens and the source and is very well constrained. F also depends on Ω_m and Ω_Λ but only at the level of a few percent. G depends on the mass distribution of the lens and is the only non-negligible systematic uncertainty (Courbin et al. 2002). The above equation clearly shows that the two major sources of uncertainty in the determination of H_0 using lensed quasars are the uncertainty of the time delay and the uncertainty of the lens mass profile.

A precise and accurate measurement of such a time delay, in combination with a well-constrained model for the lensing galaxy, can be used to constrain cosmology in a way which is very complementary to other cosmological probes (see, e.g., Linder 2011). A recent and remarkable implementation of this approach can be found in Suyu et al. (2013a) that uses the time-delay measurements from Tewes et al. (2013b). We note, however, that to obtain a robust cosmological inference from this time-delay technique, particular attention must be paid to any possible lens model degeneracies (Schneider & Sluse 2013a; Suyu et al. 2013b; Schneider & Sluse 2013b). Also, precise measurement of time delays is quite non-trivial, requiring several years of regular telescope monitoring.

1.4.1 Advantages of finding H_0 using the time delay method

1. The time delay method is based on simple geometry and the well-established physics of General Relativity. It does not involve any complex astrophysics such as exploding stars.

2. The technique allows a one-step distance determination free from calibrations associated with standard candles. Also, the time delays are primarily sensitive to H_0 and less sensitive to other cosmological parameters.

3. Measuring H_0 from gravitational lens time delays is very cheap compared to other H_0 estimation programmes. With improvements in image processing and time delay estimation techniques, accurate time delay values can be obtained by carrying out regular monitoring using 1-m class telescopes on the ground. Only for follow-up observations to constrain the lens model, like determining the redshift of the lensing galaxy, accurate measurement of astrometry, etc., we need large telescopes, that too for a small amount of time.

4. Apart from providing time delays, the monitoring light curves can be used for a variety of other studies as well, for example, probing the structure of the background quasar. The monitoring light curves have a high "legacy" value for quasar microlensing studies.

5. This method measures H_0 at truly cosmological distances.

1.4.2 H_0 from lensed quasars

Some of the recent estimates of H_0 using the time delay method are discussed below.

– An extensive analysis of the quadruple lens system B1608+656 has been carried out by Suyu et al. (2010). They have used deep HST/ACS imaging in F606W and F814W filters, accurate measurement of the stellar velocity dispersion using the Low-Resolution Imaging Spectrometer (LRIS) on Keck, and a more detailed treatment of the lens environment using a combination of ray tracing through cosmological N-body simulations along with number counts in the field of the quasar to help break the mass-sheet degeneracy. Fixing the cosmological parameters to $\Omega_m = 0.3$, $\Omega_\Lambda = 0.7$ and $w = -1$, they find $H_0 = 70.6^{+3.1}_{-3.1}$ km s^{-1} Mpc^{-1}.

– Suyu et al. (2013a) have done a blind analysis of the quadruple gravitational lens RXJ1131−1231. This quasar discovered by Sluse et al. (2003) has a redshift of z

= 0.658. The lens has a spectroscopic redshift of $z = 0.295$ (Sluse et al. 2003). Using accurate time delay measurements from COSMOGRAIL collaboration Tewes et al. (2013b), imaging observations from HST, velocity dispersion measurements of the lens galaxy using the LRIS on Keck and characterization of the line-of-sight structures via observations of the lens environment and ray tracing through the Millennium Simulation, Suyu et al. (2013a) obtain a value of $H_0 = 78.7^{+4.3}_{-4.5}$ km s^{-1} Mpc^{-1}.

– Saha et al. (2006) have used a sample of 10 lenses. They simulatenously modelled them with the additional requirement of a shared value of the Hubble parameter across all lenses using the PixeLens code of Saha & Williams (2004). They found $H_0 = 72^{+8}_{-11}$ km s^{-1} Mpc^{-1}.

– Paraficz & Hjorth (2010) did a simultaneous analysis of 18 gravitational lenses for which time delays were reported that time. For each of these lenses using the non-parametric pixellated simultaneous modelling using PixeLens (Saha & Williams 2004), with shared Hubble constant they find $H_0 = 66^{+6}_{-4}$ km s^{-1} Mpc^{-1}, for a flat universe with $\Omega_m = 0.3$ and $\Omega_\Lambda = 0.7$.

1.5 The main goals of the present research work

From the above brief overview of the status of this subject, it is evident that the desire to find an independent estimate of H_0 from lensed quasar monitoring is achievable. Any progress in this direction will be contingent upon carrying out photometric monitoring campaign with good time resolution for a large sample of lensed quasars and improvement in the lens models. High precision time delays are now achievable through regular monitoring using 1-m class telescopes and good lens models too can now be constructed, thereby bringing down the error in H_0. The key objectives of this present thesis work are

1. to get accurate estimates of time delays for more gravitational lens systems by systematic and long term optical monitoring observations, careful analysis using a proper time delay estimator that takes into account the various systematics involved and

2. to get an independent estimate of H_0 using a large sample of lensed systems through a homogeneous analysis procedure.

These questions will be addressed in the remainder of this thesis.

Chapter 2

Observations and Reductions

The starting point of the present research program was the ongoing Indian participation in the COSMOGRAIL[1] (COSmological MOnitoring of GRAvItational Lenses) project, which aims to measure time delays for most known lensed quasars. So far, only a few quasar time delays have been measured convincingly, from long and well-sampled light curves. The international COSMOGRAIL collaboration is changing this situation by measuring accurate time delays for a large number of gravitationally lensed quasars, from optical light curves obtained with telescopes in both the hemispheres (Tewes et al. 2012). The goal of COSMOGRAIL is to reach an accuracy of less than 3%, including systematics, for most of its targets.

The strategy followed in this present work was to carry out densely sampled R-band monitoring of a sample of gravitationally lensed quasars using charge coupled devices (CCDs) as the detector.

2.1 Selection of the sample

Sample selection is crucial for photometric monitoring observations of gravitationally lensed quasars. For observations of this kind, the accuracy of the photometry will depend on the brightness of the quasars, as well as the separation of the lensed quasar images. Image separation is given important consideration here, because it is difficult to get good photometry if the seeing of the site is larger compared to the image separation. Thus, considering (i) brightness of the quasar (ii) image separation and (iii) suitability of getting long term observations spreading over 5 years, we have selected two doubly imaged gravitationally lensed quasars for this thesis, namely SDSS J0806+2006 and SDSS J1001+5027.

[1] http://www.cosmograil.org/

Table 2.1: Details of the lensed quasars monitored in this research study.

Object name	RA. (2000)	Dec. (2000)	Redshifts	R mag	Separation
SDSS J0806+2006	08:06:23.70	+20:06:31.90	$z_s = 1.537^{(a)}$	$\sim$19	1.40″
			$z_l = 0.573^{(b)}$		
SDSS J1001+5027	10:01:28.61	+50:27:56.90	$z_s = 1.838^{(c)}$	$\sim$18	2.86″
			$z_l = 0.415^{(d)}$		

References. $^{(a)}$ Inada et al. (2006); $^{(b)}$ Eigenbrod et al. (2007); $^{(c)}$ Oguri et al. (2005); $^{(d)}$ Inada et al. (2012).

2.1.1 SDSS J0806+2006

SDSS J0806+2006 was discovered as a doubly imaged gravitational lens system by Inada et al. (2006). This was initially selected from the SDSS spectroscopic quasar catalog as a lens candidate and was confirmed by detailed optical and IR imaging observations. High resolution spectroscopic observations, using the Keck II telescope, confirmed the gravitationally lensed nature of the source. SDSS J0806+2006 has a source redshift of $z_s = 1.540$, and the two quasar images are separated by 1.40″. This source is lensed by a galaxy at $z_l = 0.573$, as evident from its magnitude, colors and the presence of a Mg II absorption in its spectrum. This quasar is found in a denser galactic environment, suggesting that the lensing galaxy is part of a small group.

2.1.2 SDSS J1001+5027

SDSS J1001+5027 was discovered as a gravitational lens system by Oguri et al. (2005).This was discovered in a lens search programme using SDSS data. This quasar at a source redshift of $z_s = 1.838$ has two lensed images separated by 2.86″. Two extended objects, namely G1 and G2 are found in the vicinity of the lensed images, and these objects have colors consistent with early type galaxies with redshift $0.2 < z < 0.5$. As the galaxy G1 is nearly co-linear with the two quasar images, it is likely to be the main contributor to the lens potential. Using the GMOS instrument on Gemini North telescope, Inada et al. (2012) find a spectroscopic redshift of $z_l = 0.415$ for the lensing galaxy. The details of these two lens systems are summarised in Table 2.1.

Figure 2.1: The 1.2-m Mercator Telescope. (Photo courtesy: Tyl Dermine http://www.astro.uni-bonn.de/~dermine/Mercator Telescope.html)

Figure 2.2: The 2.0-m Liverpool Robotic Telescope (LRT). (Photo courtesy: COSMOGRAIL http://obswww.unige.ch/~tewes/cosmograil/public/telescopes.php)

Figure 2.3: The 1.5-m telescope of the Maidanak Observatory. (Photo courtesy: COSMO-GRAIL http://obswww.unige.ch/~tewes/cosmograil/public/telescopes.php)

Figure 2.4: The 2.0-m Himalayan Chandra Telescope (HCT). (Photo courtesy: Indian Institute of Astrophysics http://www.iiap.res.in/files/uploads/brochure/brochure_2006.html)

2.2 Observations

The imaging observations reported in this work come from four different telescopes. In order to be able to accurately assess the photometric errors, three or more dithered images were obtained during each epoch of observation. The size of the dithering box used was $10''$ - $20''$. All observations were carried out in R-band considering the maximal response of CCD in that waveband.

2.2.1 Himalayan Chandra Telescope (HCT), India

Most of the data supporting this thesis derives from observations made using the 2-m Himalayan Chandra Telescope (HCT) (Fig. 2.4), which is a Ritchey-Chretien system with an f/9 beam. The telescope is located at the Indian Astronomical Observatory (IAO), Hanle (India) at an altitude of 4500 metres, and remotely operated via a dedicated satellite link from the Centre for Research in Education Science and Technology (CREST), Hosakote, which is a field-station of the Indian Institute of Astrophysics (IIA), Bangalore. The detector used was the Himalayan Faint Object Spectrograph and Camera (HFOSC). For the observations reported here, the central 2048 $\times$ 2048 pixel^2 region of the CCD in HFOSC was used. Each pixel of size 15 microns corresponds to $0.296''$ on the sky. The CCD covers about $10' \times 10'$ region on the sky. The readout noise and gain are 4.8 e^- and 1.22 e^-/ADU respectively. An exposure time of 300 seconds was used to obtain each dithered image.

2.2.2 Mercator telescope, Spain

This is a 1.2-m telescope (Fig. 2.1) located at the Roque de los Muchachos Observatory in La Palma, Canary Islands, Spain. It was built by the Observatory of the Geneva University, but is operated by the Instituut voor Sterrenkunde, Katholieke Universiteit Leuven, Belgium. Mercator is equipped with a 2048 $\times$ 2048 CCD camera, which has a $6.5' \times 6.5'$ field of view and $0.19''$ pixels. The read out noise and gain of the CCD are 4.5 e^- and 0.93 e^-/ADU respectively. Each dithered image was obtained with 360 seconds of integration.

2.2.3 Liverpool Robotic Telescope (LRT), Spain

This is a 2-m Cassegrain telescope with Ritchey-Cretien hyperbolic optics on an alt-azimuth mount. This telescope is fully robotic and is operated by the Astrophysics Research Institute of Liverpool John Moores University in England. The observations reported here were carried out using the RATCam camera consisting of 2048 $\times$ 2048 pixel^2

Table 2.2: Summary of COSMOGRAIL observations of SDSS J1001+5027.

Telescope Diameter	Camera FoV Pixel scale	Monitoring period	Epochs	Exp. time$^{(a)}$	Sampling$^{(b)}$
Mercator 1.2 m	MEROPE $6.5' \times 6.5'$ $0.190''$	2005 Mar – 2008 Dec	239	5×360 s	3.8 (2.0) d
HCT 2.0 m	HFOSC $10' \times 10'$ $0.296''$	2005 Oct – 2011 Jul	143	4×300 s	9.5 (6.1) d
Maidanak 1.5 m	SITE $8.9' \times 3.5'$ $0.266''$	2005 Dec – 2008 Jul	41	7×180 s	5.9 (4.1) d
Maidanak 1.5 m	SI $18.1' \times 18.1'$ $0.266''$	2006 Nov – 2008 Oct	20	6×600 s	12.6 (9.5) d
Combined		2005 Mar – 2011 Jul	443	201.5 h	3.8 (1.9) d

Notes. $^{(a)}$ The exposure time is given by the number of dithered exposures per epoch and their individual exposure times. $^{(b)}$ The sampling is given as the mean (median) number of days between two consecutive epochs, excluding the seasonal gaps.

CCD covering $4.6' \times 4.6'$ of the sky. Each dithered image was obtained with an exposure time of 300 seconds.

2.2.4 Maidanak Observatory, Uzbekistan

We have also used the 1.5 telescope of the Maidanak Observatory in Pamir Alai, Uzbekistan, and operated by the Uzbekistan Academy of Science in Tashkent. We have used two CCDs for observations. During the period 2005 December to 2008 July we used the SITE CCD camera which has a pixel scale of $0.266''$ and covers a total area in the sky of $8.9'$ $\times$ $3.5'$. Simlarly, during the period 2006 November $-$ 2008 October, the SI CCD camera was used, which has a pixel scale of $0.266''$ and covers an area of $18.1' \times 18.1'$ in the sky. When using the SITE chip, the dithered image was obtained with an exposure time of 180 seconds, but for the SI chip, each dithered image was acquired with an integration time of 600 seconds.

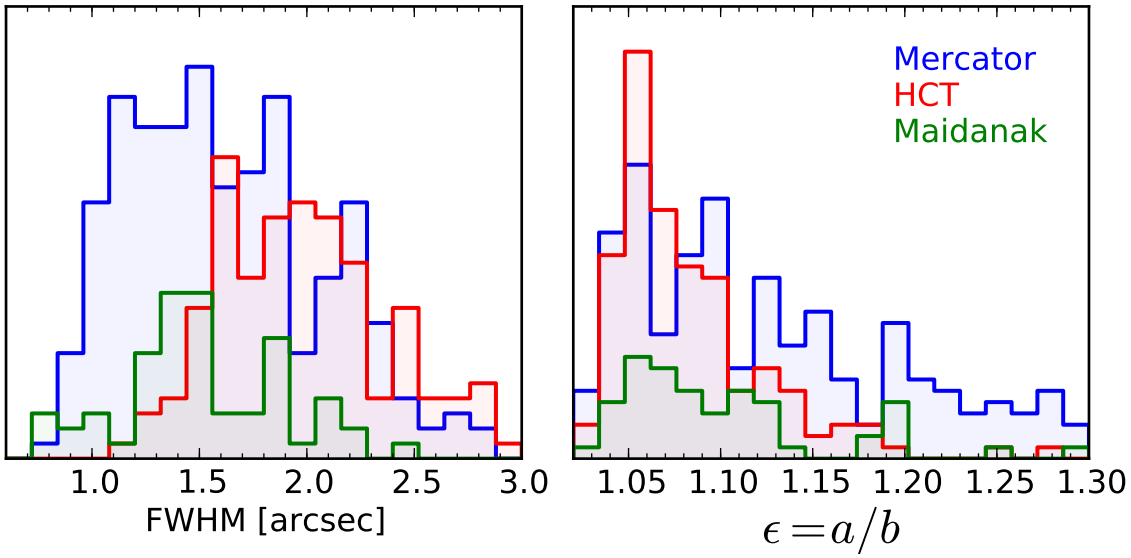

Figure 2.5: Distribution of the average observed FWHM and elongation ε of field stars in the images used to build the light curves of SDSS J1001+5027.

2.2.5 Observations of SDSS J1001+5027

We monitored SDSS J1001+5027 in the R band for more than six years, from March 2005 to July 2011, with three different telescopes: the 1.2-m Mercator Telescope, the 1.5-m telescope of the Maidanak Observatory and the 2-m HCT. Table 2.2 details our monitoring observations. In total we obtained photometric measurements for 443 independent epochs, with a mean sampling interval below four days. Each epoch consists of at least three, but mostly four or more, dithered exposures. Figure 2.5 summarizes the image quality of our data. The COSMOGRAIL collaboration has now ceased the monitoring of this target.

2.2.6 Observations of SDSS J0806+2006

We have been monitoring SDSS J0806+2006 in the R band for more than six years, since September 2007, with two different telescopes: the 2.0-m LRT and the 2.0-m HCT. Although the 1.5-m telescope of the Maidanak Observatory was involved in the monitoring in the beginning, the epochs of observation obtained were too few to be useful. In this thesis, we present the light curves using data obtained till April 2012. Table 2.3 details our monitoring observations. In total we obtained photometric measurements for 153 independent epochs, with a mean sampling interval of about a week. Each epoch consists of at least three, but mostly four or more, dithered exposures. Figure 2.6 summarizes the image quality of our data. We are continuing observations of this target using HCT.

Table 2.3: Summary of COSMOGRAIL observations of SDSS J0806+2006 used in this thesis.

Telescope Diameter	Camera FoV Pixel scale	Monitoring period	Epochs	Exp. time$^{(a)}$	Sampling$^{(b)}$
HCT 2.0 m	HFOSC $10' \times 10'$ $0.296''$	2007 Oct – 2012 Apr	120	4×300 s	9.2 (7.0) d
LRT 2.0 m	RATCam $4.6' \times 4.6'$ $0.135''$	2007 Sep – 2008 Nov	33	5×300 s	9.6 (6.9) d
Combined		2007 Sep – 2012 Apr	153	58.8 h	7.4 (5.1) d

Notes. $^{(a)}$ The exposure time is given by the number of dithered exposures per epoch and their individual exposure times. $^{(b)}$ The sampling is given as the mean (median) number of days between two consecutive epochs, excluding the seasonal gaps.

2.3 Data Reduction

The following sections briefly describe the steps involved in the generation of lightcurves of the quasar images starting from the raw telescope data frames.

2.3.1 Preprocessing

Preprocessing is a set of steps carried out in order to remove the signatures of the instrument present in the observed data frames. This was carried out using standard tasks in IRAF.[2] In the following, we briefly outline the preprocessing steps needed for data frames from HFOSC instrument in the 2.0-m HCT. Similar procedures were used for data from other telescopes as well.

Bias subtraction

Bias in the context of CCDs is the term for the signal added before digitization, in order to avoid the noise creating negative values at the readout of a pixel. This bias has, in principle an absolutely constant value which gets added to all pixels. In practice, however, it

[2]IRAF is the Image Reduction and Analysis Facility, a general purpose software system for the reduction and analysis of astronomical data. IRAF is written and supported by the IRAF programming group at the National Optical Astronomy Observatories (NOAO) in Tucson, Arizona. NOAO is operated by the Association of Universities for Research in Astronomy (AURA), Inc. under cooperative agreement with the National Science Foundation.

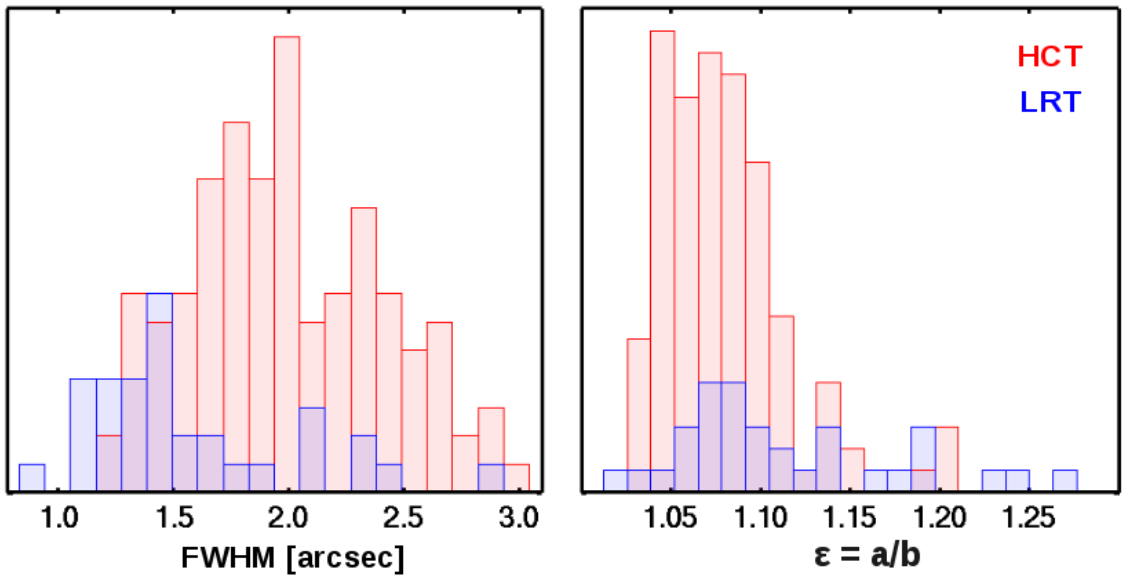

Figure 2.6: Distribution of the average observed FWHM and elongation ε of field stars in the images used to build the light curves of SDSS J0806+2006.

is affected by noise and also, the level varies due to temperature and other effects on the electronics and it may not be necessarily uniform across the chip. For our observations, we adopted the following procedure. The bias images in and around a given night were median-combined to create the master-bias for that night. This master-bias is used to estimate the bias level which is subtracted from all the image frames i.e. both target frames and flat field frames in that night.

Dark subtraction

This is the second step needed in any CCD image reduction. This is also an additive signal present in any CCD image. However, as the CCDs used in our observations are cryogenically cooled, the rate of accumulation of thermal charge is negligible and thus dark subtraction is not carried out for the observations reported here.

Flat fielding

This is the third and crucial step of image processing. This needs to be done with great care as the final sensitivity of the measurements critically depends on it. One of the important characteristics of CCDs is that each pixel generally behaves as a linear device, but with somewhat different quantum efficiency for different pixels. Thus, to treat the whole array of pixels as a single entity, the various pixel gains need to be normalised relative to one

another. To accomplish this, several image frames of the flat sky were taken during twilight. The bias-subtracted flats in and around a given night are median-combined to create the master-flat for that night. The bias-subtracted object frames in a night are then divided by the normalised master-flat for that night. This will remove the pixel to pixel sensitivity variations in the object frames, and produce clean object frames devoid of any instrumental signatures.

Cosmic ray removal

The final step in preprocessing is identifying and removing the cosmic rays in the images. The cosmic rays can be differentiated from the objects due to the following reason. A cosmic ray is a single pixel event, whereas an object is spread over many pixels, according to the seeing. However we do not remove the cosmic rays in the preprocessing stage itself. They are identified and masked later in the processing stage.

2.3.2 Sky subtraction

When acquiring an image of the field containing the target of interest, the CCD, apart from collecting photons from the target, they also collect photons from the background sky. It is therefore necessary to estimate and remove the background counts from the image frame before determining the flux from the source. The background sky can vary from frame to frame, as it depends on the exposure time, the transparency of the sky, presence and phase of the moon, etc. Thus to effectively remove the photons coming from sky background, a map of the background is created using SExtractor (Bertin & Arnouts 1996), which is then subtracted from each image data frame.

2.3.3 Geometric Alignment

Before doing photometry on the data frames, they need to be aligned together. For this purpose, a reference data frame is chosen from among the best seeing data frames after making sure that it does not have any problem. Stars are then chosen from all over the field and their positions in the reference frame are noted down. Their corresponding positions in a given data frame are used to compute the geometric shift and rotation which is to be applied to the data frame in order to align it with the reference data frame. Geometric alignment of all the data frames was accomplished using the Python package 'alipy'[3], which makes use of SExtractor and IRAF.

[3] http://obswww.unige.ch/~tewes/alipy/

2.3.4 Photometry

Performing photometry of lensed quasars is a challenging task because lensed quasars are faint and also because the typical angular separation between the images is comparable to typical values of seeing obtained at ground-based telescopes, hence light from the different quasar images are blended with each other and also with light from the lensing galaxy, and thus conventional photometry will not work well on these images. Therefore, specialised procedures are needed to perform accurate photometry of lensed quasars. To perform photometry of the lensed quasar images, we have used the MCS deconvolution algorithm (Magain et al. 1998).

MCS deconvolution

The resolution of a point source as observed through a telescope is inversely proportional to the diameter of the telescope. However, if the observations are carried out using ground based telescopes, the image is degraded by the turbulent atmosphere, thereby limiting the image resolution to the seeing of the site. The image is also blurred by the telescope and the detector having a finite resolving power. However, it is possible to improve the resolution of the images off-line by subsequent numerical processing of the images using the technique of deconvolution.

The observed light distribution of a point source, can be mathematically expressed as a convolution of the original light distribution with the total instrumental profile which includes the atmospheric seeing. This total blurring function is called the point spread function (PSF) of the image. This is written as

$$d(\vec{x}) = t(\vec{x}) * f(\vec{x}) + n(\vec{x}), \tag{2.1}$$

where $d(\vec{x})$ is the observed light distribution, $f(\vec{x})$ is the original light distribution, $t(\vec{x})$ is the total PSF, and $n(\vec{x})$ is the measurement error or noise affecting the data. Also, on observations carried out using CCDs, the observed light distribution is not continuous and is known only at regularly spaced pixels. The imaging equation for a sampled light distribution is

$$d_i = \sum_{j=1}^{N} t_{ij} f_j + n_i, \tag{2.2}$$

where N is the total number of pixels. d_j, f_j, and n_j are the sampled values of $d(\vec{x})$, $f(\vec{x})$, and $n(\vec{x})$ at the pixel j. t_{ij} is the value at pixel j of the PSF centered at pixel i. Given an observed image $d(\vec{x})$ and the PSF $t(\vec{x})$, the aim of deconvolution is to recover the origi-

nal light distribution $f(\vec{x})$. Deconvolution methods such as the maximum entropy method (Skilling & Bryan 1984; Narayan & Nityananda 1986) and the Richardson-Lucy algorithm (Richardson 1972; Lucy 1974) are available, however they suffer from certain weaknesses (Magain et al. 1998). Therefore for this work we have used the MCS deconvolution technique (Magain et al. 1998), named after the authors of the paper. In this procedure, the point spread function (PSF) is modelled for each exposure using bright stars in the vicinity of the target of interest. Since the light distribution observed at a telescope gets spatially sampled by the pixels of the CCD, MCS deconvolution algorithm performs the deconvolution using a PSF which is narrower than the total PSF so that the deconvolved image has a residual PSF which is compatible with the pixel size of the CCD, thus avoiding violation of the sampling theorem. For our work, we perform simultaneous deconvolution of all the exposures, modelling the quasar images as point sources, whose fluxes are allowed to vary from one exposure to the other, and the lensing galaxy as extended light distribution, which is held the same for all the exposures, yielding the light curves of the individual quasar images.

2.3.5 Normalisation

The data frames are typically obtained under differing sky-conditions and varying airmasses. To correct for these effects, a normalisation coefficient needs to be calculated for each individual data frame in order to bring all the data frames to the same photometric level. For this purpose, a set of bright and isolated stars, at least three in number, in the field are chosen. Simultaneous MCS deconvolution of each of the chosen stars is carried out. The fluxes of the stars in each individual data frame are compared to the their respective median fluxes to calculate the ratios. The median value of the ratios in a given data frame is taken to be its normalisation coefficient. The standard deviation of the ratios divided by the square root of the number of stars used gives the calibration error. In the above process, it is important to ensure that the stars used are not significantly variable, by inspecting their light curves.

2.3.6 Estimation of photometric error

The magnitude of an object of interest measured from a given data frame has photometric error, which is estimated by adding the photon shot noise and the calibration error in quadrature. The photon shot noise is calculated according to the denominator term in the

equation for the S/N of a measurement made with a CCD (Howell 2006).

$$\frac{S}{N} = \frac{N_*}{\sqrt{N_* + n_{pix}(N_S + N_D + N_R^2)}} \tag{2.3}$$

Here N_* is the total number of photons collected from the object of interest, n_{pix} is the number of pixels over which the profile of the object is spread out, N_S is the number of counts per pixel from the background, N_D is the number of counts per pixel resulting from dark current (which is negligibly small for the case of the CCD in HFOSC, since it is cryogenically cooled using liquid nitrogen), N_R is the readout noise (4.8 e^- for the CCD in HFOSC).

2.3.7 Combination of magnitudes in an epoch

As noted above, during each night we obtain 3 to 6 dithered exposures. Hence it remains to estimate the magnitude of the object of interest for a given epoch from the magnitudes resulting from the individual exposures. The magnitude for each epoch is taken to be the median value of the magnitudes from the individual data frames in the night and its uncertainty is computed as follows. For each epoch of observation, we compute a theoretical error bar based on the median value of the individual error bars from the data frames obtained in that epoch and also an empirical error bar based on the spread of the magnitudes from the individual data frames. Whichever of the two estimates is larger is adopted to be the photometric uncertainty for that epoch. For details, see Sect. 3.5 of Tewes et al. (2013b).

2.4 Light curves of SDSS J1001+5027

The image reduction and photometry closely follows the procedure described in Tewes et al. (2013b). We performed the flat-field correction and bias subtraction for each exposure using custom software pipelines, which address the particularities of the different telescopes and instruments.

Figure 2.7 shows part of the field around SDSS J1001+5027, obtained by stacking the best monitoring exposures from the Mercator telescope to reach an integrated exposure time of 21 hours. The relative flux measurements of the quasar images and reference stars for each individual epoch were obtained through our COSMOGRAIL photometry pipeline, which is based on the simultaneous MCS deconvolution algorithm. The stars labeled 1, 2,

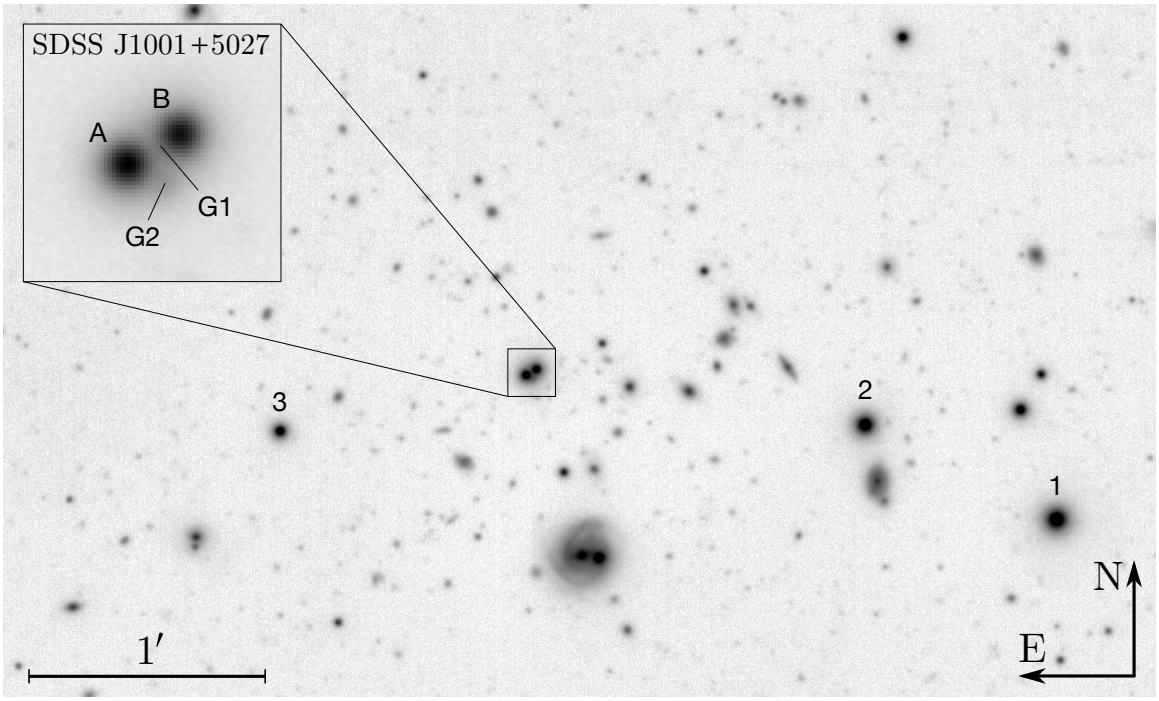

Figure 2.7: R-band image centered on SDSS J1001+5027. The image is the combination of the 210 best exposures from the Mercator telescope, for a total exposure time of 21 hours. We use the stars labeled 1, 2, and 3 to model the PSF and to cross-calibrate the photometry of each exposure. The position of the two lensing galaxies G1 and G2 are indicated in the zoomed image in the upper left. They are most clearly seen in the deconvolved images presented in Fig. 2.8.

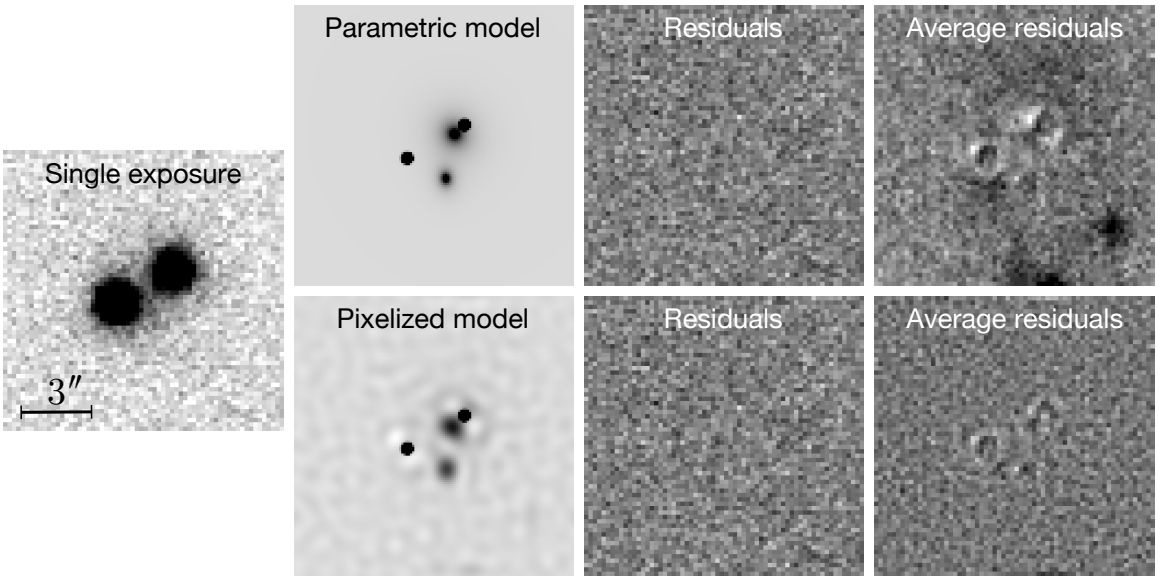

Figure 2.8: Two ways of modeling the light distribution for extended objects during the deconvolution process. On the left is shown a single 360-second exposure of SDSS J1001+5027 obtained with the Mercator telescope in typical atmospheric conditions. The other panels show the parametric (top row) and pixelized light models (bottom row) for the lens galaxies as described in the text. The residual image for the single exposure is also shown in each case, as well as the average residuals over the 120 best exposures. The residual maps are normalized by the shot noise amplitude. The dark areas indicate excess flux in the data with respect to the model. Gray scales are linear.

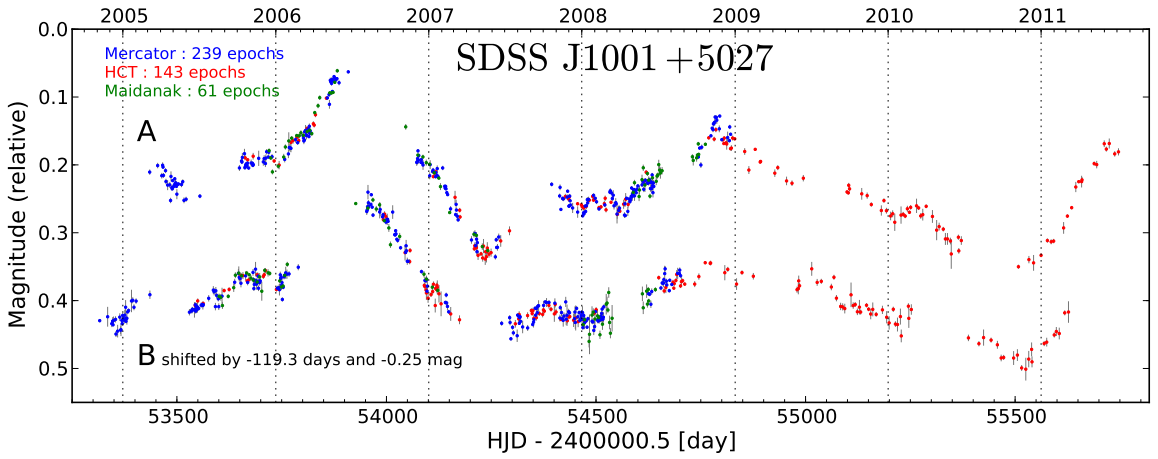

Figure 2.9: R-band light curves of the quasar images A and B in SDSS J1001+5027 from March 2005 to July 2011. The 1σ photometric error bars are also shown. For display purpose, the curve of quasar image B is shown shifted in time by the measured time delay (see text). The light curves are available in tabular form from the CDS and the COSMOGRAIL website.

and 3 in Fig. 2.7 are used to characterize the point spread function (PSF) and relative magnitude zero-point of each exposure.

The two quasar images A and B of SDSS J1001+5027 are separated by 2.86″, which is significantly larger than the typical separation in strongly lensed quasars. In principle, this makes SDSS J1001+5027 a relatively easy target to monitor, as the quasar images are only slightly blended in most of our images. However, image B lies close to the primary lensing galaxy G1. Minimizing the additive contamination by G1 to the flux measurements of B therefore requires a model for the light distribution of G1. In Fig. 2.8, we show two different ways of modeling these galaxies. Our standard approach, shown in the bottom panels, consists in representing all extended objects, such as the lens galaxies, by a regularized pixel grid. The values of these pixels get iteratively updated during the deconvolution photometry procedure. Because of obvious degeneracies, this approach may fail when a relatively small extended object (lens galaxy) is strongly blended with a bright point source (quasar), leading to unphysical light distributions. To explore the sensitivity of our results to a possible bias of this kind, we have adopted an alternative approach of representing G1 and G2 by two simply parametrized elliptical Sersic profiles, as shown in the top row of Fig. 2.8. For both cases, the residuals from single exposures are convincingly homogeneous. Only when averaging the residuals of many exposures to decrease the noise can the simply parametrized models be seen to yield a less good overall fit to the data, since they cannot represent additional background sources nor compensate for small systematic errors in the shape of the PSF.

We find that the difference between these approaches in terms of the resulting quasar flux photometry is marginal; it is insignificant regarding the measurement of the time delay. In all the following we will use the quasar photometry obtained using the parametrized model (top row of Fig. 2.8) which is likely to be closer to reality than our pixelized model in the immediate surroundings of image B.

Following Tewes et al. (2013b), we empirically corrected for small magnitude and flux shifts between the light curve contributions from different telescopes/cameras to obtain minimal dispersion in each of the combined light curves. In the present case we chose the photometry from the Mercator telescope as a reference, and for the data from the Maidanak and HCT telescopes, we optimized a common magnitude shift and individual flux shifts for A and B.

Figure 2.9 shows the combined 6.5-season long light curves, from which we measure a time delay of $\Delta t_{\mathrm{AB}} = -119.3$ days (see Sect. 3.4). In this figure, light curve B has been shifted by this time delay to highlight the correspondence and temporal overlap of the data. We observe strong intrinsic quasar variability, common to images A and B. In the

period 2006 to 2007, the variability in image A is as large as 0.25 magnitudes over a single year. In addition to this large scale correspondence, several small and short scale intrinsic variability features are common to both curves, for instance around December 2005 and January 2010. Our data unambiguously reveal, already to the eye, an approximate time delay of $\Delta t_{\rm AB} \approx -120$ days, with A leading B.

2.4.1 An apparent mismatch between the light curves of the quasar images

The apparent flux ratio between the quasar images, as inferred from the time-shifted light curves shown in Fig. 2.9, stays roughly in the range from 0.40 to 0.44 mag over the length of our monitoring. Strong gravitational lens models readily explain different magnifications of the quasar images, yielding stationary flux ratios or magnitude shifts between the light curves. Figure 2.9 hints, however, at a moderate correlation between some variable flux ratio and the intrinsic quasar variability. In particular, the amplitude of the quasar variability, in units of magnitudes, appears to be smaller in B than in A. Potential reasons for this mismatch include the effects of microlensing by stars of the lens galaxy, or a contamination of the photometry of B by some additive external flux. We find that one has to subtract from curve B about 20% of its median flux to obtain an almost stationary magnitude shift of about 0.66 mag between the light curves. As this contamination would be several times larger than the entire flux of galaxy G1, we conclude that plausible errors of our light models for G1 cannot be responsible for the observed discrepancy between the light curves.

2.5 Light curves of SDSS J0806+2006

The image reduction and photometry follows almost the same procedure as for SDSS J1001+5027 as described in the previous section. Figure 2.10 shows part of the field around SDSS J0806+2006, obtained by stacking the best monitoring exposures from the HCT to reach an integrated exposure time of 5 hours. The stars labeled 1, 2, and 3 in Fig. 2.10 are used to characterize the relative magnitude zero-point of each exposure and the stars 1 and 2 are used to characterize the point spread function (PSF). In Fig. 2.11, we show the results of simultaneous MCS deconvolution of HCT data frames. The lensing galaxy was modelled following the standard approach, wherein all extended objects, including the lensing galaxy, are represented by a regularized pixel grid and the values of these pixels get iteratively updated during the deconvolution photometry procedure. To combine the data

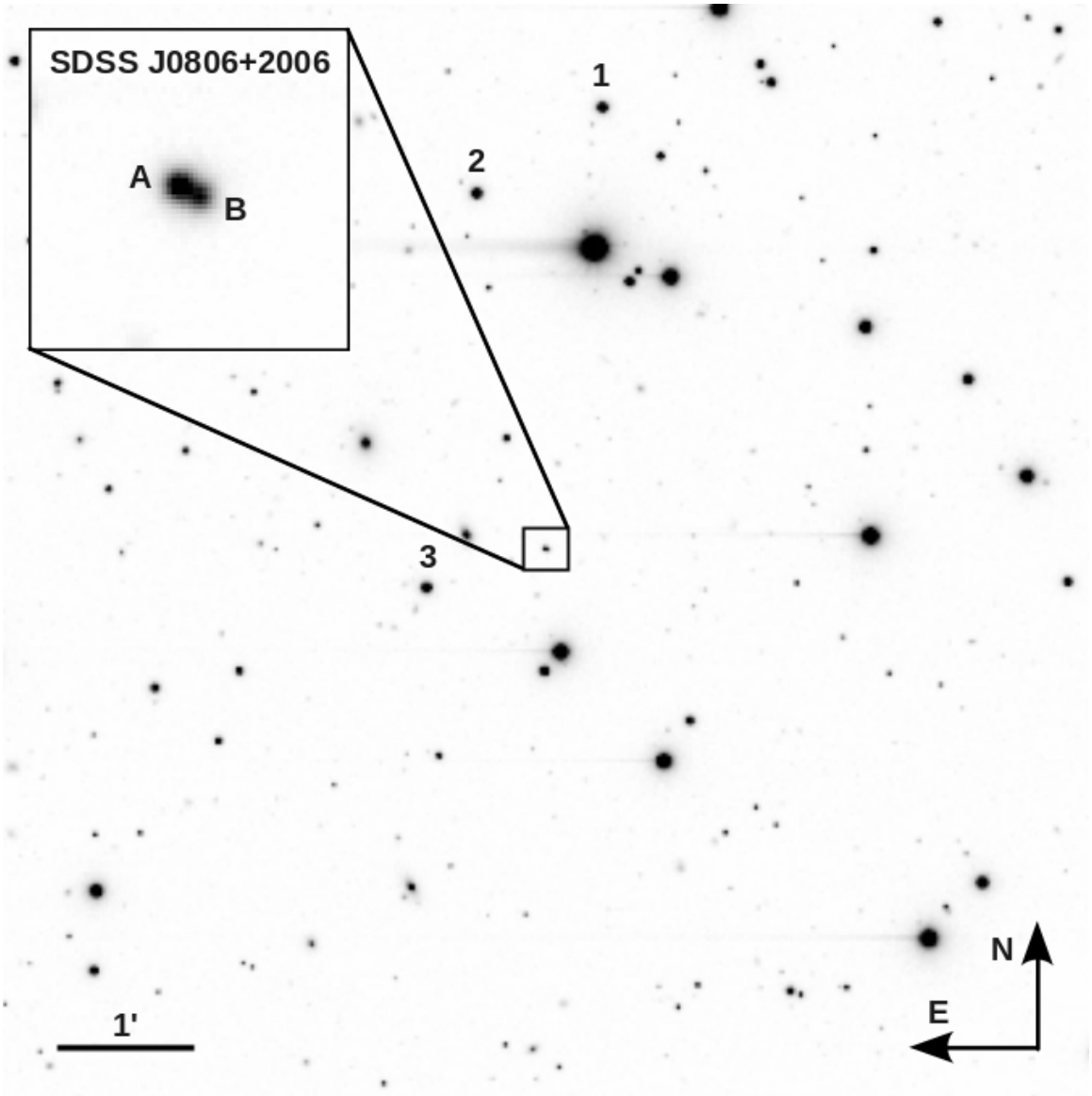

Figure 2.10: R-band image centered on SDSS J0806+2006. The image is the combination of the 58 best exposures from the HCT, for a total exposure time of 5 hours. We use the stars labeled 1, 2, and 3 to cross-calibrate the photometry of each exposure and the stars 1 and 2 to model the PSF.

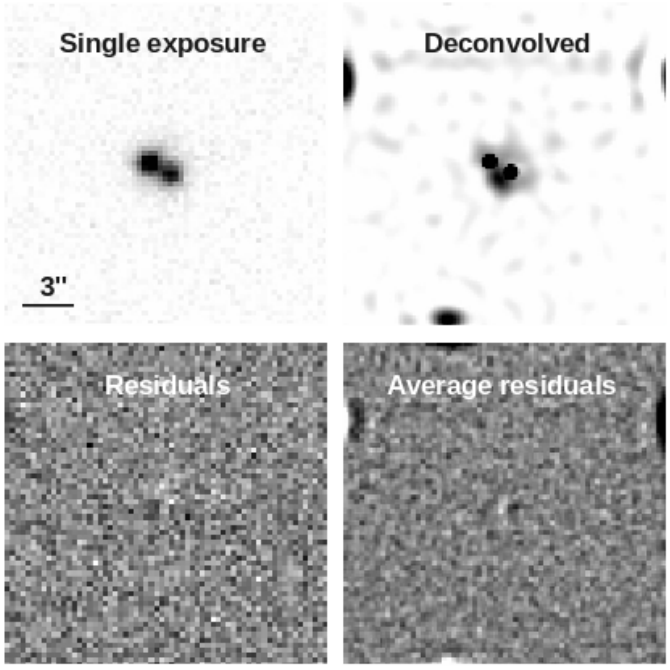

Figure 2.11: On the top left is shown a single 300-second exposure of SDSS J0806+2006 obtained with the HCT in best seeing conditions. The other panels show the deconvolved image consisting of pixelized light model (top right) for the lens galaxy, the residual image for the single exposure (bottom left) and the average residual image (bottom right) for all the exposures. The residual maps are normalized by the shot noise amplitude. The dark areas indicate excess flux in the data with respect to the model. Gray scales are linear.

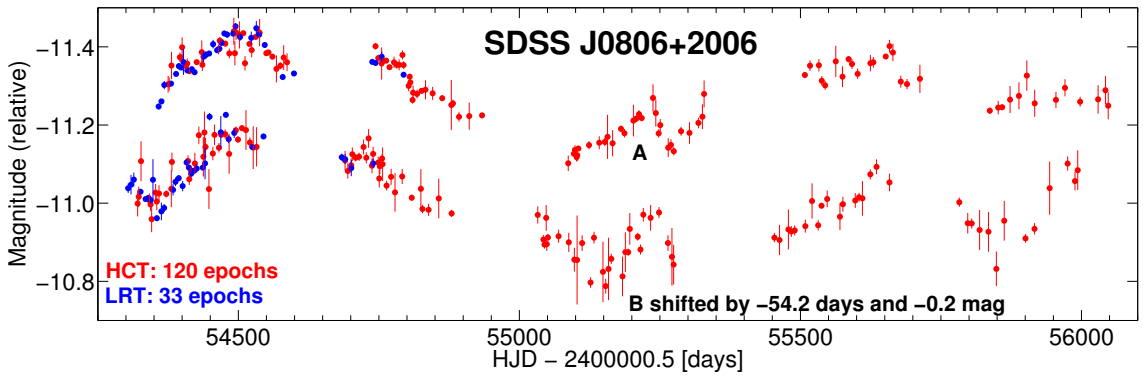

Figure 2.12: R-band light curves of the quasar images A and B in SDSS J0806+2006 from September 2007 to April 2012. The 1σ photometric error bars are also shown. For display purpose, the curve of quasar image B is shown shifted in time by the measured time delay (see text).

points from HCT and LRT, we empirically determined magnitude shifts between the light curve contributions from the two telescopes, to obtain minimal dispersion in each of the combined light curves. In the present case we chose the photometry from HCT as a reference, and for the data from LRT, we optimized magnitude shifts individually for A and B. Figure 2.12 shows the combined 5-season long light curves, from which we measure a time delay of $\Delta t_{\rm AB} = -54.2$ days (see Sect. 3.5), with A leading B. In this figure, light curve B has been shifted by this time delay to highlight the correspondence and temporal overlap of the data. We observe strong intrinsic quasar variability, common to images A and B.

Chapter 3

Determination of time delays of SDSS J1001+5027 and SDSS J0806+2006

3.1 Background

Long before the discovery of the first gravitational lens Q0957+561 by Walsh et al. (1979), Refsdal (1964) had suggested that there will be time delays between flux variations of multiply imaged variable background source such as a quasar. These time delays are due to different times taken for light to travel along the different paths corresponding to the lensed images. These delays can be of the order of days and therefore to measure such time delays one needs to frequently observe the source over long periods of time. This is not so easy to achieve in practice, due to the difficulties in getting telescope time allocated over a long period of time and acquiring good data. Even when telescope time gets allocated, observations will always have hindrance from cloudy sky conditions. Therefore, the data acquired in monitoring observations of this kind are not regularly sampled, and often will have large gaps in the time series. Generally, data could also be obtained from a wide variety of instruments having different sensitivities, and thereby having different levels of errors in the data. Since the use of time delays in constraining H_0 requires these delays to be measured to high precision, it is important that good time delay estimators are used to obtain robust time delay values. A good time delay estimator should effectively take into account the gaps in the time series, heterogeneity of the data, with varied errors and the presence of uncorrelated signal due to microlensing by stars in the intervening lensing galaxy. If not effectively distinguished from the intrinsic variations of the quasar images, these microlensing events in the lensed images remain an unwanted noise for time delay measurements. During the course of the thesis work, I have come up with a novel approach

of determining time delays in the time series data from lensed quasars with measurements at irregular intervals over several years from different telescopes with varied sensitivities as well as being affected from uncorrelated microlensing variations.

3.2 Methods of estimating time delays

There are various techniques available in the literature to estimate time delays from observed quasar light curves. However, two methods are widely used in the literature.

3.2.1 Cross-correlation method

One can deduce a value of the time delay by observing fluctuations in one light curve that are repeated at a later time in the other light curve. Such a comparison suggests a correlation analysis between the observed light curves. In the literature, there are three versions of the cross-correlation method available, namely the Discrete Correlation Function (DCF; Edelson & Krolik 1988), the Locally Normalised Discrete Correlation Function (LNDCF; Lehar et al. 1992) and the z-transformed Discrete Correlation Function (zDCF; Alexander 1997). These are the fastest and simplest time delay estimation methods and they can handle time series that are not uniformly sampled.

Discrete Correlation Function

The discrete correlation function (DCF) was introduced by Edelson & Krolik (1988). For two discrete data sets $X_A(t_i)$ and $X_B(t_j)$, the set of unbinned discrete correlation function (UDCF) is given as

$$UDCF_{ij} = \frac{(X_A(t_i) - \bar{a})(X_B(t_j) - \bar{b})}{\sigma_a \sigma_b} \tag{3.1}$$

for all measured pairs $(X_A(t_i), X_B(t_j))$. Here, $\bar{a}$ and $\bar{b}$ are the mean values of the observed data fluxes $X_A(t_i)$ and $X_B(t_j)$ respectively and σ_a and σ_b are their variances. Each of these values of UDCFs is associated with the pairwise lag $\Delta t_{ij} = t_j - t_i$. Binning these lags in τ gives the DCF(τ). By averaging over all M number of pairs for which $\tau - \delta\tau/2 \leq \Delta t_{ij} \leq \tau + \delta\tau/2$ gives

$$DCF(\tau) = \frac{1}{M} \sum_{i,j} UDCF_{ij}. \tag{3.2}$$

The time delay Δt is that value of τ which maximises $DCF(\tau)$.

Locally Normalized Discrete Correlation Function

This is a variant of the DCF and introduced by Lehar et al. (1992). In the DCF relation given in Eq. 3.1 the $\bar{a}$ and σ_a are replaced by $\bar{a}(\tau)$ and $\sigma_a(\tau)$, which are the mean and standard deviation of the data points in each lag (τ) bin. As discussed above for DCF, the set of unbinned ULNDCF is given as

$$ULNDCF_{ij} = \frac{(X_A(t_i) - \bar{a}(\tau))(X_B(t_j) - \bar{b}(\tau))}{\sigma_a(\tau)\sigma_b(\tau)} \tag{3.3}$$

for all measured pairs $(X_A(t_i), X_B(t_j))$. By averaging over all M number of pairs for which $\tau - \delta\tau/2 \leq \Delta t_{ij} \leq \tau + \delta\tau/2$ gives

$$LNDCF(\tau) = \frac{1}{M}\sum_{i,j} ULNDCF_{ij}. \tag{3.4}$$

The time delay Δt is that value of τ which maximises $LNDCF(\tau)$.

z-transformed Discrete Correlation Function

The z-transformed discrete correlation function (zDCF) is a variant of the DCF method for estimating the cross correlation function of sparse, unevenly sampled light curves. The zDCF method (Alexander 1997) corrects various biases of the DCF method of Edelson & Krolik (1988), by using equal population binning and Fisher's z-transform.

Dispersion method

The Dispersion method is a non-parametric form of calculating time delays in lensed quasar light curves and was introduced by Pelt et al. (1996). Given two time series $X_A(t_i)$ and $X_B(t_j)$, dispersion is nothing but a weighted sum of the squared differences between $X_A(t_i)$ and $X_B(t_j)$ (for a given time lag (τ) and flux ratio (l)). This method is similar to that of the DCF, however, it models the time series of the two light curves in a different way, in which a combined light curve C_k is generated by combining both the time series, where k = 1, 2, ... , N, where N is the total number of data points in the combined light curve. The simplest form of the dispersion function is given as

$$D_l^2 = min_l \frac{\sum_{k=1}^{N-1} W_k (C_{k+1} - C_k)^2}{2\sum_{k=1}^{N-1} W_k}, \tag{3.5}$$

where the W_k are the statistical weights of the combined light curve,

$$W_k = W_{i,j} = \frac{W_i W_j}{W_i + W_j}. \tag{3.6}$$

The time delay in this method is found by minimizing D^2 over a range of trial time delays. In general, we found the dispersion method to perform better compared to the DCF method. Whereas the DCF method cannot allow for the presence of uncorrelated variations between the light curves, the dispersion method allows for uncorrelated variations to be modelled as lower-order polynomials, which is adequate if the uncorrelated variations are slow occuring over several years. It is of interest to develop techniques which can cope with uncorrelated variations happening over much smaller timescales. During the course of this thesis work, I have developed a new time delay estimation method called the "difference-smoothing technique", which can model small duration microlensing variations. This technique is based on minimizing the residuals of a high-pass filtered difference light curve between the quasar images.

3.3 Difference-smoothing technique

This technique is a point estimator that determines both an optimal time delay and an optimal shift in *flux* between two light curves, while also allowing for smooth extrinsic variability. These extrinsic variations could arise due to microlensing by stars in the lensing galaxy which affect the brightnesses of different quasar images differently due to their different paths (Chang & Refsdal 1979). The correction for a flux shift between the light curves explicitly addresses the mismatch described in Sect. 2.4.1, whatever its physical explanation. This flux shift may be due to a contamination of light curve B by residual light from the lensing galaxy, from the lensed quasar host galaxy, or by microlensing resolving the quasar structure.

We consider two light curves A and B sampled at epochs t_i, where A_i and B_i are the observed magnitudes at epochs t_i, $(i = 1, 2, 3, ..., N)$. We select A as the reference curve. Light curve B is shifted in time with respect to A by some amount τ, and in *flux* by some amount Δf. Formally, this shifted version B' of B is given by

$$\mathrm{B}'_i = -2.5 \log\left(10^{-0.4\,\mathrm{B}_i} + \Delta f\right), \tag{3.7}$$

$$t'_i = t_i + \tau. \tag{3.8}$$

For any estimate of the time delay τ and of the flux shift Δf, we form a *difference light*

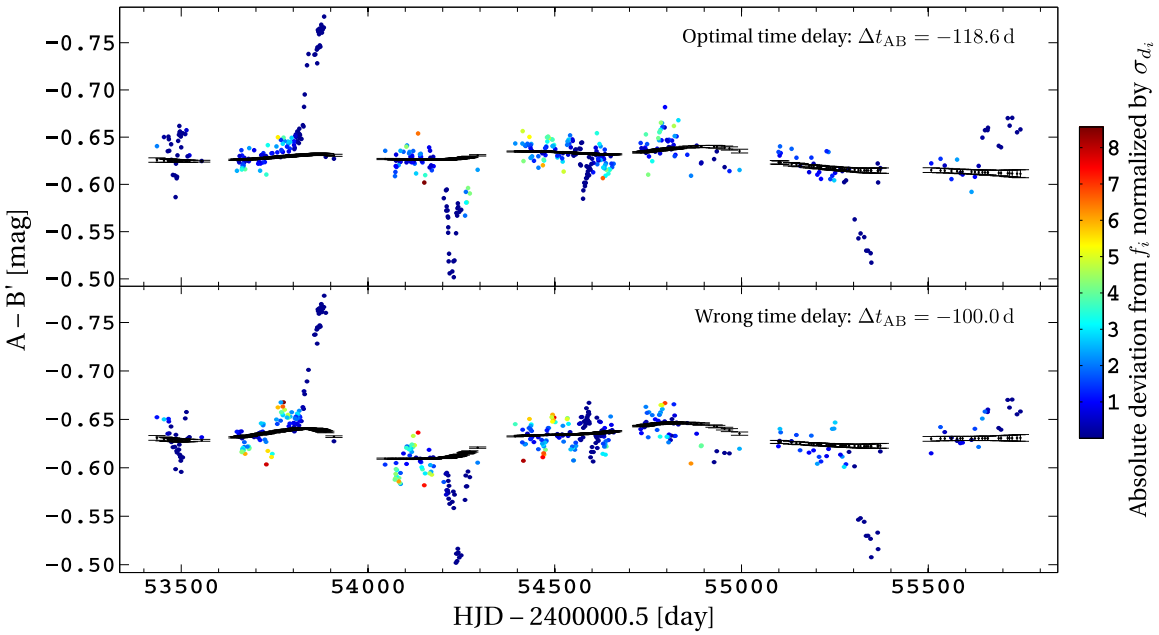

Figure 3.1: Difference light curves of SDSS J1001+5027 as obtained by the new difference-smoothing technique introduced in Rathna Kumar et al. (2013). The curves are shown for the best time-delay estimate found with this technique (top panel, $\Delta t_{AB} = -118.6$ days), and for a wrong time-delay value (bottom panel, $\Delta t_{AB} = -100.0$ days). The difference light curves d_i are shown as colored points. They are smoothed using a kernel of width $s = 100$ days to compute the f_i (black points). The error bars on the black points show the uncertainty coefficients σ_{f_i}. The points in the difference light curve d_i are color-coded according to the absolute factors of their uncertainties σ_{d_i} by which they deviate from f_i. In both panels, light curve A is used as reference, and light curve B is shifted in flux by the same amount.

curve, with points d_i at epochs t_i,

$$d_i(\tau, \Delta t) = \mathrm{A}_i - \frac{\sum_{j=1}^{N} w_{ij} \mathrm{B}'_j}{\sum_{j=1}^{N} w_{ij}}, \tag{3.9}$$

where the weights w_{ij} are given by

$$w_{ij} = \frac{1}{\sigma^2_{\mathrm{B}_j}} e^{-(t'_j - t_i)^2 / 2\delta^2}. \tag{3.10}$$

The parameter δ is the decorrelation length, as in Pelt et al. (1996), and σ_{B_j} denotes the photometric error of the magnitude B_j. This decorrelation length should typically be of the order of the sampling period, small enough to not smooth out any intrinsic quasar variability

features from the light curve B. The uncertainties on each d_i are then calculated as

$$\sigma_{d_i} = \sqrt{\sigma_{\mathrm{A}_i}^2 + \frac{1}{\sum_{j=1}^{N} w_{ij}}}, \tag{3.11}$$

where w_{ij} are given by Eq. 3.10. To summarize, at this point we have a discrete difference light curve, sampled at the epochs of curve A, built by subtracting from light curve A a smoothed and shifted version of B. We now smooth this difference curve d_i, again using a Gaussian kernel, to obtain a model f_i for the differential extrinsic variability

$$f_i = \frac{\sum_{j=1}^{N} \nu_{ij} d_j}{\sum_{j=1}^{N} \nu_{ij}}, \tag{3.12}$$

where the weights ν_{ij} are given by

$$\nu_{ij} = \frac{1}{\sigma_{d_j}^2} e^{-(t_j - t_i)^2/2s^2}. \tag{3.13}$$

The smoothing time scale s is a second free parameter of this method. Its value must be chosen to be significantly larger than δ. For each f_i, we compute an uncertainty coefficient

$$\sigma_{f_i} = \sqrt{\frac{1}{\sum_{j=1}^{N} \nu_{ij}}}. \tag{3.14}$$

The idea of the present method is now to optimize the time-delay estimate τ and flux shift Δf to minimize residuals between the difference curve d_i and the much smoother f_i. Any incorrect value for τ introduces relatively fast structures that originate from the quasar variability into d_i, and these structures will not be well represented by f_i. Figure 3.1 illustrates this phenomenon in the case of SDSS J1001+5027 by showing d_i and f_i for an optimal and an arbitrarily chosen wrong time-delay estimate. In both panels of Fig. 3.1, the largest deviations between d_i and f_i are due to poorly constrained points with very high σ_{d_i}, and are therefore not significant. However, for the incorrect time-delay estimate, a larger number of well-constrained points of d_i significantly deviate from f_i (yellow and red points). To quantify this match between d_i and f_i we define a cost function in the form of a normalized χ^2,

$$\overline{\chi}^2 = \left[\sum_{i=1}^{N} \frac{(d_i - f_i)^2}{\sigma_{d_i}^2 + \sigma_{f_i}^2}\right] \Big/ \left[\sum_{i=1}^{N} \frac{1}{\sigma_{d_i}^2 + \sigma_{f_i}^2}\right], \tag{3.15}$$

and minimize this $\overline{\chi}^2(\tau, \Delta f)$ using a global optimization.

In the above description, light curves A and B are not interchangeable, thus introducing an asymmetry into the time-delay measurement process. To avoid this arbitrary choice of the reference curve, we systematically perform all computations for both permutations of A and B, and minimize the sum of the two resulting values of $\overline{\chi}^2$.

3.3.1 The uncertainty estimation procedure

As a point estimator, the technique described above does not provide information on the uncertainty of its result. We stress that simple statistical techniques such as variants of bootstrapping or resampling cannot be used to quantify the uncertainty of such highly non-linear time-delay estimators (Tewes et al. 2013a). These approaches are not able to discredit "lethargic" estimators, which favor a particular solution (or a small set of solutions) while being relatively insensitive to the actual shape of the light curves. Furthermore, they are not sensitive to plain systematic biases of the techniques.

Consequently, to quantify the random and systematic errors of this estimator, for each dataset to be analyzed and as a function of its free parameters, we follow the Monte Carlo analysis described in Tewes et al. (2013a). It consists in applying the point estimator to a large number of fully synthetic light curves, which closely mimic the properties of the observed data, but have known true time delays. It is particularly important that these synthetic curves cover a range of true time delays around a plausible solution, instead of all having the same true time delay. Only this feature enables the method to adequately penalize estimators with lethargic tendencies.

3.3.2 Application to SDSS J1001+5027

The decorrelation length δ and the width of the smoothing kernel s are the two free parameters of the described technique. In Rathna Kumar et al. (2013), we choose δ to be equal to the mean sampling of the light curves ($\delta = 5.2$ days) and $s = 100$ days, yielding a point estimate of $\Delta t_{\mathrm{AB}} = -118.6$ days for the time delay. The corresponding d_i and f_i difference light curves are shown in the top panel of Fig. 3.1. Results of the uncertainty analysis will be presented in the next section, together with the performance of other point estimators.

We have explored a range of alternative values for the free parameters ($s = 50, 100, 150, 200$ and $\delta = 2.6, 5.2, 10.4$ days), and find that neither the time-delay point estimate from the observed data, nor the error analysis is significantly affected. The time-delay estimates resulting from these experiments stay within 1.2 days around the reference value obtained for $\delta = 5.2$ and $s = 100$ days. Regarding the uncertainty analysis, we observe that increasing the smoothing length scale s beyond 100 days decreases the random

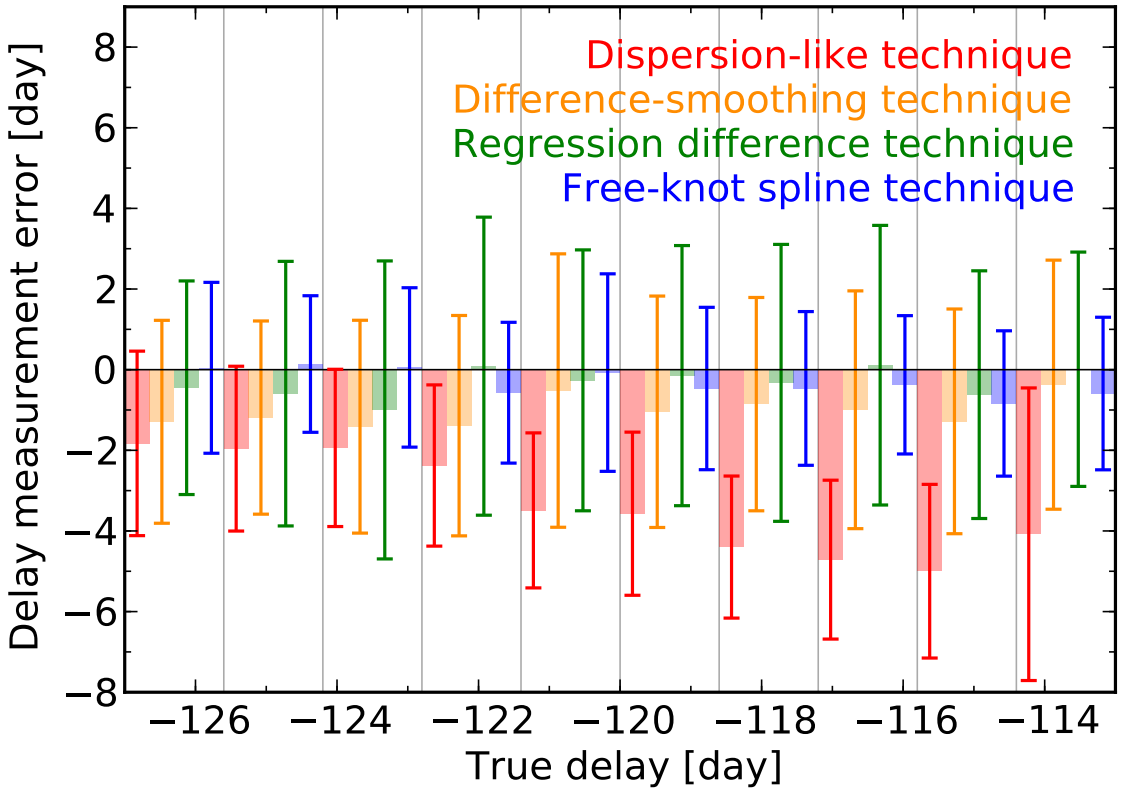

Figure 3.2: Error analysis of the four time-delay measurement techniques, based on delay estimations on 1000 synthetic curves that mimic our SDSS J1001+5027 data. The horizontal axis corresponds to the value of the true time delay used in these synthetic light curves. The gray vertical lines delimit bins of true time delay. In each of these bins, the colored rods and 1σ error bars show the systematic biases and random errors, respectively, as committed by the different techniques.

error, but at the cost of an increasing bias, which is not surprising.

3.4 Time-delay measurement of SDSS J1001+5027

The details of the observations are summarised in Table 2.2 and the light curves are displayed in Fig. 2.9. Although an unambiguous approximation of the time delay of SDSS J1001+5027 can be made by eye, accurately measuring its value is not trivial, and is made more difficult by the extrinsic variability between the light curves. Even more obvious features of the data, such as the sampling gaps due to non-visibility periods of the targets, could easily bias the results from a time-delay measurement technique. The impact of these effects on the quality of the time-delay inference clearly differs for each individual quasar

Table 3.1: Time-delay measurements for SDSS J1001+5027. The total 1σ error bars are given. Whenever possible, we give in parenthesis the breakdown of the error budget: (random, systematic).

Method	Δt_{AB} [day]
Dispersion-like technique	-120.5 +/- 6.2 (3.6, 5.0)
Difference-smoothing technique	-118.6 +/- 3.7 (3.4, 1.4)
Regression difference technique	-121.1 +/- 3.8 (3.7, 1.0)
Free-knot spline technique	-119.7 +/- 2.6 (2.4, 0.8)
GP by Hojjati et al. (2013)	-117.8 +/- 3.2
Combined estimate (see text)	-119.3 +/- 3.3

lensing system and dataset. To check for potential systematic errors, a wise approach is to employ several numerical methods based on different fundamental principles.

In Rathna Kumar et al. (2013), we use five different methods to measure the time delay of SDSS J1001+5027 from the data shown in Fig. 2.9. All these methods have been developed to address light curves affected by extrinsic variability, resulting from microlensing by stars in the lensing galaxy (Chang & Refsdal 1979) or flux contamination. Three of the techniques, namely the dispersion-like technique, the regression difference technique, and the free-knot spline technique are described in length in Tewes et al. (2013a) and were used to measure the time delays in the four-image quasar RX J1131−1231 (Tewes et al. 2013b).

In the the previous section, we presented our fourth method, the difference-smoothing technique. These first four methods are point estimators: they provide best estimates, without information on the uncertainty of their results. We proceed by quantifying the accuracy and precision of these estimators by applying them to a set of 1000 fully synthetic light curves, produced and adjusted following Tewes et al. (2013a). These simulations include the intrinsic variations of the quasar source, mimicking the observed variability of SDSS J1001+5027, as well as extrinsic variability on a range of time scales from a few days to several years. They share the same sampling and scatter properties as the real observations.

Figure 3.2 shows the results of this analysis, depicting the delay measurement error as a function of the true delay used to generate the synthetic light curves. As always, this analysis naturally takes into account the intrinsic variances of the techniques, that are due to the limited ability of the employed global optimizers to find the absolute minima of the cost functions.

As can be seen in Fig. 3.2, the dispersion-like technique is strongly biased for this particular dataset. This could be a consequence of the simplistic polynomial correction for extrinsic variability linked to this technique. For the other techniques, the bias remains smaller than the random error, and no strong dependence on the true time delay is detected.

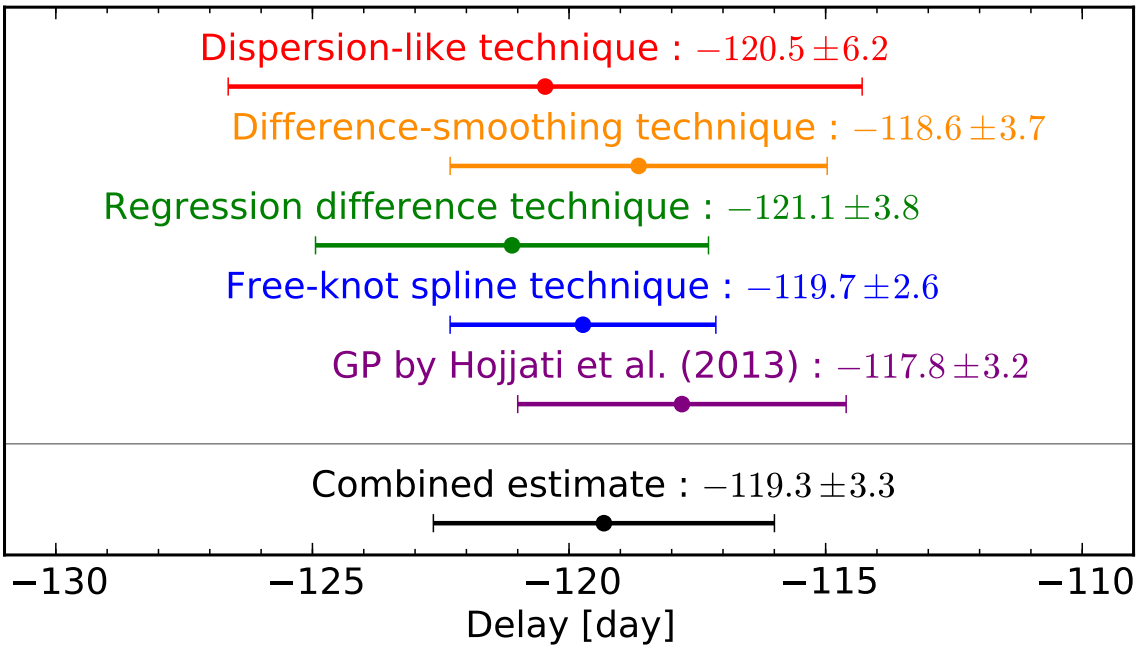

Figure 3.3: Time-delay measurements of SDSS J1001+5027, following five different methods. The total error bar shown here includes systematic and random errors.

The final systematic error bar for each of these four techniques is taken as the worst measured systematic error on the simulated light curves (biggest colored rod in Fig. 3.2). The final random error is taken as the largest random error across the range of tested time delays. Finally, the total error bar for each technique is obtained by summing the systematic and random components in quadrature.

In the writing process of Rathna Kumar et al. (2013), Hojjati et al. (2013) proposed a new independent method to measure time delays that is also able to address extrinsic variability. Their method is based on Gaussian process modeling, and does not rely on point estimation. It provides its own standalone estimate of the total uncertainty. We have provided these authors with the COSMOGRAIL data of SDSS J1001+5027, without letting them know our measured values. They find $\Delta t_{\rm AB} = -117.8 \pm 3.2$ days.

We include this measurement by Hojjati et al. (2013) as a fifth measurement in our result summary, presented in Table 3.1 and in a more graphical form in Fig. 3.3. Not only do their time-delay values agree with our four estimates, but also their error bars agree well with ours, in spite of the totally different way of estimating them.

We have five time-delay estimates from five very different methods, and all these estimates are compatible with each other. We now need to combine these results. In doing this, we exclude the delay from the dispersion-like technique that, as we show, is dominated by

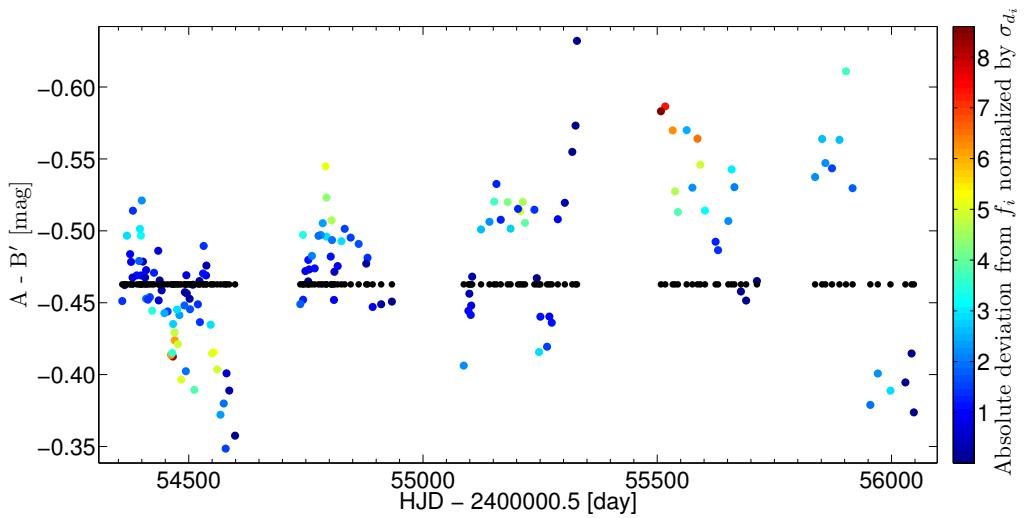

Figure 3.4: Difference light curve of SDSS J0806+2006 as obtained by the difference-smoothing technique. The curve is shown for the best time-delay estimate found with this technique ($\Delta t_{\mathrm{AB}} = -54.2$ days). The difference light curves d_i are shown as colored points. They are smoothed using a kernel of width $s = \infty$ to compute the f_i (black points). The error bars on the black points show the uncertainty coefficients σ_{f_i}. The points in the difference light curve d_i are color-coded according to the absolute factors of their uncertainties σ_{d_i} by which they deviate from f_i. Light curve A is used as reference.

systematic errors. While the estimates from the four remaining techniques are obtained with very different methods, they are still not independent, as they all make use of the same data. We therefore simply average the four time-delay measurements to obtain our combined estimate, and we use the average of the total uncertainties as the corresponding uncertainty. This leads to $\Delta t_{\mathrm{AB}} = -119.3 \pm 3.3$ days, shown in black in Fig. 3.3.

Further, as our new difference-smoothing technique gives results that are similar to other independent methods, we use this technique only to get the time delay for the second lensed quasar observed in this study, namely SDSS J0806+2006.

3.5 Time-delay measurement of SDSS J0806+2006

The details of the observations are summarised in Table 2.3 and the light curves are displayed in Fig. 2.12. In Sect. 4.1, we present a modification to the difference-smoothing technique and introduce a recipe for creating simulated light curves having known time delays in a plausible range around the measured delay. Further in Sect. 4.1, we present a method to tune the free parameters of the difference-smoothing technique for a given pair of light curves. Following this approach, we set $\delta = 11.1$ days and $s = \infty$ (since we do

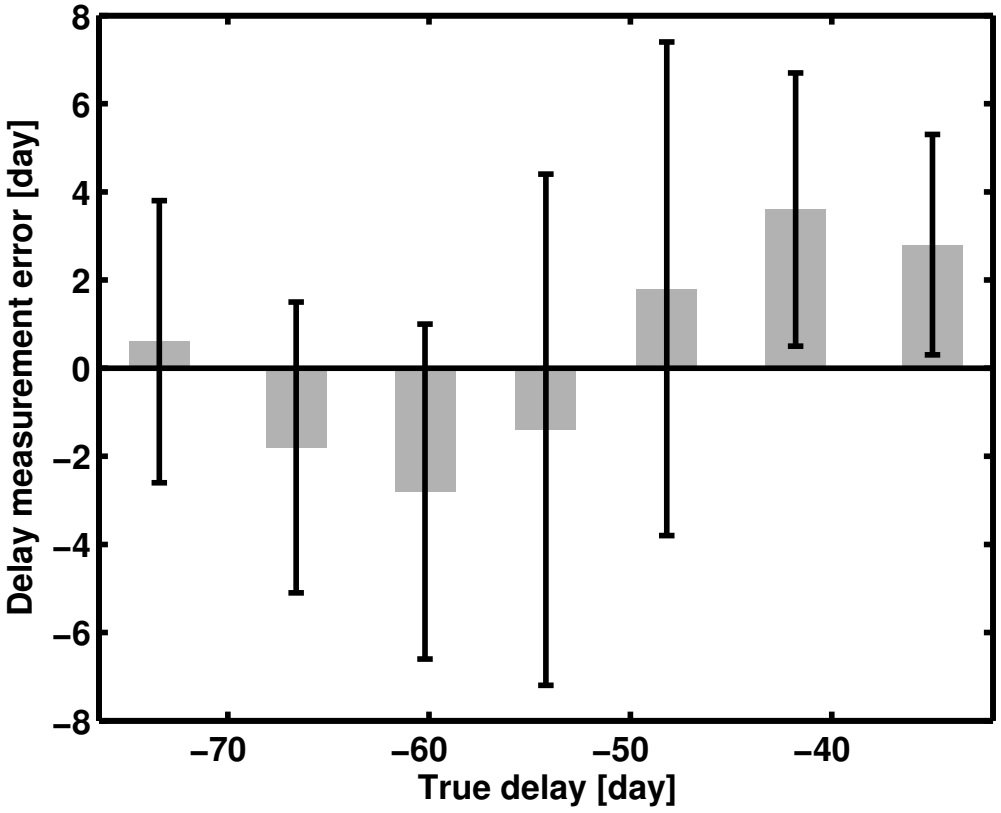

Figure 3.5: Error analysis of the time-delay measurement using difference-smoothing technique, based on delay estimations on simulated light curves that mimic our SDSS J0806+2006 data. The horizontal axis corresponds to the value of the true time delay used in these simulated light curves. The gray colored rods and 1σ error bars show the systematic biases and random errors, respectively, as committed by the difference-smoothing technique.

not detect any statistically significant uncorrelated variation between the two light curves), and measured a time delay of $\Delta t_{\rm AB} = -54.2 \pm 6.8$ days (1σ uncertainty, 12.5% precision), with image A leading image B. The difference light curve for the measured delay is plotted in Fig. 3.4. The uncertainty of the measured time delay was estimated following the procedure outlined in Sect. 4.1.4. Figure 3.5 shows the results of this analysis, depicting the delay measurement error as a function of the true delay used to generate the simulated light curves.

Further, the large error in the time delay measured for SDSS J0806+2006 is due to the quality of the light curves, with large gaps, low S/N and lack of large amplitude variability of the quasar. Accumulation of more high S/N ratio data frames with better temporal sampling on this source will surely bring down the error in the time delay measured for this source.

Chapter 4

Homogeneous estimation of time delays of 24 gravitationally lensed quasars

Till date, time delays have been reported for 24 gravitationally lensed quasars among the hundreds of such strongly lensed quasars known. However the quality of the light curves and the techniques used to infer these time delays vary from one system to the other. In this chapter, we apply the difference-smoothing technique, presented in Chapter 3, to the publicly available light curves of the 24 systems in a homogeneous manner, firstly to identify systems having robust time delay measurements and then select a sub-sample of suitable lens systems to determine H_0 in Chapter 5.

The chapter is organized as follows. Section 4.1 describes the technique used for time delay determination and introduces a recipe for creating realistic simulated light curves having known time delays, which is used in this chapter to estimate the uncertainty of each measured delay. In Sect. 4.2, the application of the curve-shifting procedure to the 24 systems is described.

4.1 Time delay determination

In this section, we discuss one modification to the original version of the difference-smoothing technique reported in Rathna Kumar et al. (2013) (see Sect. 3.3 for the rest of the details). We then introduce a recipe for simulating realistic light curves having known time delays in a plausible range around the measured delay in order to estimate its uncertainty. We also present an approach to tune the free parameters of the difference-smoothing technique for a given dataset.

4.1.1 Modification to the difference-smoothing technique

A_i and B_i are the observed magnitudes constituting light curves A and B sampled at epochs t_i ($i = 1,2,3,...,N$). Light curve A is selected as the reference. We shift the light curve B in time with respect to the light curve A by some amount τ. This shifted version B' of B is given by

$$B'_i = B_i, \tag{4.1}$$

$$t'_i = t_i + \tau. \tag{4.2}$$

We note here that we do not apply any flux shift to light curve B as in Rathna Kumar et al. (2013), since we have found that doing so considerably increases the computational time without significantly changing the results.

4.1.2 Simulation of light curves

In Rathna Kumar et al. (2013), in order to estimate the uncertainty of the time delay measured using the difference-smoothing technique, we made use of realistic simulated light curves, which were created following the procedure introduced in Tewes et al. (2013a). In this work, we introduce an independent recipe for creating simulated light curves. Here we follow the same notation as in Sect. 3.3.

We infer the underlying variation $A(t)$ of the light curve A at the epoch t_i based on the magnitudes A_j for the remaining epochs as

$$A(t_i) = \frac{\sum_{j=1}^{N}{}^{j\neq i} \frac{1}{\sigma_{A_j}^2} e^{-(t_j - t_i)^2/2m^2} A_j}{\sum_{j=1}^{N}{}^{j\neq i} \frac{1}{\sigma_{A_j}^2} e^{-(t_j - t_i)^2/2m^2}}, \tag{4.3}$$

where the value of m is set to equal the mean sampling of the light curves. For those points having the nearest neighbour separated by less than m, we compute the values of $(A_i - A(t_i))/\sigma_{A_i}$, the standard deviation of which is multiplied to the error bars σ_{A_i} to obtain the rescaled error bars $\hat{\sigma}_{A_i}$. Similarly for the B light curves the rescaled error bars $\hat{\sigma}_{B_i}$ are obtained. This rescaling is done since the magnitudes of the original error bars may suffer from systematic under-estimation or over-estimation.

We merge the light curves A and B by shifting the B light curve by the time delay found (Δt) and subtracting the differential extrinsic variability f_i corresponding to the delay from the A light curve. This merged light curve M_i, whose errors we denote σ_{M_i}, consists of the magnitudes $A_i - f_i$ at times t_i and having errors $\hat{\sigma}_{A_i}$ and the magnitudes B_i at times $t_i + \Delta t$

and having errors $\hat{\sigma}_{\mathrm{B}_i}$. We now model the quasar brightness variation $\mathrm{M}(t)$ as

$$\mathrm{M}(t) = \frac{\sum_{j=1}^{2N} \frac{1}{\sigma^2_{\mathrm{M}_j}} e^{-(t_j-t)^2/2m^2} \mathrm{M}_j}{\sum_{j=1}^{2N} \frac{1}{\sigma^2_{\mathrm{M}_j}} e^{-(t_j-t)^2/2m^2}}. \tag{4.4}$$

We then model the quasar brightness variation using only the A points in M_i as

$$\mathrm{M}_{\mathrm{A}}(t) = \frac{\sum_{j=1}^{N} \frac{1}{\hat{\sigma}^2_{\mathrm{A}_j}} e^{-(t_j-t)^2/2m^2} (\mathrm{A}_j - f_j)}{\sum_{j=1}^{N} \frac{1}{\hat{\sigma}^2_{\mathrm{A}_j}} e^{-(t_j-t)^2/2m^2}} \tag{4.5}$$

and only the B points in M_i as

$$\mathrm{M}_{\mathrm{B}}(t) = \frac{\sum_{j=1}^{N} \frac{1}{\hat{\sigma}^2_{\mathrm{B}_j}} e^{-(t_j+\Delta t-t)^2/2m^2} \mathrm{B}_j}{\sum_{j=1}^{N} \frac{1}{\hat{\sigma}^2_{\mathrm{B}_j}} e^{-(t_j+\Delta t-t)^2/2m^2}}. \tag{4.6}$$

The residual extrinsic variations present in the A and B light curves can now be calculated as

$$f_{\mathrm{A}_i} = \mathrm{M}_{\mathrm{A}}(t_i) - \mathrm{M}(t_i) \tag{4.7}$$

and

$$f_{\mathrm{B}_i} = \mathrm{M}_{\mathrm{B}}(t_i) - \mathrm{M}(t_i). \tag{4.8}$$

We can now simulate light curves A_i^{simu} and B_i^{simu} having a time delay of $\Delta t + dt$ between them by sampling $\mathrm{M}(t)$ at appropriate epochs and adding terms for extrinsic variations and noise,

$$\mathrm{A}_i^{simu} = \mathrm{M}\left(t_i - \frac{dt}{2}\right) + f_i + f_{\mathrm{A}_i} + N^*(0,1)\hat{\sigma}_{\mathrm{A}_i} \tag{4.9}$$

and

$$\mathrm{B}_i^{simu} = \mathrm{M}\left(t_i + \Delta t + \frac{dt}{2}\right) + f_{\mathrm{B}_i} + N^*(0,1)\hat{\sigma}_{\mathrm{B}_i}, \tag{4.10}$$

where $N^*(0,1)$ is a random variate drawn from a normal distribution having mean 0 and variance 1. These simulated light curves are then assigned the times t_i and the error bars σ_{A_i} and σ_{B_i} for the A and B light curves respectively. Including the terms f_{A_i} and f_{B_i} in the calculation of A_i^{simu} and B_i^{simu} respectively ensures that our simulated light curves contain extrinsic variability on all timescales, just as in the real light curves.

Here again in the above description, since light curves A and B are not interchangeable, we systematically perform all computations for both permutations of A and B, and average

the corresponding values of A_i^{simu} and B_i^{simu}, before adding the noise terms.

4.1.3 Choice of free parameters

The value of the decorrelation length δ needs to be chosen to be of the order of the temporal sampling of the light curves. In our present work, as in Rathna Kumar et al. (2013), we set δ equal to m, the mean sampling of the light curves.

The smoothing time scale s needs to be chosen to be significantly larger than δ. In our present work, its value is set to the largest integer multiple of δ for which the maximum absolute values of both $\frac{f_{A_i}}{\hat{\sigma}_{A_i}}$ and $\frac{f_{B_i}}{\hat{\sigma}_{B_i}}$, which quantify the residual extrinsic variations in units of photometric noise for the A and B light curves respectively, are smaller than 3. This choice ensures that the value of s is small enough to adequately model the extrinsic variations, so that the extreme values of residual extrinsic variations are not significantly larger than the noise in the data.

Again as in the above description, as light curves A and B are not interchangeable, we systematically perform all the computations for both permutations of A and B, and average the corresponding maximum absolute values.

4.1.4 Estimation of uncertainty

We create 100 simulated light curves having a true delay of Δt between them. The difference-smoothing technique is applied on each of them to obtain 100 delay values. The standard deviation of the 100 delay values gives us the random error and the systematic error is obtained by the difference between the mean of the 100 delay values and the true delay. The total error $\Delta\tau_0$ is obtained by adding the random error and the systematic error in quadrature.

However, as noted by Tewes et al. (2013a), it is important to simulate light curves having not only the time delay Δt found, but also other time delays in a plausible range around Δt, so as to obtain a reliable estimate of the uncertainty (see also Sect. 3.2 in Rathna Kumar et al. 2013). To this end, we also simulate 100 light cuves for each true delay which differs from Δt by $\pm\Delta\tau_0, \pm(\Delta\tau_0+\Delta\tau_1), \ldots, \pm(\Delta\tau_0+\Delta\tau_1+\ldots+\Delta\tau_{n-1})$, in each step updating the total error $\Delta\tau_n$ by adding the maximum obtained value of the random error and the maximum obtained absolute value of the systematic error in quadrature. n is chosen to be the smallest integer for which

$$\Delta\tau_0+\Delta\tau_1+\ldots+\Delta\tau_{n-1} \geq 2\Delta\tau_n. \tag{4.11}$$

This ensures that we have simulated light curves over a range of delay values which is at least as wide or wider than the 95.4% confidence interval implied by the stated final error $\Delta\tau_n$.

The application of the procedures outlined in this section to the light curves of SDSS J0806+2006 is discussed in Sect. 3.5

4.2 Time delays of 24 gravitationally lensed quasars

Till date, time delays have been reported for 24 gravitationally lensed quasars. However, the quality of the data and the curve-shifting procedure followed differs from system to system. In this section, we present a homogeneous analysis of their publicly available light cuves following the procedure described in the previous section, with the aim of identifying those systems having reliable time delay measurements. In case of systems with more than two images, we measured the time delays between all pairs of light curves.

The results are summarised in Table 4.1, wherein a negative value of time delay implies that the arrival-time order is reverse of what is implied in the subscript to Δt. All quoted uncertainties are 1σ error bars, unless stated otherwise. Additional information on some systems listed in Table 4.1 are given below.

– *Q0142−100 (UM673):* We were unable to make a reliable time delay measurement using the light curves presented in Koptelova et al. (2012).

– *JVAS B0218+357:* From 8 GHz and 15 GHz VLA observations reported by Cohen et al. (2000), we measured time delays of 10.1 $\pm$ 2.0 days and 11.4 $\pm$ 2.4 days respectively. Taking the weighted average of the two results, we find the time delay to be 10.6 $\pm$ 1.5 days.

– *SBS 0909+532:* We were unable to make a reliable time delay measurement using the light curves presented in Goicoechea et al. (2008) and Hainline et al. (2013).

– *RX J0911.4+0551:* We used the light curves presented in Hjorth et al. (2002), which were made publicly available by Paraficz et al. (2006).

– *FBQ 0951+2635:* We used the light curves presented in Jakobsson et al. (2005), which were made publicly available by Paraficz et al. (2006).

– *Q0957+561:* From the r-band and g-band light curves presented in Shalyapin et al. (2012), we measured time delays of 418.8 $\pm$ 2.5 days and 418.6 $\pm$ 1.9 days respectively. Taking the weighted average of the two results, we find the time delay to be 418.7 $\pm$ 1.5 days. The reported delay listed is the weighted average of the two delays found by Shalyapin et al. (2012).

– *RX J1131−1231:* Tewes et al. (2013b) measured time delays between all pairs of light curves using three different numerical techniques. The time delay value listed in the table for each pair of light curves is for that technique which resulted in the smallest uncertainty.

– *CLASS B1600+434:* From the optical light curves presented in Burud et al. (2000) (and made publicly available by Paraficz et al. (2006)), we measure a time delay in agreement with the reported value, however our estimate of uncertainty is much larger than the reported uncertainty. From the radio light curves presented in Koopmans et al. (2000), we were unable to make a reliable time delay measurement.

– *HE 2149−2745:* We used the light curves presented in Burud et al. (2002a), which were made publicly available by Paraficz et al. (2006).

In Figs. 4.1 – 4.27, we have plotted the analyzed light curves. For each dataset, those light curves whose time delays with respect to the A light curve could be measured to a precision of better than 33.3% are shown shifted in time by the measured time delays. Also the mean values have been subtracted from all the displayed light curves to enable better comparison between their variability features. The photometric error bars are also shown.

Table 4.1: Time delay measurements of 24 gravitationally lensed quasars.

Object (Observational waveband(s))	Time delay	Reported value [day]	Our measurement [day]
(a) Q0142−100 (R)	Δt_{AB}	89 ± 11	?
(b) JVAS B0218+357 (8 & 15 GHz)	Δt_{AB}	$10.1^{+1.5}_{-1.6}$ (95% CI)	10.6 ± 1.5
(c) HE 0435−1223 (R)	Δt_{AB}	8.4 ± 2.1	9.3 ± 1.3
	Δt_{AC}	0.6 ± 2.3	0.7 ± 1.9
	Δt_{AD}	14.9 ± 2.1	13.5 ± 1.6
	Δt_{BC}	-7.8 ± 0.8	-7.3 ± 2.2
	Δt_{BD}	6.5 ± 0.7	6.1 ± 1.2
	Δt_{CD}	14.3 ± 0.8	12.4 ± 1.6
(d) SBS 0909+532 (r)	Δt_{AB}	-50^{+2}_{-4}	?
(e) RX J0911.4+0551 (I)	$\Delta t_{(A1+A2+A3)B}$	-146 ± 8 (2σ)	-143.2 ± 10.1
(f) FBQ 0951+2635 (R)	Δt_{AB}	16 ± 2	-5.0 ± 22.9
(g) Q0957+561 (r & g)	Δt_{AB}	417.4 ± 0.9	418.7 ± 1.5
(h) SDSS J1001+5027 (R)	Δt_{AB}	119.3 ± 3.3	121.2 ± 2.2
(i) SDSS J1004+4112 (R & r)	Δt_{AB}	-40.6 ± 1.8	-35.5 ± 2.5
	Δt_{AC}	-821.6 ± 2.1	-821.9 ± 12.7
	Δt_{BC}		-777.9 ± 12.8
(j) SDSS J1029+2623 (r)	$\Delta t_{A(B+C)}$	744 ± 10 (90% CI)	743.5 ± 8.9
(k) HE 1104−1805 (R & V)	Δt_{AB}	$-152.2^{+2.8}_{-3.0}$	-158.4 ± 6.2
(l) PG 1115+080 (R)	$\Delta t_{(A1+A2)B}$		-8.9 ± 8.4
	$\Delta t_{(A1+A2)C}$	-12	-18.3 ± 4.4
	Δt_{BC}	-16.4	-13.2 ± 9.0
(m) RX J1131−1231 (R)	Δt_{AB}	0.7 ± 1.0	0.9 ± 1.7
	Δt_{AC}	0.0 ± 1.3	-1.0 ± 1.5
	Δt_{AD}	90.6 ± 1.4	92.9 ± 1.5
	Δt_{BC}	-0.7 ± 1.5	0.7 ± 1.3
	Δt_{BD}	91.4 ± 1.2	91.6 ± 1.6
	Δt_{CD}	91.7 ± 1.5	90.7 ± 2.4
(n) SDSS J1206+4332 (R)	Δt_{AB}	111.3 ± 3	111.5 ± 2.0
(o) H1413+117 (r)	Δt_{AB}	-17 ± 3	-16.1 ± 14.0
	Δt_{AC}	-20 ± 4	-21.9 ± 12.1

Continued on next page

Table 4.1 – continued from previous page

Object (Observational waveband(s))	Time delay	Reported value [day]	Our measurement [day]
	Δt_{AD}	23 ± 4	22.6 ± 8.5
	Δt_{BC}		-47.7 ± 23.1
	Δt_{BD}		20.7 ± 18.9
	Δt_{CD}		29.7 ± 11.7
(p) B1422+231 (15 GHz)	Δt_{AB}	-1.5 ± 1.4	1.1 ± 3.9
	Δt_{AC}	7.6 ± 2.5	-0.3 ± 5.1
	Δt_{BC}	8.2 ± 2.0	-0.4 ± 6.6
(q) SBS 1520+530 (R)	Δt_{AB}	130 ± 3	125.8 ± 20.1
(r) CLASS B1600+434 (I)	Δt_{AB}	51 ± 4 (95% CI)	48.9 ± 30.4
(s) CLASS B1600+434 (8.5 GHz)	Δt_{AB}	47^{+5}_{-6}	?
(t) CLASS B1608+656 (8.5 GHz)	Δt_{AB}	$-31.5^{+2.0}_{-1.0}$	-30.0 ± 2.6
	Δt_{AC}		5.0 ± 3.0
	Δt_{AD}		46.1 ± 2.4
	Δt_{BC}	$36.0^{+1.5}_{-1.5}$	37.2 ± 3.8
	Δt_{BD}	$77.0^{+2.0}_{-1.0}$	77.5 ± 2.8
	Δt_{CD}		41.4 ± 3.3
(u) SDSS J1650+4251 (R)	Δt_{AB}	49.5 ± 1.9	63.8 ± 16.1
(v) PKS 1830−211 (8.6 GHz)	Δt_{AB}	26^{+4}_{-5}	32.9 ± 5.8
(w) WFI J2033−4723 (R)	Δt_{AB}	-35.5 ± 1.4	-36.0 ± 1.6
	Δt_{AC}		25.1 ± 3.8
	Δt_{BC}	$62.6^{+4.1}_{-2.3}$	66.0 ± 3.5
(x) HE 2149−2745 (V)	Δt_{AB}	103 ± 12	84.3 ± 19.4
(y) HS 2209+1914 (R)	Δt_{AB}	-20.0 ± 5	-23.5 ± 7.3

References for data. (a) Koptelova et al. (2012); (b) Cohen et al. (2000); (c) Courbin et al. (2011); (d) Goicoechea et al. (2008), Hainline et al. (2013); (e) Hjorth et al. (2002); (f) Jakobsson et al. (2005); (g) Shalyapin et al. (2012); (h) Rathna Kumar et al. (2013); (i) Fohlmeister et al. (2007), Fohlmeister et al. (2008); (j) Fohlmeister et al. (2013); (k) Poindexter et al. (2007); (l) Tsvetkova et al. (2010); (m) Tewes et al. (2013b); (n) Eulaers et al. (2013); (o) Goicoechea & Shalyapin (2010); (p) Patnaik & Narasimha (2001); (q) Burud et al. (2002b); (r) Burud et al. (2000); (s) Koopmans et al. (2000); (t) Fassnacht et al. (1999), Fassnacht et al. (2002); (u) Vuissoz et al. (2007); (v) Lovell et al. (1998); (w) Vuissoz et al. (2008); (x) Burud et al. (2002a); (y) Eulaers et al. (2013).

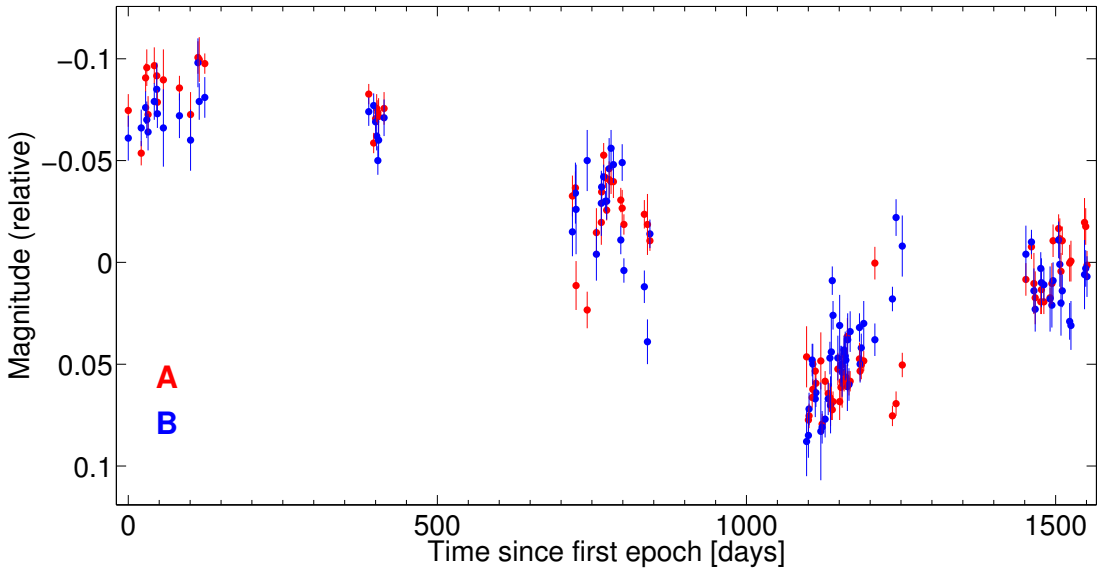

Figure 4.1: *R*-band light curves of Q0142−100 using data from Koptelova et al. (2012).

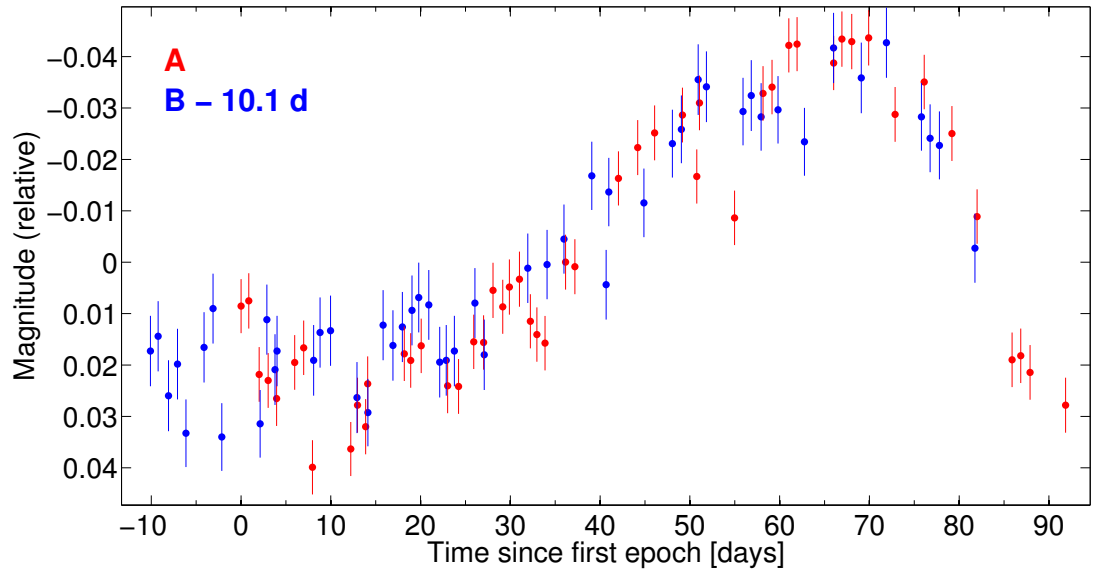

Figure 4.2: 8 GHz light curves of JVAS B0218+357 using data from Cohen et al. (2000).

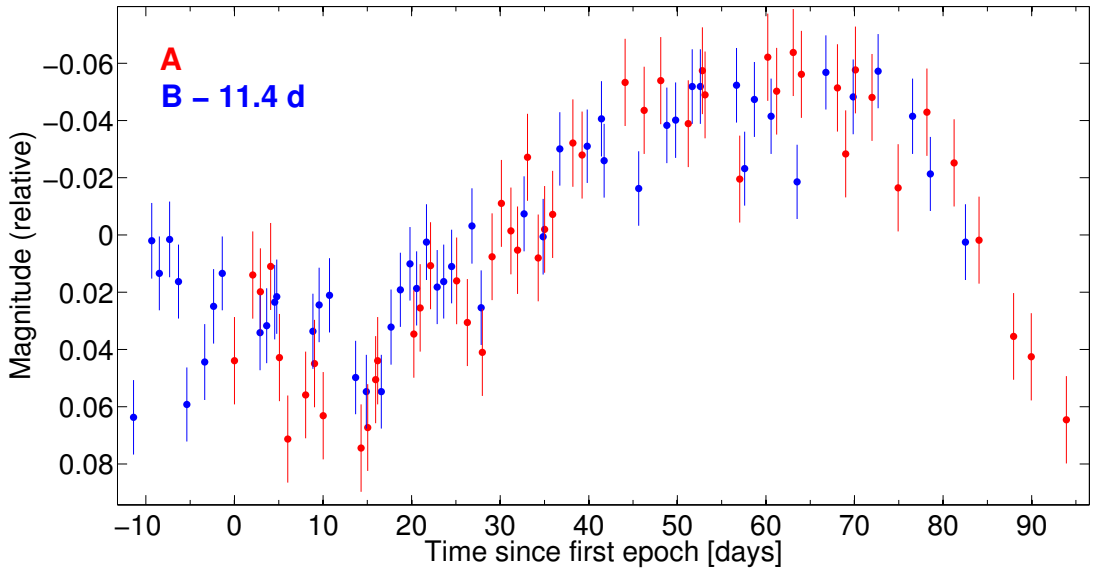

Figure 4.3: 15 GHz light curves of JVAS B0218+357 using data from Cohen et al. (2000).

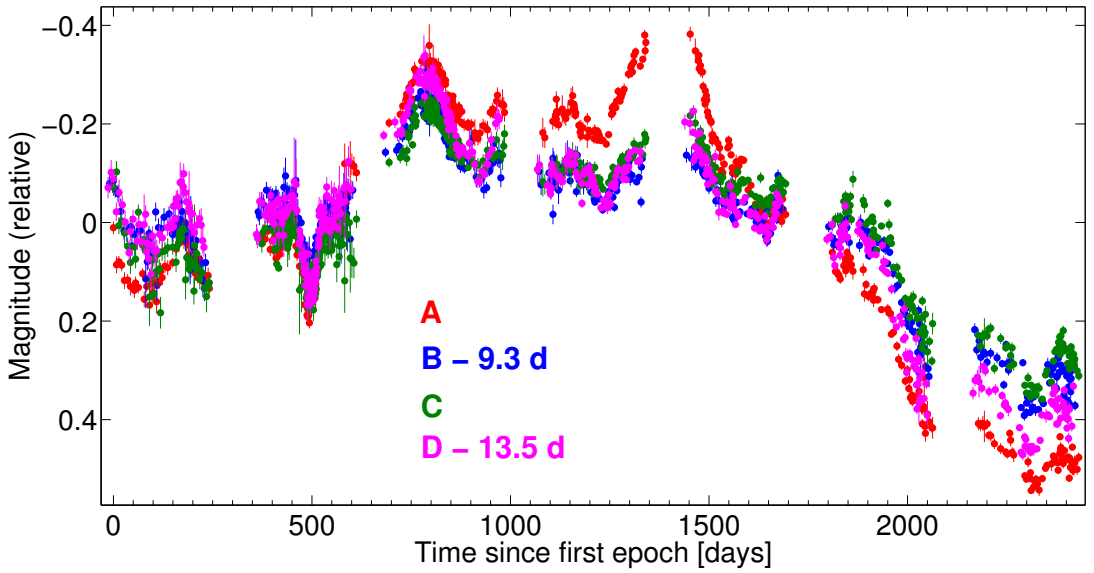

Figure 4.4: *R*-band light curves of HE 0435−1223 using data from Courbin et al. (2011).

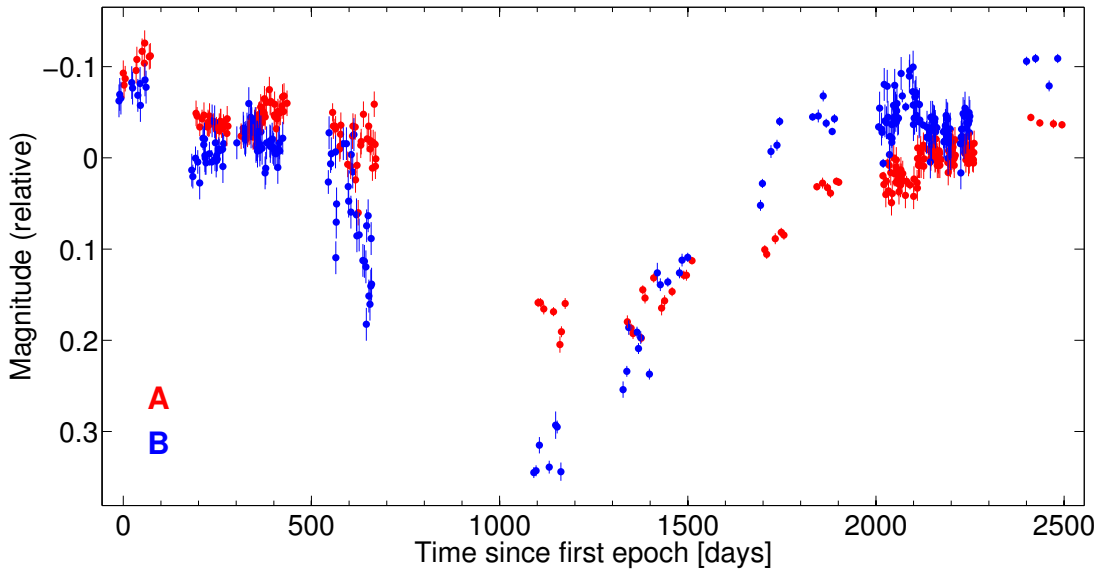

Figure 4.5: *r*-band light curves of SBS 0909+532 using data from Goicoechea et al. (2008) and Hainline et al. (2013).

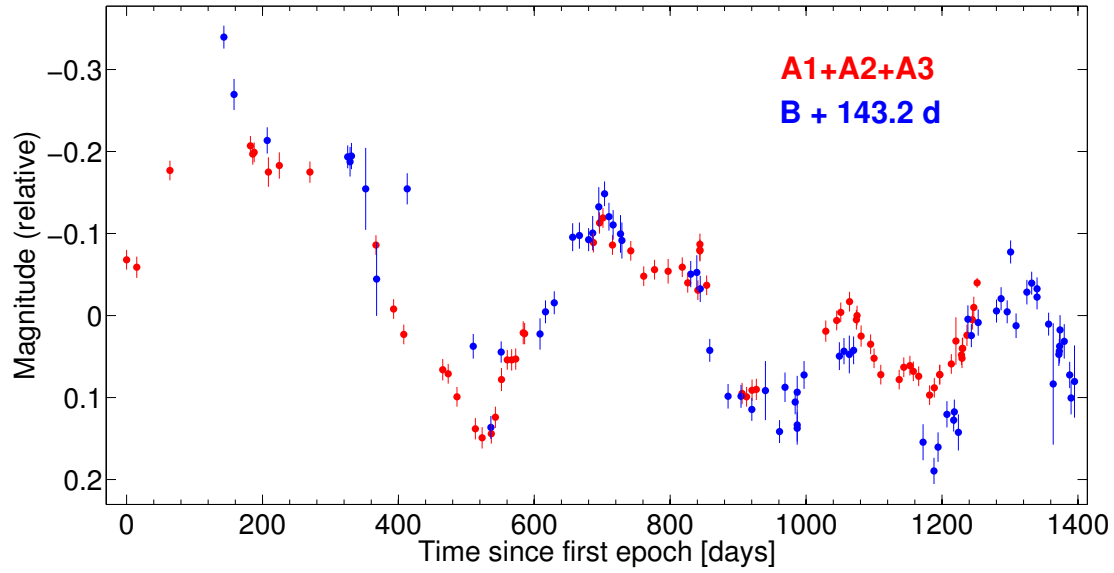

Figure 4.6: *I*-band light curves of RX J0911.4+0551 using data from Hjorth et al. (2002).

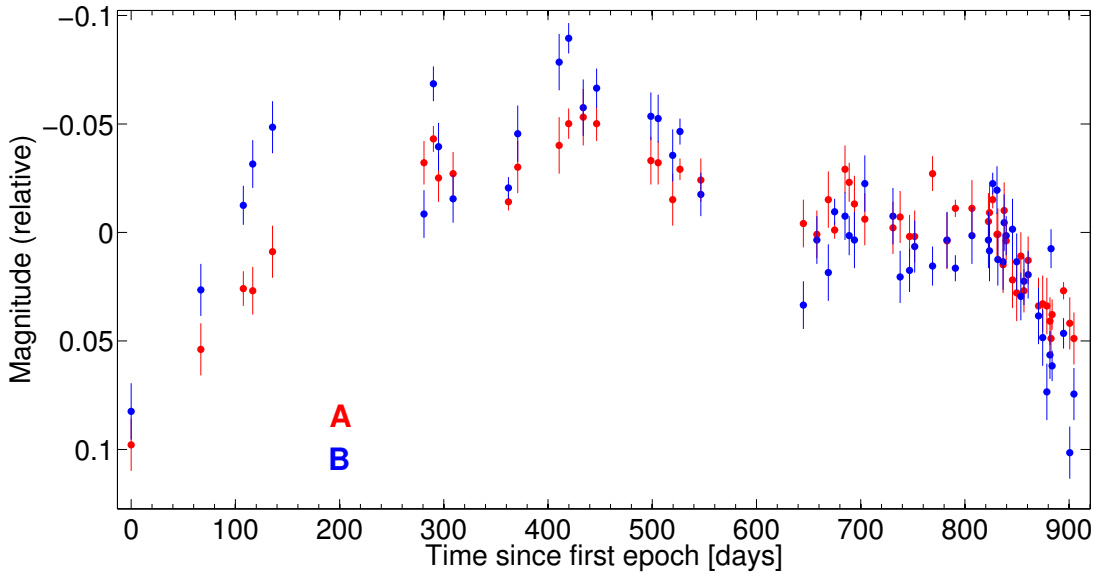

Figure 4.7: *R*-band light curves of FBQ 0951+2635 using data from Jakobsson et al. (2005).

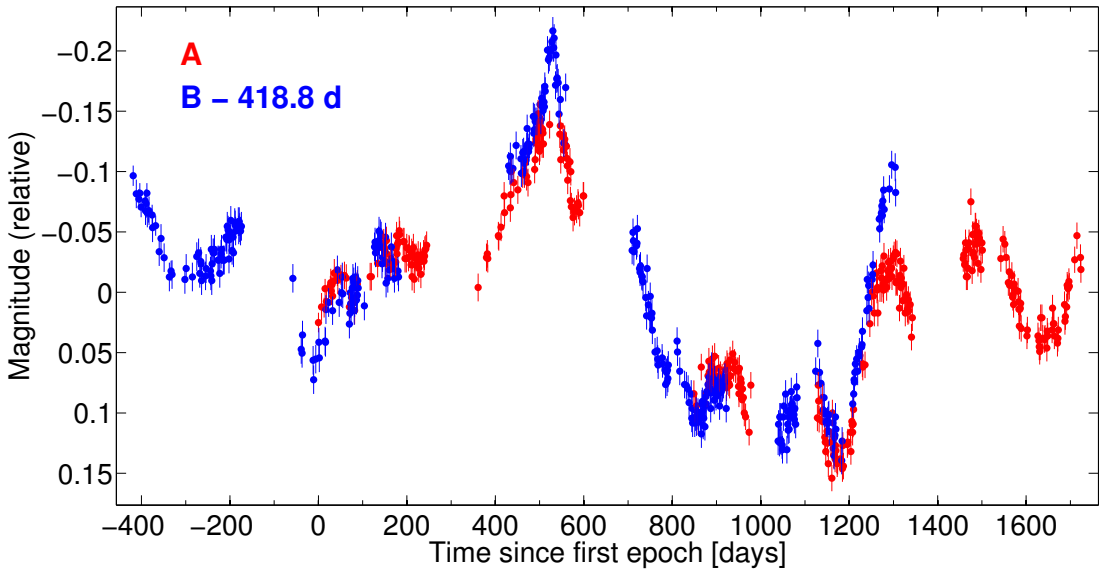

Figure 4.8: *r*-band light curves of Q0957+561 using data from Shalyapin et al. (2012).

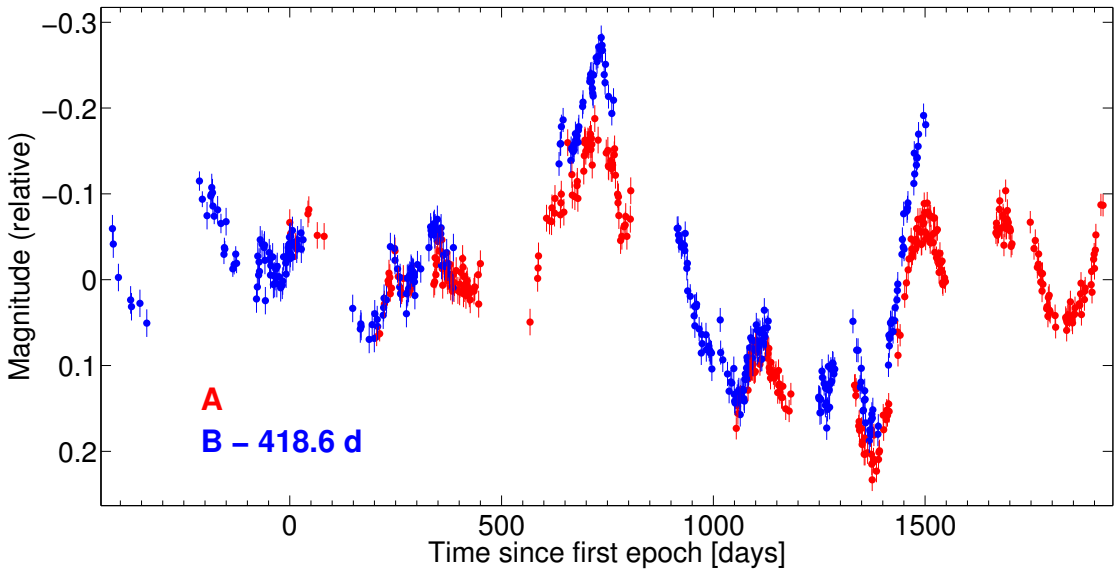

Figure 4.9: *g*-band light curves of Q0957+561 using data from Shalyapin et al. (2012).

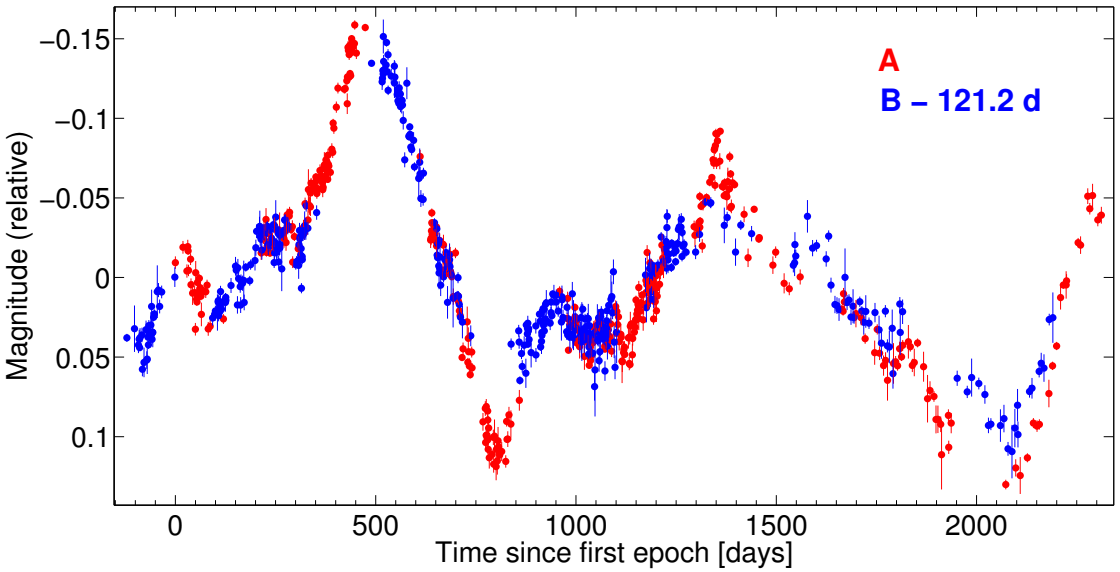

Figure 4.10: *R*-band light curves of SDSS J1001+5027 using data from Rathna Kumar et al. (2013).

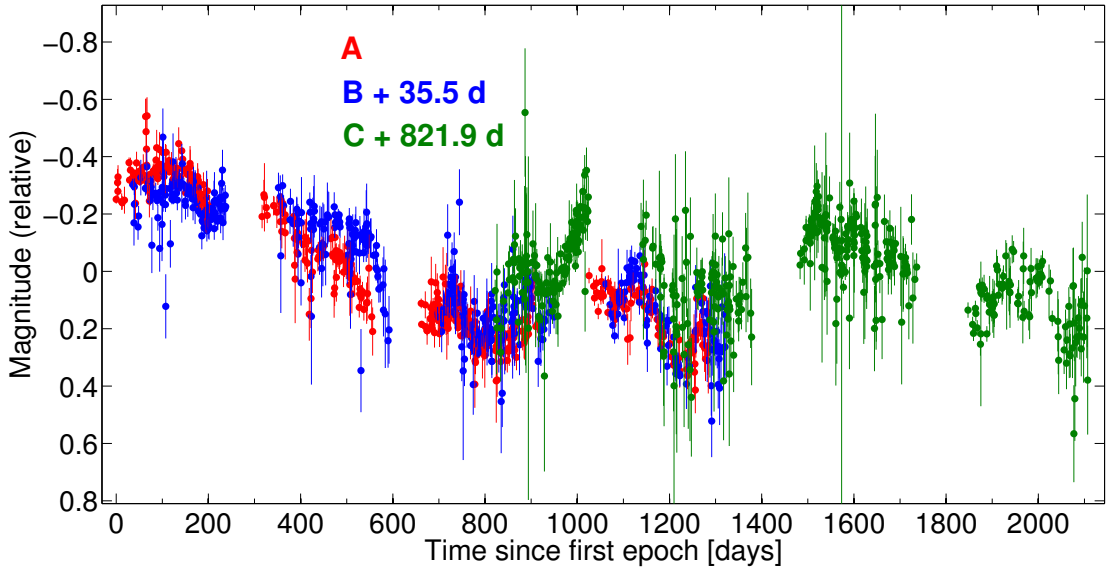

Figure 4.11: Light curves, comprising observations in *R*-band and *r*-band, of images A and B of SDSS J1004+4112 using data from Fohlmeister et al. (2007) and Fohlmeister et al. (2008).

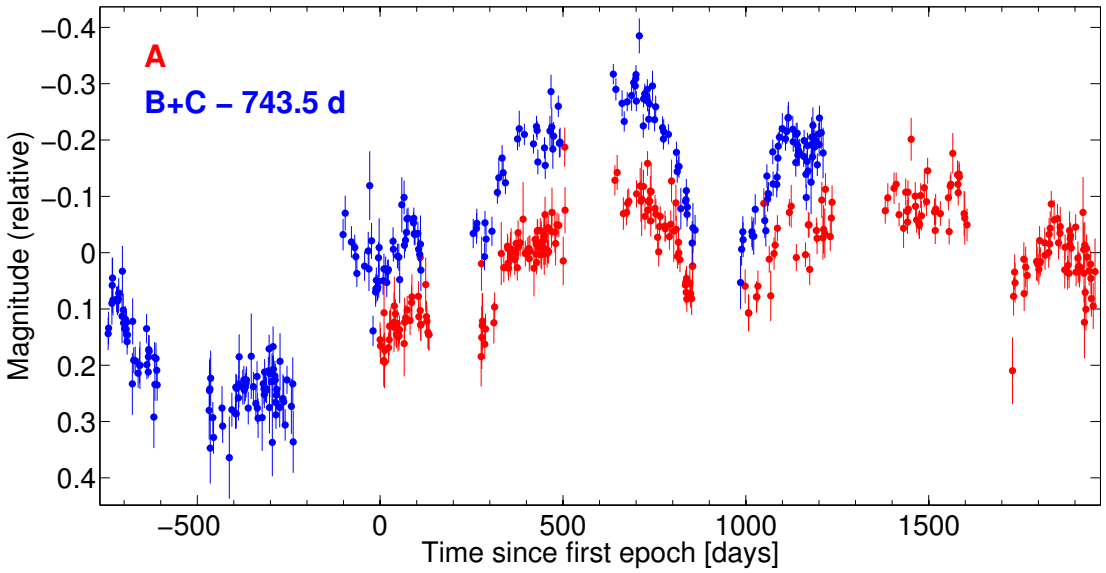

Figure 4.12: *r*-band light curves of SDSS J1029+2623 using data from Fohlmeister et al. (2013).

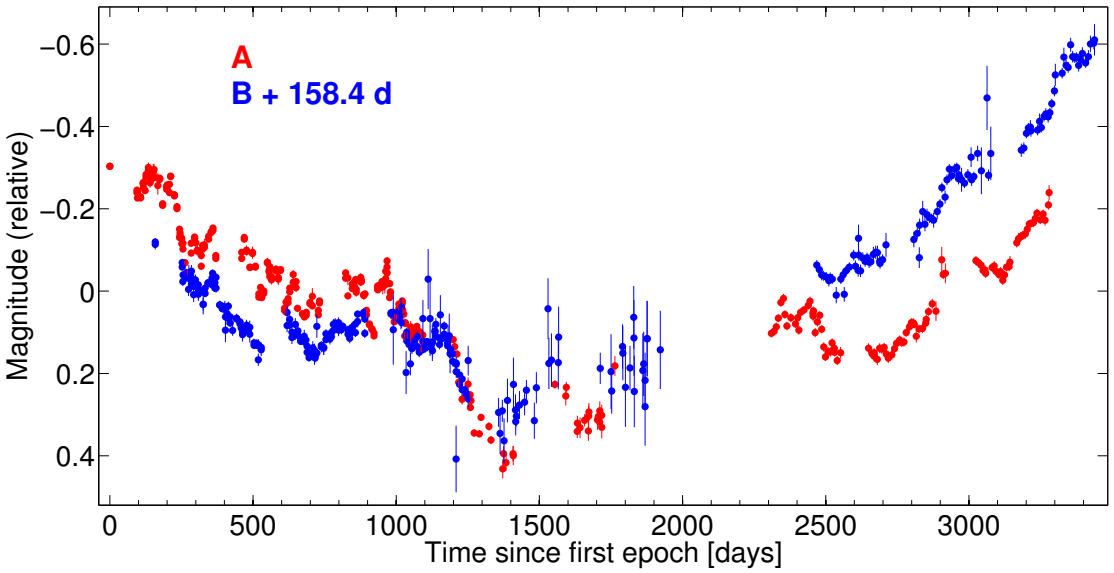

Figure 4.13: Light curves, comprising observations in R-band and V-band, of HE 1104−1805 using data from Poindexter et al. (2007).

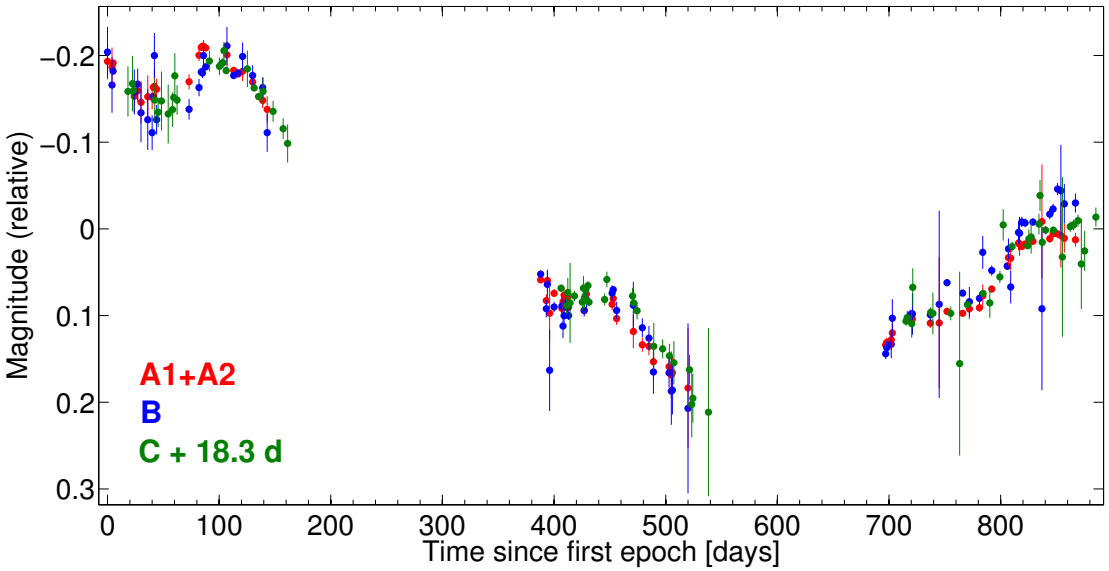

Figure 4.14: R-band light curves of PG 1115+080 using data from Tsvetkova et al. (2010).

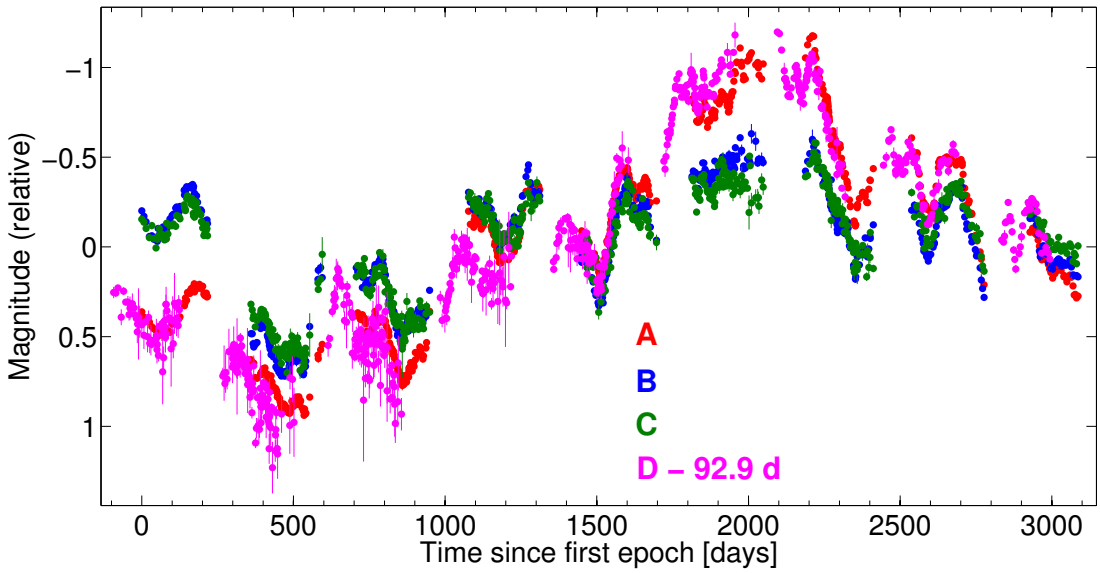

Figure 4.15: *R*-band light curves of RX J1131−1231 using data from Tewes et al. (2013b).

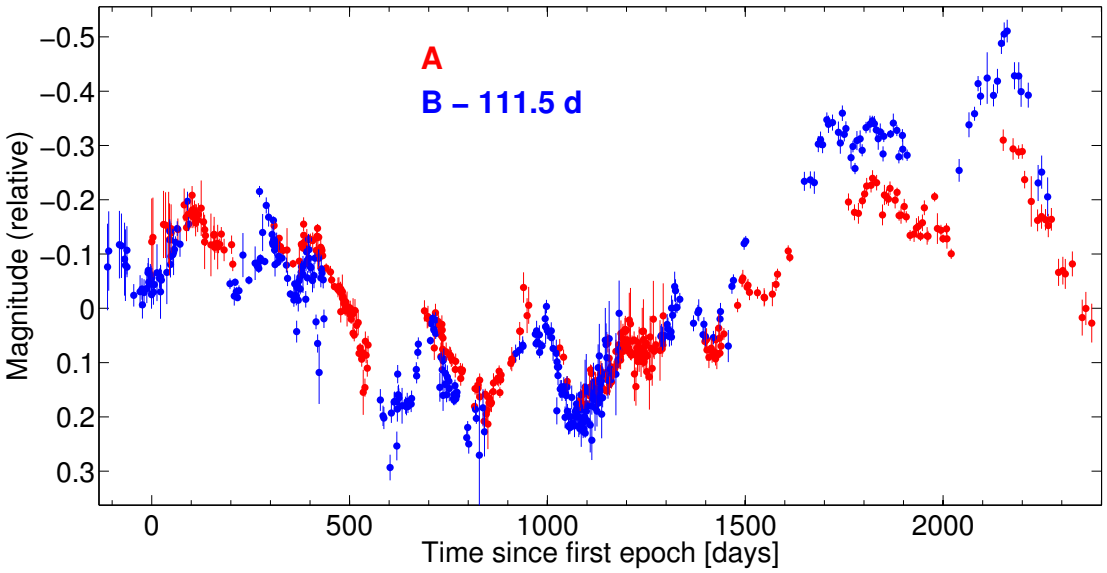

Figure 4.16: *R*-band light curves of SDSS J1206+4332 using data from Eulaers et al. (2013).

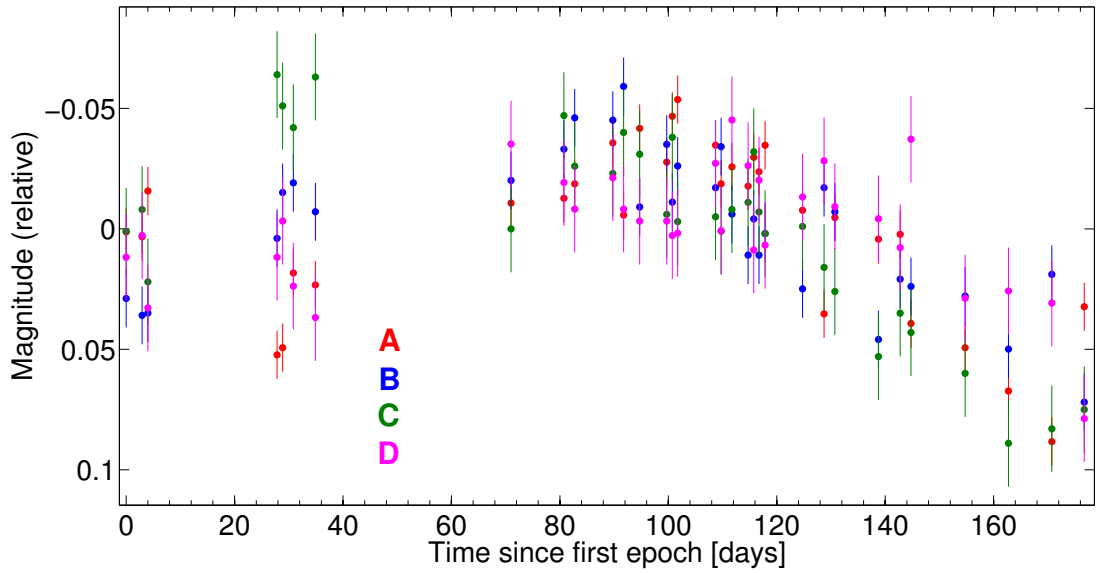

Figure 4.17: *r*-band light curves of H1413+117 using data from Goicoechea & Shalyapin (2010).

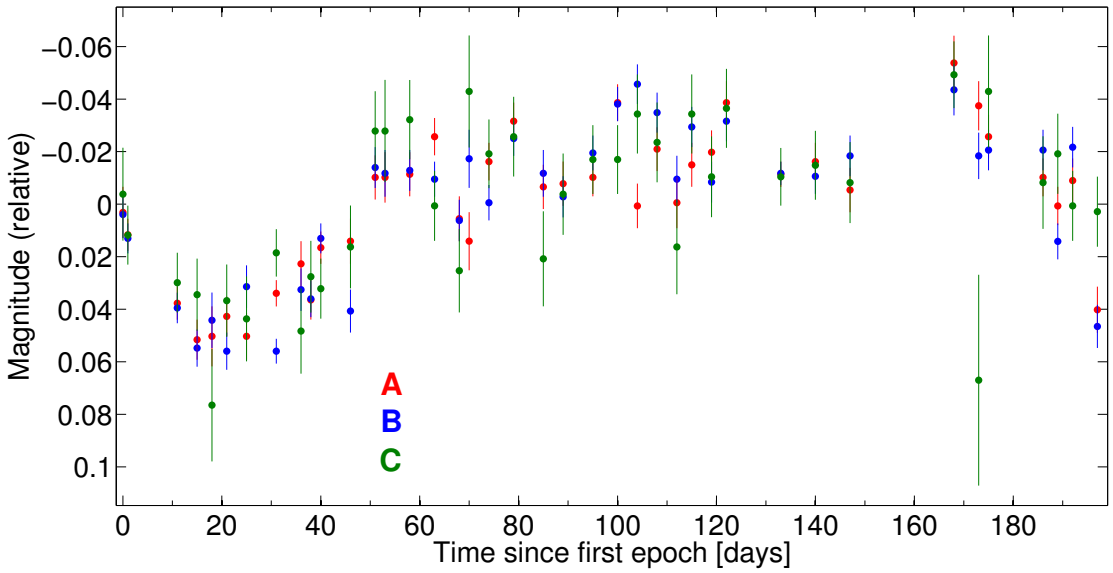

Figure 4.18: 15 GHz light curves of B1422+231 using data from Patnaik & Narasimha (2001).

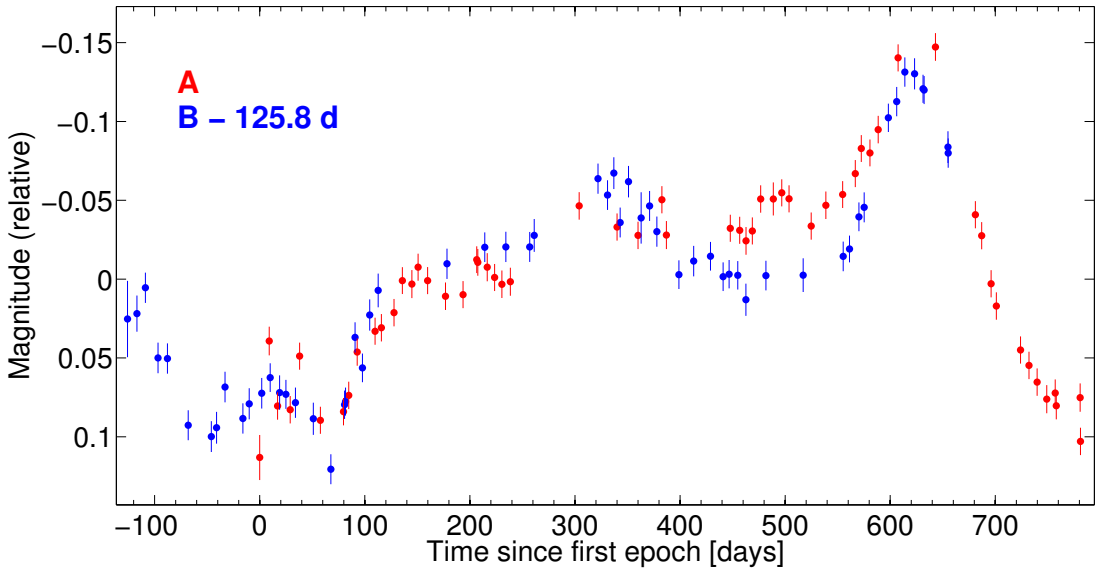

Figure 4.19: *R*-band light curves of SBS 1520+530 using data from Burud et al. (2002b).

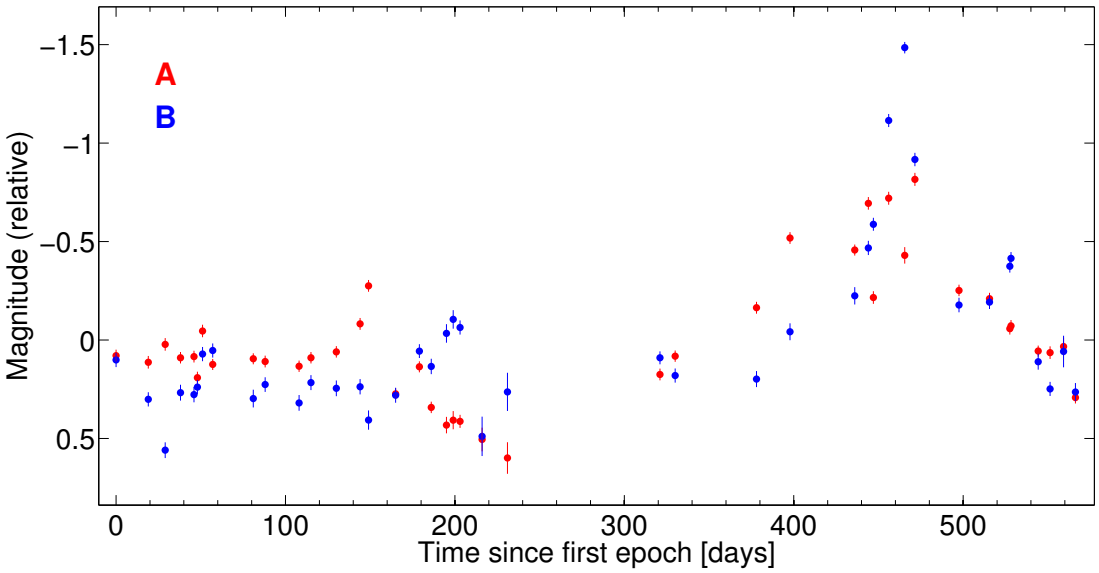

Figure 4.20: *I*-band light curves of CLASS B1600+434 using data from Burud et al. (2000).

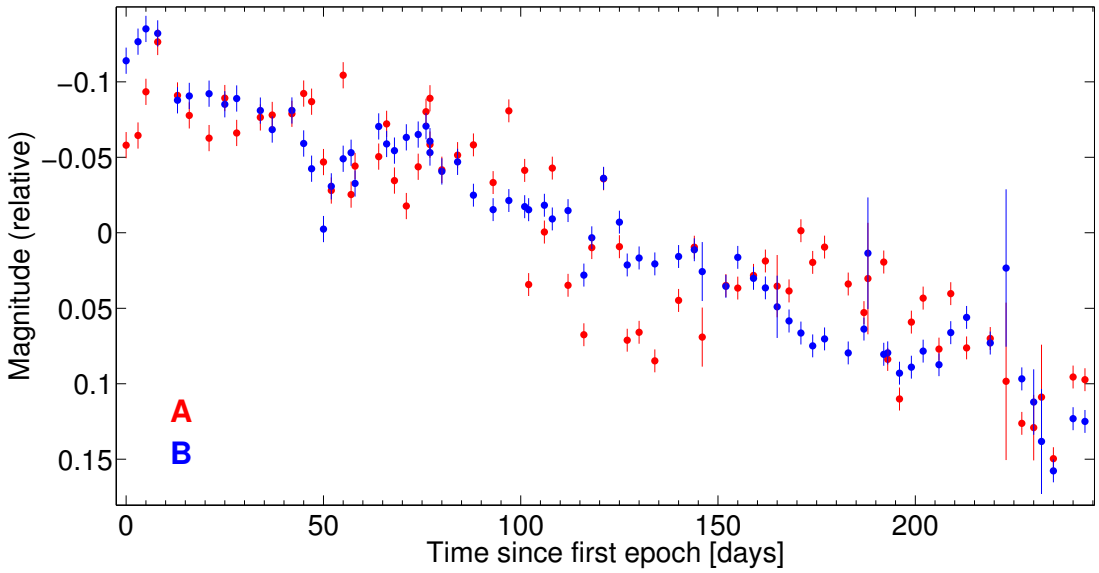

Figure 4.21: 8.5 GHz light curves of CLASS B1600+434 using data from Koopmans et al. (2000).

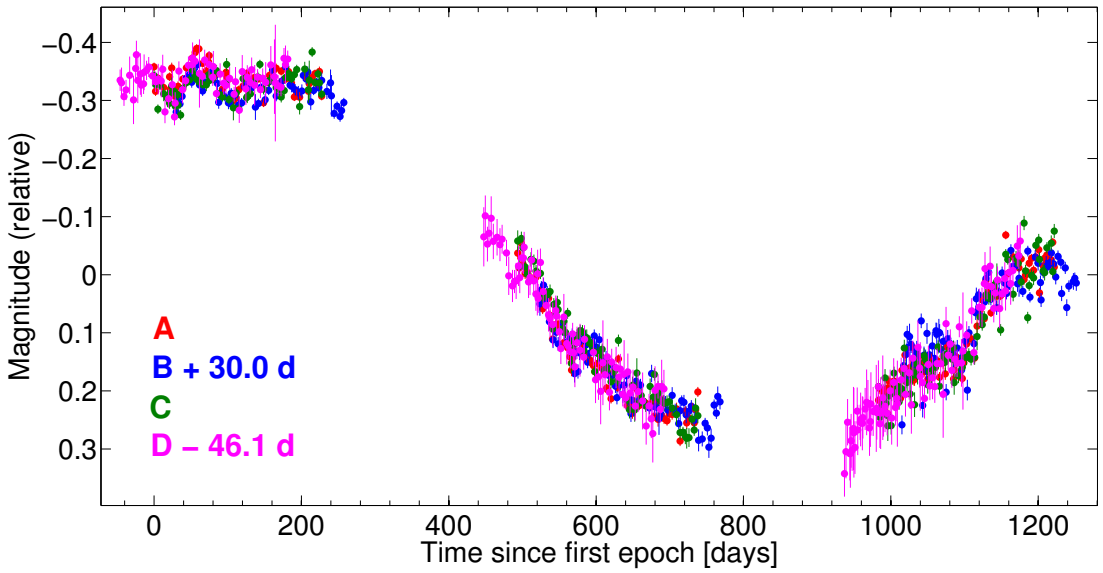

Figure 4.22: 8.5 GHz light curves of CLASS B1608+656 using data from Fassnacht et al. (1999) and Fassnacht et al. (2002).

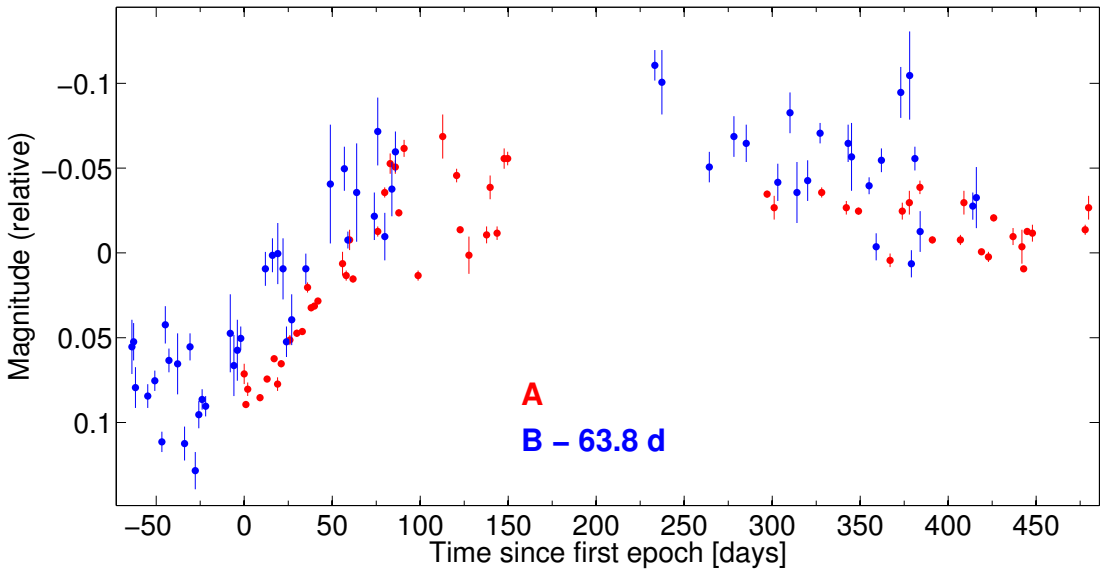

Figure 4.23: *R*-band light curves of SDSS J1650+4251 using data from Vuissoz et al. (2007).

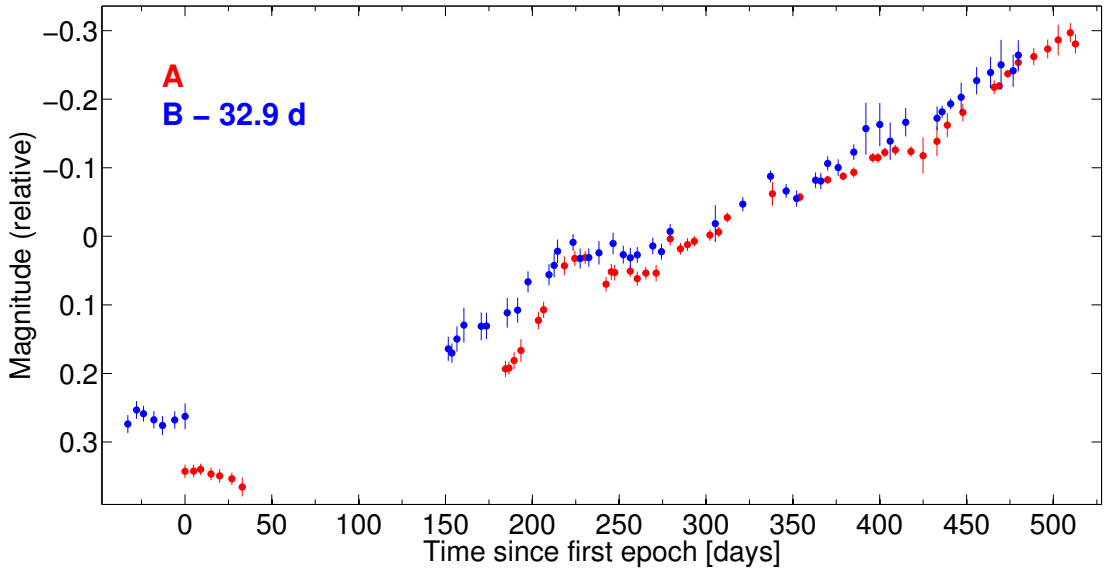

Figure 4.24: 8.6 GHz light curves of PKS 1830−211 using data from Lovell et al. (1998).

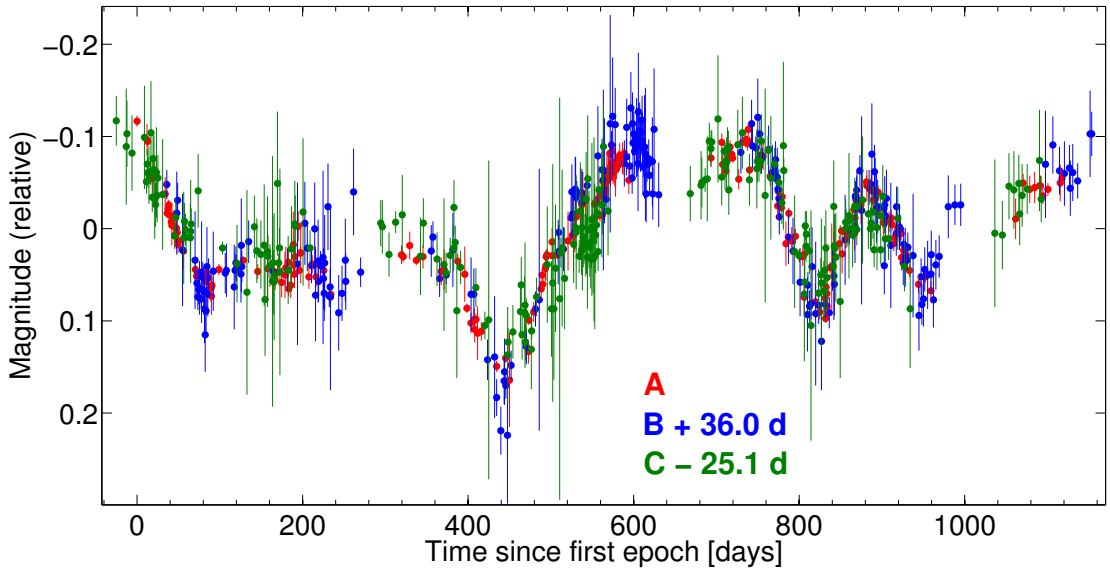

Figure 4.25: *R*-band light curves of WFI J2033−4723 using data from Vuissoz et al. (2008).

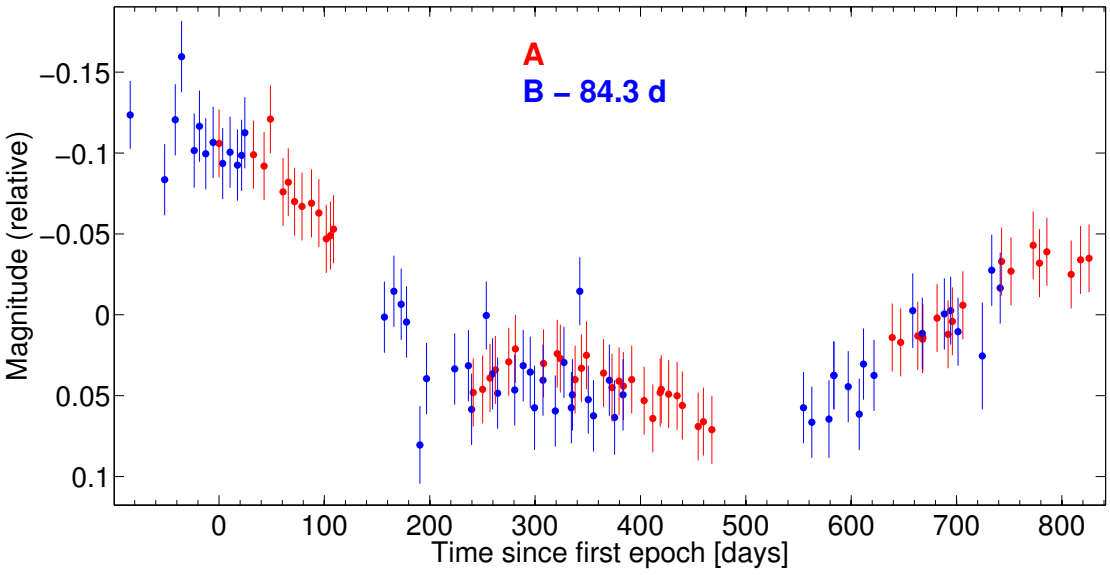

Figure 4.26: *V*-band light curves of HE 2149−2745 using data from Burud et al. (2002a).

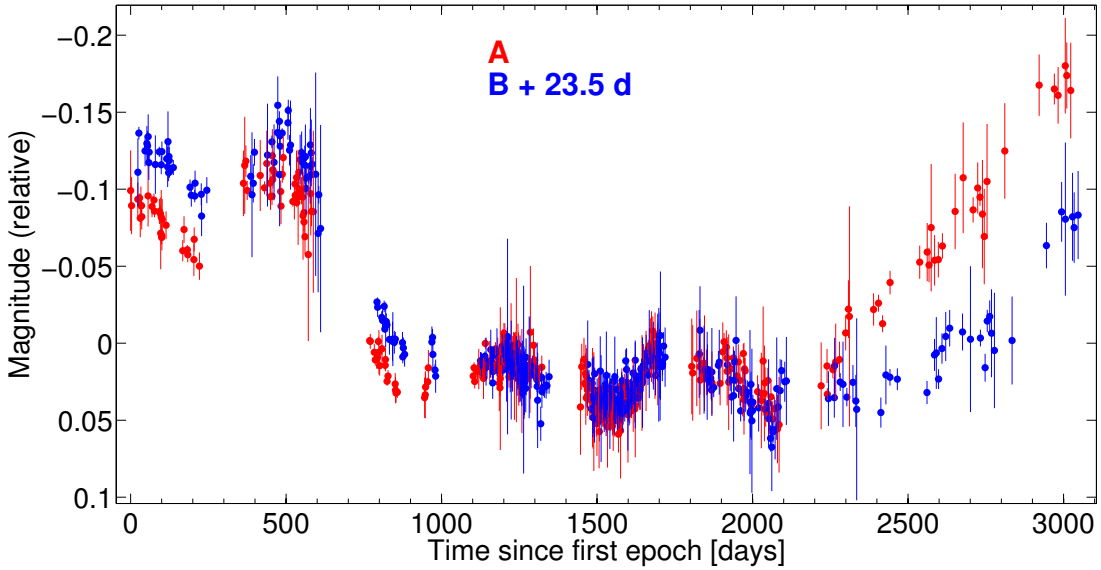

Figure 4.27: *R*-band light curves of HS 2209+1914 using data from Eulaers et al. (2013).

Chapter 5

The Hubble constant from well-measured time-delay lenses

In the previous chapter, we have presented a homogeneous analysis of the published light curves of 24 gravitationally lensed quasars. This analysis used the "difference-smoothing technique" developed during the course of the thesis (Rathna Kumar et al. 2013) and described in Chapter 5. This homogeneous analysis also gives the errors associated with the measured time delays, the details of which are given in the previous chapter. In this chapter, we use a subsample of the 24 systems, that have at least one time delay between the images adjacent to each other in terms of arrival-time order measured to a precision of better than 33.3% including systematic errors. We use here such a carefully selected sub-sample of sources to infer H_0.

5.1 Sample selection

Of the 24 systems analysed in the last chapter, 18 of them had light curves of sufficiently good quality to enable the measurement of at least one time delay between the images, adjacent to each other in terms of arrival-time order, to a precision of better than 33.3% (which corresponds to a 3σ detection of time delay). The six systems which did not satisfy this criterion are Q0142−100 (UM673), SBS 0909+532, FBQ 0951+2635, H1413+117, JVAS B1422+231 and CLASS B1600+434. In addition to these 18 systems, we also have SDSS J0806+2006, the unpublished time delay for which was presented in Sect. 3.5. We thus have a total of 19 systems.

Of the 19 systems, we did not model the mass distribution for 7 systems for the following reasons. HS 2209+1914 does not have known lens redshift. SDSS J1001+5027, SDSS

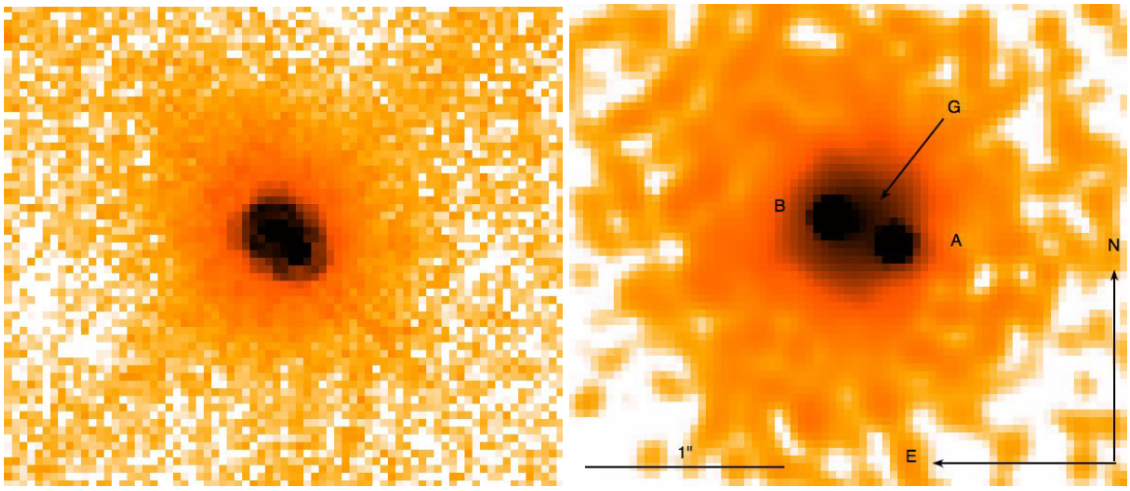

Figure 5.1: *Left:* HST image of JVAS B0218+357. *Right:* Deconvolved image. (Image courtesy: Sluse et al. 2012)

J1206+4332 and SDSS J1650+4251 do not have accurate astrometric data measured from Hubble Space Telescope (HST) images or ground-based imaging with adaptive optics. Although the astrometry of JVAS B0218+357, having a small image separation of $0.33''$, has been measured from HST images by Sluse et al. (2012), the authors warn about possibly large systematic errors in the published astrometry. Meylan et al. (2005) through adaptive optics imaging confirm the presence of a second extended object of unknown redshift along the line of sight to PKS 1830−211, in addition to the known lensing spiral galaxy. SDSS J1029+2623 is a three-image cluster lens with highly complex mass distribution (see, Oguri et al. 2013) and hence not amenable to lens-modelling following the simplistic approach described below. We are thus left with a final sample of 12 lens systems.

5.2 H_0 from pixellated modelling of 12 gravitational lenses

To perform mass-modelling of the remaining 12 systems to infer H_0, we used the publicly available PixeLens[1] code (Saha & Williams 2004), which builds an ensemble of pixellated mass maps compatible with the input data for a given system, which is comprised of the redshifts of the quasar and the lensing galaxy, the arrival-time order of the images, their astrometry relative to the center of the main lensing galaxy and the known time delays between the images adjacent to each other in terms of arrival-time order. In case of quadruple lenses in which only some of the time delays are known, it is still possible to guess the

[1] http://www.qgd.uzh.ch/projects/pixelens/

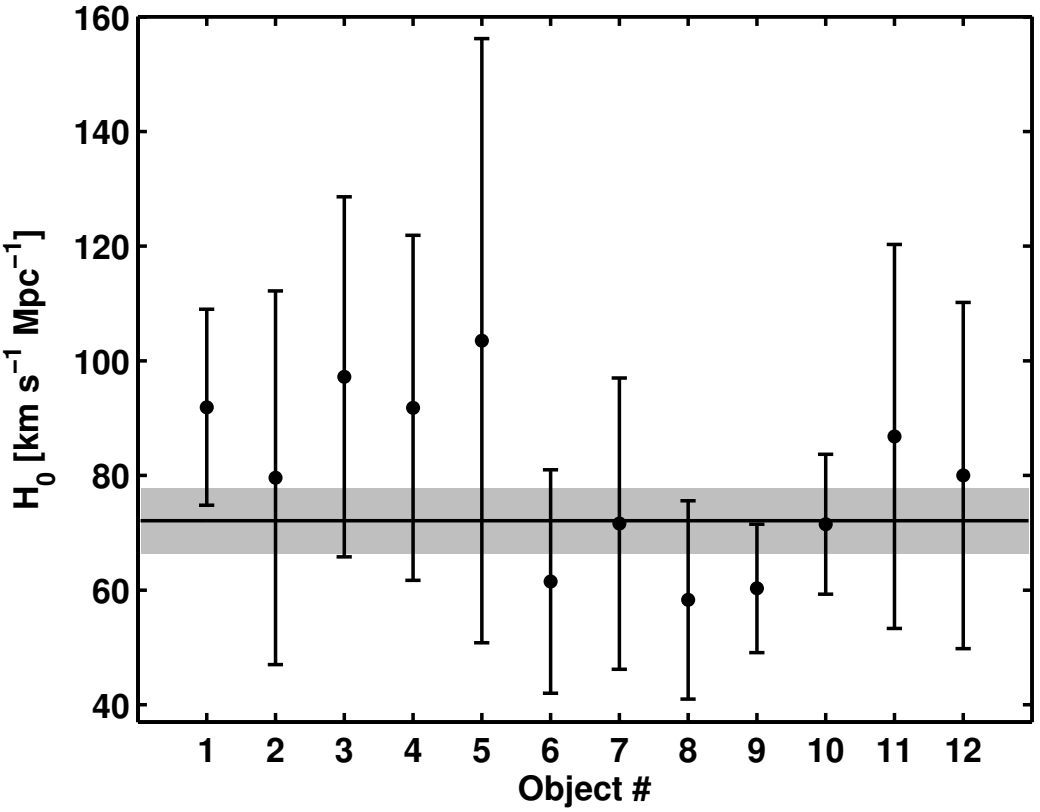

Figure 5.2: The H_0 estimates and their 1σ uncertainties for the 12 gravitational lenses – *(1)* HE 0435−1223, *(2)* RX J0911.4+0551, *(3)* Q0957+561, *(4)* SDSS J1004+4112, *(5)* HE 1104−1805, *(6)* PG 1115+080, *(7)* RX J1131−1231, *(8)* SBS 1520+530, *(9)* CLASS B1608+656, *(10)* WFI J2033−4723, *(11)* HE 2149−2745 and *(12)* SDSS J0806+2006. The best estimate of H_0 and its 1σ confidence interval, inferred through maximum-likelihood analysis, are represented by the horizontal line and the gray shaded region respectively.

arrival-time order of the images by following certain simple rules (see, Saha & Williams 2003).

We model all lenses, except SDSS J1004+4112, such that their mass profiles have inversion symmetry about the lens center, including any companion galaxy to the main lensing galaxy as a point mass. The lensing cluster in SDSS J1004+4112 consists of several galaxies besides the main lensing galaxy (see, Inada et al. 2005) and hence was modelled without assuming inversion symmetry about the lens center.

PixeLens builds models such that their projected density profiles are steeper than $|\theta|^{-\gamma_{min}}$, the default value of γ_{min} being 0.5. In this work, we relax this restriction and set $\gamma_{min} = 0$, for those lenses in our sample in which the largest angular separation between

the images is greater than $3''$. The lenses in our sample which satisfy this criterion are RX J0911.4+0551, Q0957+561, SDSS J1004+4112, HE 1104−1805 and RX J1131−1231. A large image separation implies that there is significant lensing action from the cluster of which the main lensing galaxy is part of, in which case the projected density profile can be shallower than $|\theta|^{-0.5}$.

For each system, we build an ensemble of 100 models, corresponding to 100 values of H_0. The mean of the 100 values gives the best estimate of H_0, the uncertainty of which is the standard deviation of the 100 values. This uncertainty includes only the uncertainty in the mass model. PixeLens assumes that the uncertainty in the input priors to be negligibly small, which is a reasonable assumption for the redshifts, if they are spectroscopically measured and astrometry, if measured from HST or ground-based adaptive optics imaging. However the measured time delays have finite uncertainties, which need to be propagated into the uncertainty of the estimated H_0. We achieve this by summing the fractional uncertainty arising from mass modelling and the fractional uncertainty in the measured time delay in quadrature. In case of quadruple lenses having more than one known time delay, the fractional uncertainty component arising from time delay measurement for the system is computed by averaging the fractional uncertainties of the independent time delays in quadrature.

In order to include the effects of external shear, an approximate direction of the shear axis needs to be specified and PixeLens will search for solutions within 45° of the specified direction. Since there exists no simple rule to guess the direction of the external shear for a given system, for each system, we repeat the modelling, specifying the approximate direction of the shear axis as 90°, 45°, 0° and −45°. (Note that, in this instance, specifying θ and θ+180° are equivalent.) We thus obtain four estimates of H_0 and their uncertainties. The final estimate of H_0 and its uncertainty are found using maximum likelihood analysis, optimising their values such as to maximise the joint posterior probability of these two parameters for the sample consisting of the four H_0 values and their uncertainties (as in, Barnabè et al. 2011, Eq. 7). In optimising the value of the uncertainty, we choose the minimum limit to be the smallest of the four uncertainties. For each system, we found that the H_0 estimates for the various shear directions are consistent with each other within 2σ and hence the uncertainty of the final estimate of H_0 turns out to be the smallest uncertainty.

The input priors for each system and the resulting H_0 estimates are summarised in Table 5.1, wherein

– the QSO images are listed in arrival-time order,

– ‘P.M.’ is abbreviation for point mass,

– the astrometry of the QSO images and point masses are specified with respect to the center of the main lensing galaxy and

– the time delay of a given image is listed (if measured to a precision of better than 33.3%) with respect to the previous image in terms of arrival-time order.

In Fig. 5.2, we plot the H_0 estimates from the 12 lenses, all of which are seen to agree with each other within 2σ. To combine the 12 independent estimates into a best estimate of H_0, we again employ maximum likelihood analysis, as described above. However, in this case, in optimising the value of the uncertainty of the best estimate of H_0, the minimum limit is chosen to be the uncertainty of the weighted average of the 12 values. We infer a value of H_0 of 72.1 ± 5.7 km s^{-1} Mpc^{-1} (1σ uncertainty, 7.9% precision) for a spatially flat universe having $\Omega_m = 0.3$ and $\Omega_\Lambda = 0.7$. The reason for employing maximum likelihood analysis in this case, rather than taking a simple weighted average is to detect the presence of any unmodelled uncertainties. However as can be seen from Fig. 5.2, the H_0 estimates from the individual systems all agree with each other within 2σ and hence the H_0 value inferred above through maximum likelihood analysis is only marginally different compared to the weighted average.

As an instructive exercise, we modelled all the lenses without allowing for external shear and found a H_0 value of 67.0 ± 5.6 km s^{-1} Mpc^{-1}, which agrees with the value found above within the error bar, presumably because the biases resulting from not accounting for external shear for the different lenses in the sample tend to average out. For the source and lens redshifts of the current sample, we find the H_0 estimate to decrease by 6.6% for Einstein-de Sitter universe ($\Omega_m = 1.0$ and $\Omega_\Lambda = 0.0$) and increase by 2.1% for an open universe having $\Omega_m = 0.3$ and $\Omega_\Lambda = 0.0$, thus illustrating the low level of dependence of the inferred value of H_0 on the precise values of Ω_m and Ω_Λ.

In Figs. 5.3 – 5.14, we have displayed the high-resolution images for the modelled systems from which their astrometry were derived.

Table 5.1: Summary of input data to PixeLens and resulting H_0 estimates.

Object, z_l, z_s	Image / P.M.	ΔRA [″]	ΔDec [″]	Time delay [day]	H_0 [km s^{-1} Mpc^{-1}]
HE 0435−1223[1]	A	1.1706	0.5665		91.9 ± 17.1
$z_l = 0.4546$[2]	C	−1.2958	−0.0357		
$z_s = 1.689$[3]	B	−0.3037	1.1183	7.3 ± 2.2	
	D	0.2328	−1.0495	6.1 ± 1.2	
RX J0911.4+0551[4]	B	−2.2662	0.2904		79.6 ± 32.6
$z_l = 0.769$[5]	A2	0.9630	−0.0951	143.2 ± 10.1	
$z_s = 2.800$[6]	A1	0.7019	−0.5020		
	A3	0.6861	0.4555		
	P.M.	−0.7582	0.6658		
Q0957+561[7]	A	1.408	5.034		97.2 ± 31.4
$z_l = 0.361$[8]	B	0.182	−1.018	418.7 ± 1.5	
$z_s = 1.41$[8]					
SDSS J1004+4112[9]	C	3.925	−8.901		91.8 ± 30.1
$z_l = 0.68$[10]	B	−8.431	−0.877	777.9 ± 12.8	
$z_s = 1.734$[11]	A	−7.114	−4.409	35.5 ± 2.5	
	D	1.285	5.298		
HE 1104−1805[4]	B	1.9289	−0.8242		103.5 ± 52.7
$z_l = 0.729$[12]	A	−0.9731	0.5120	158.4 ± 6.2	
$z_s = 2.319$[13]					
PG 1115+080[4]	C	−0.3813	1.3442		61.5 ± 19.5
$z_l = 0.3098$[14]	A1	0.9473	−0.6896	18.3 ± 4.4	
$z_s = 1.722$[15]	A2	1.0959	−0.2315		
	B	−0.7218	−0.6156		
RX J1131−1231[16]	B	−2.076	0.662		71.6 ± 25.4
$z_l = 0.295$[17]	C	−1.460	−1.632		
$z_s = 0.658$[17]	A	−2.037	−0.520		
	D	1.074	0.356	92.9 ± 1.5	
	P.M.	−0.097	0.614		
SBS 1520+530[4]	A	−1.1395	0.3834		58.3 ± 17.3
$z_l = 0.761$[18]	B	0.2879	−0.2691	125.8 ± 20.1	

Continued on next page

Table 5.1 – continued from previous page

Object, z_l, z_s	Image / P.M.	ΔRA [″]	ΔDec [″]	Delay [day]	H_0 [km s^{-1} Mpc^{-1}]
$z_s = 1.855$[19]					
CLASS B1608+656[4]	B	1.2025	−0.8931		60.3 ± 11.2
$z_l = 0.6304$[20]	A	0.4561	1.0647	30.0 ± 2.6	
$z_s = 1.394$[21]	C	1.2044	0.6182		
	D	−0.6620	−0.1880	41.4 ± 3.3	
	P.M.	0.7382	0.1288		
WFI J2033−4723[22]	B	1.4388	−0.3113		71.5 ± 12.2
$z_l = 0.661$[23]	A1	−0.7558	0.9488	36.0 ± 1.6	
$z_s = 1.66$[24]	A2	−0.0421	1.0643		
	C	−0.6740	−0.5891	25.1 ± 3.8	
HE 2149−2745[4]	A	−0.7198	−1.1498		86.8 ± 33.5
$z_l = 0.603$[25]	B	0.1703	0.2963	84.3 ± 19.4	
$z_s = 2.033$[26]					
SDSS J0806+2006[27]	A	0.918	0.514		80.0 ± 30.2
$z_l = 0.573$[25]	B	−0.398	−0.187	54.2 ± 6.8	
$z_s = 1.540$[28]					
Combined					72.1 ± 5.7

References for astrometry, lens redshift and source redshift. [1] Courbin et al. (2011); [2] Morgan et al. (2005); [3] Wisotzki et al. (2002); [4] Sluse et al. (2012); [5] Kneib et al. (2000); [6] Bade et al. (1997); [7] Fadely et al. (2010); [8] Walsh et al. (1979); [9] Inada et al. (2005); [10] Oguri et al. (2004); [11] Inada et al. (2003); [12] Lidman et al. (2000); [13] Smette et al. (1995); [14] Tonry (1998); [15] Weymann et al. (1980); [16] Suyu et al. (2013a); [17] Sluse et al. (2003); [18] Auger et al. (2008); [19] Chavushyan et al. (1997); [20] Myers et al. (1995); [21] Fassnacht et al. (1996); [22] Vuissoz et al. (2008); [23] Eigenbrod et al. (2006); [24] Morgan et al. (2004); [25] Eigenbrod et al. (2007); [26] Wisotzki et al. (1996); [27] Sluse et al. (2008); [28] Inada et al. (2006).

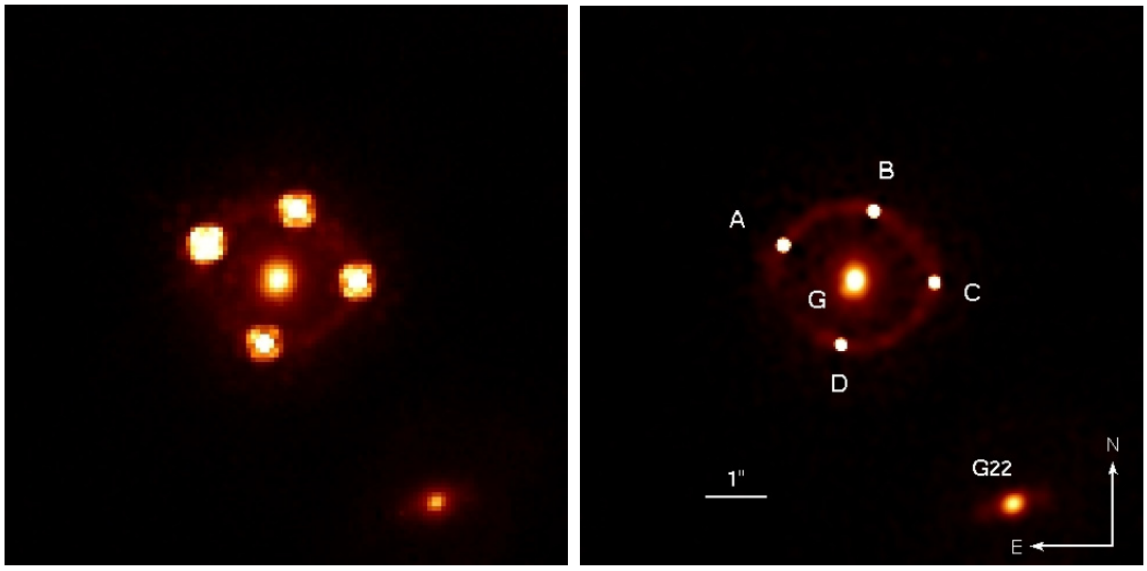

Figure 5.3: *Left:* HST image of HE 0435−1223. *Right:* Deconvolved image. (Image courtesy: Courbin et al. 2011)

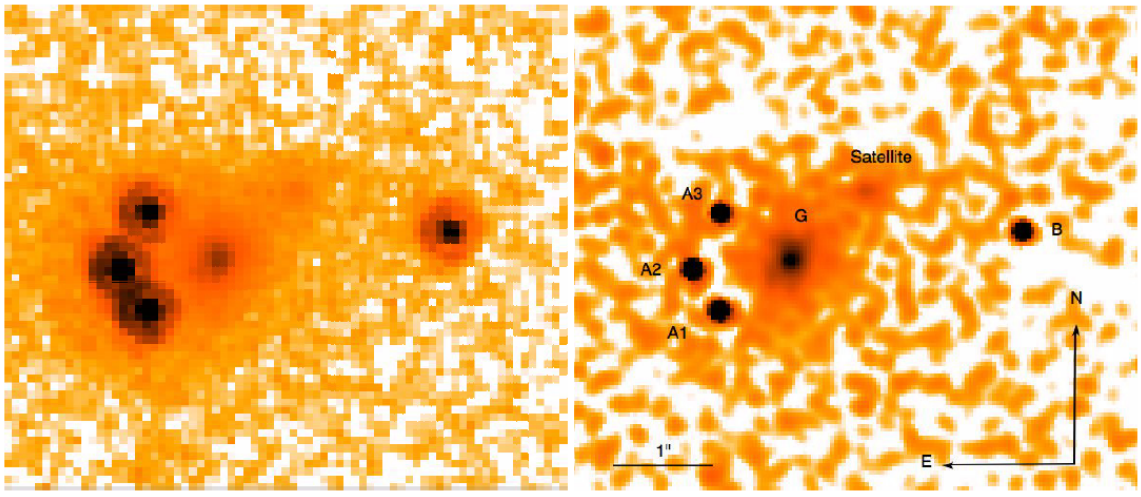

Figure 5.4: *Left:* HST image of RX J0911.4+0551. *Right:* Deconvolved image. (Image courtesy: Sluse et al. 2012)

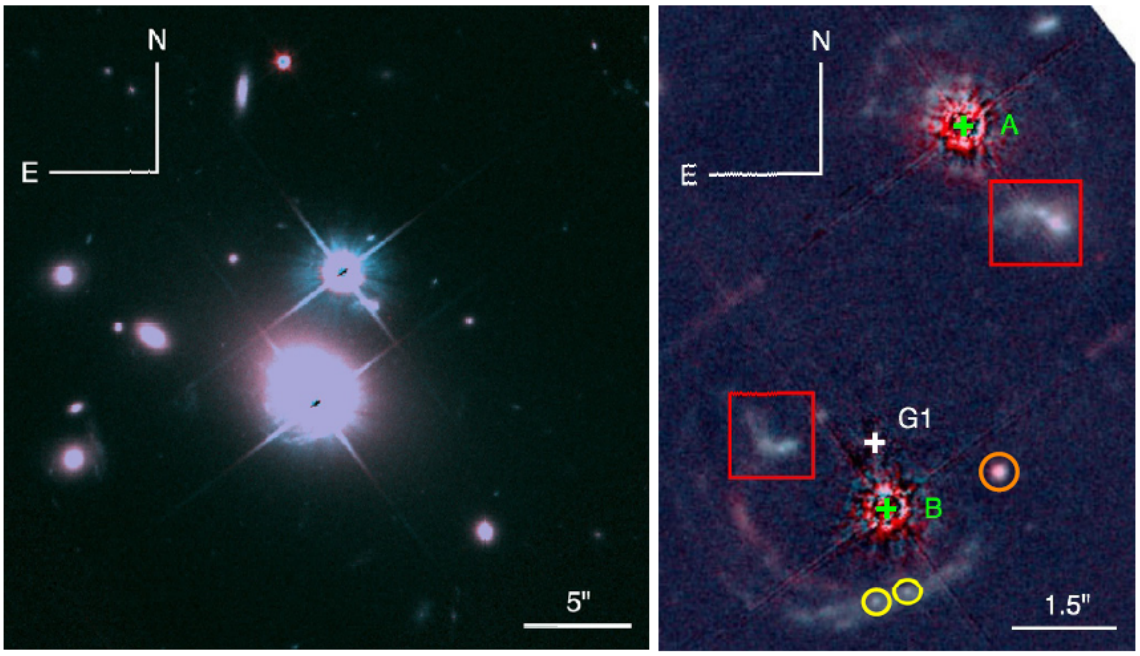

Figure 5.5: *Left:* HST image of Q0957+561. *Right:* Central region after the quasar images and the main lensing galaxy have been subtracted. (Image courtesy: Fadely et al. 2010)

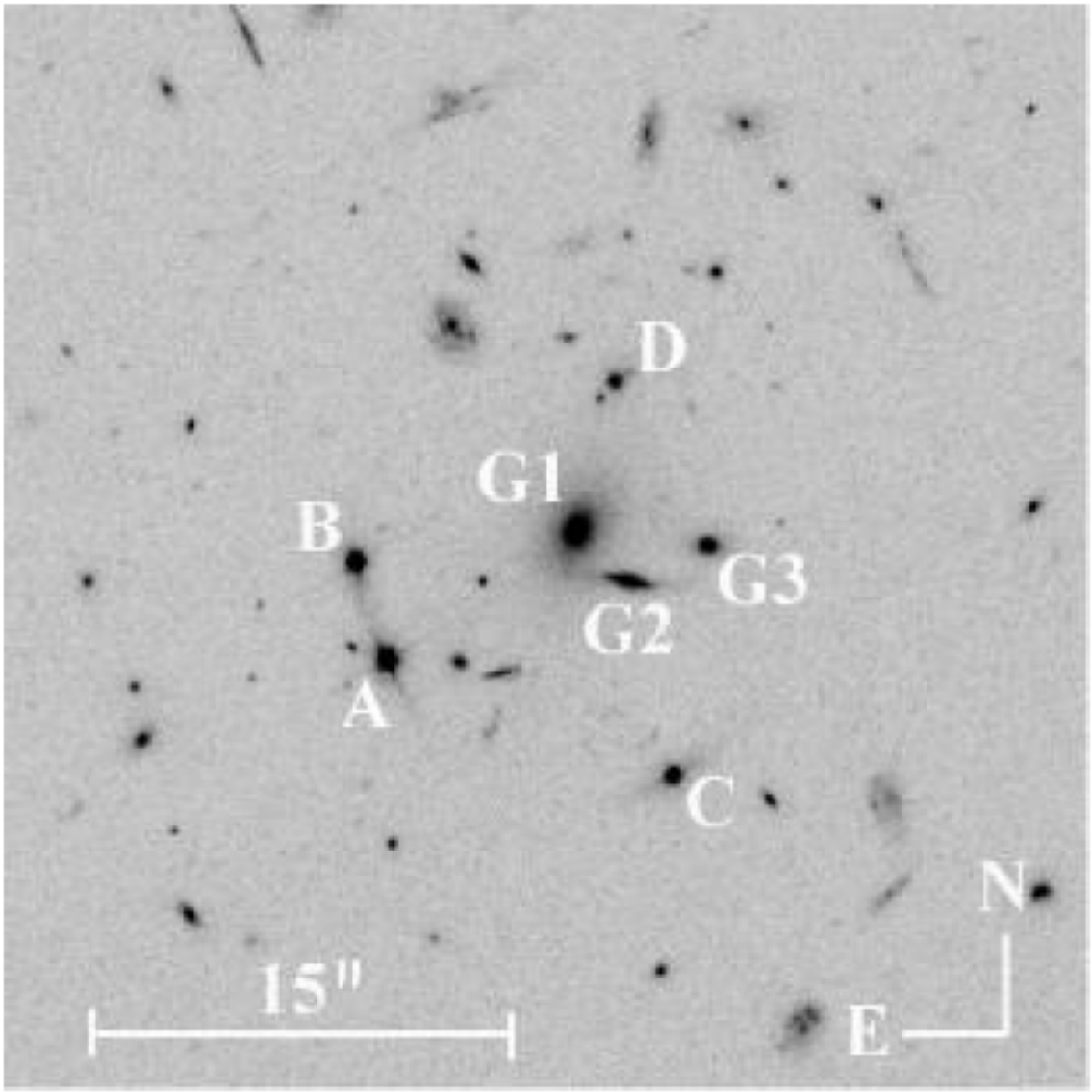

Figure 5.6: HST image of SDSS J1004+4112. (Image courtesy: Inada et al. 2005)

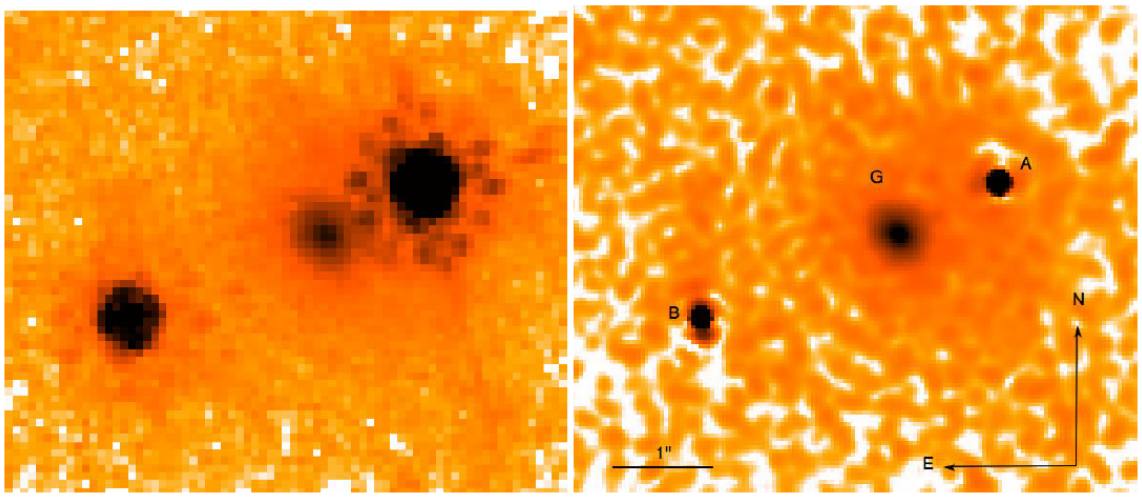

Figure 5.7: *Left:* HST image of HE 1104−1805. *Right:* Deconvolved image. (Image courtesy: Sluse et al. 2012)

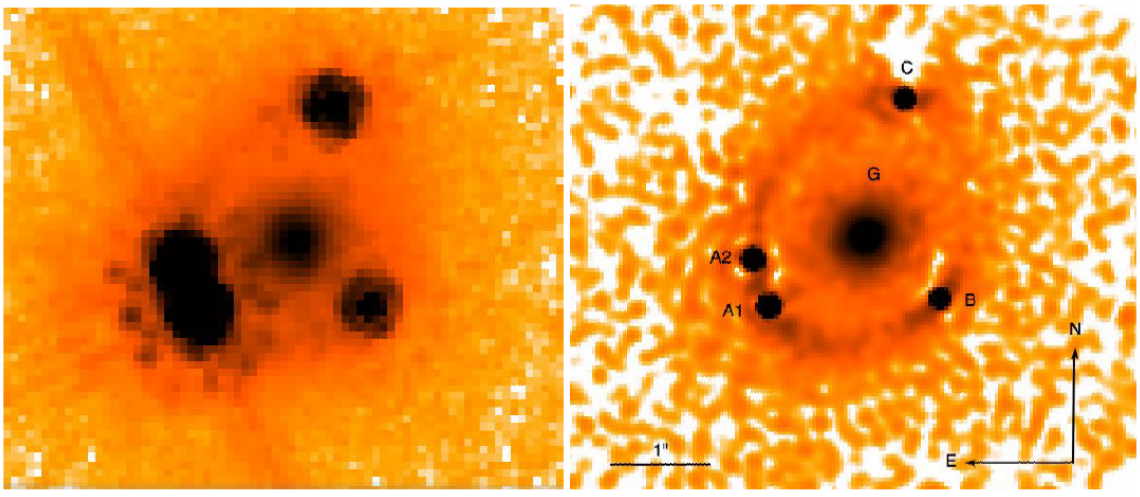

Figure 5.8: *Left:* HST image of PG 1115+080. *Right:* Deconvolved image. (Image courtesy: Sluse et al. 2012)

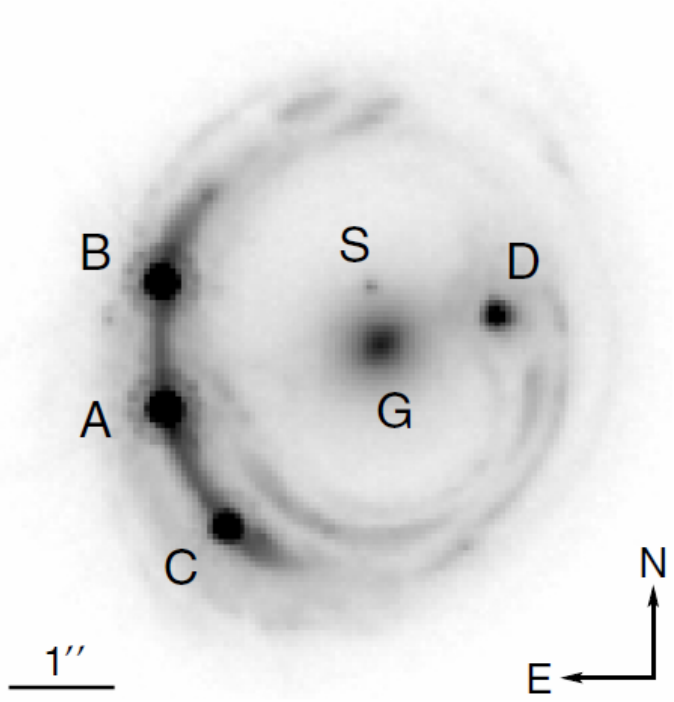

Figure 5.9: HST image of RX J1131−1231. (Image courtesy: Suyu et al. 2013a)

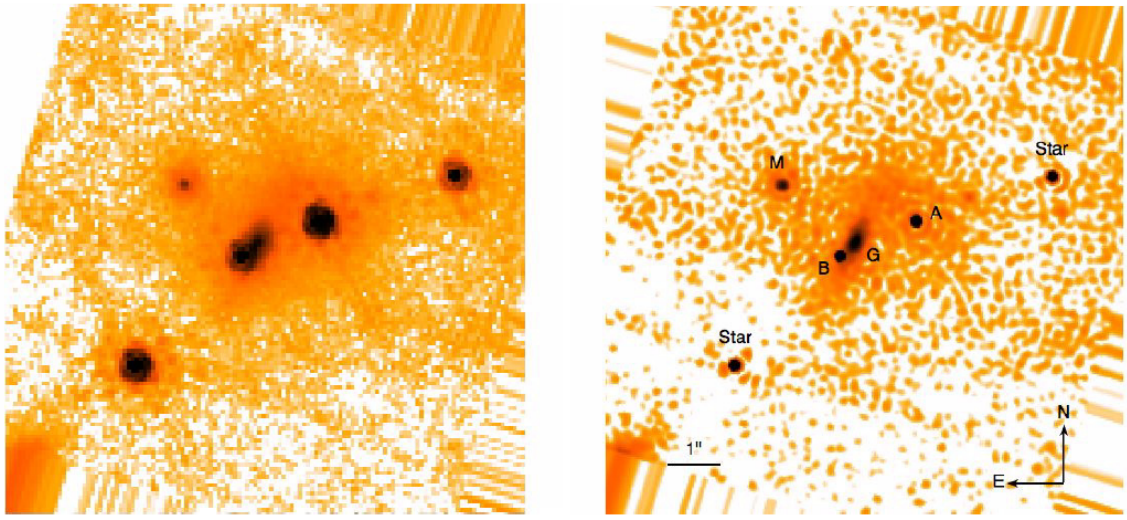

Figure 5.10: *Left:* HST image of SBS 1520+530. *Right:* Deconvolved image. (Image courtesy: Sluse et al. 2012)

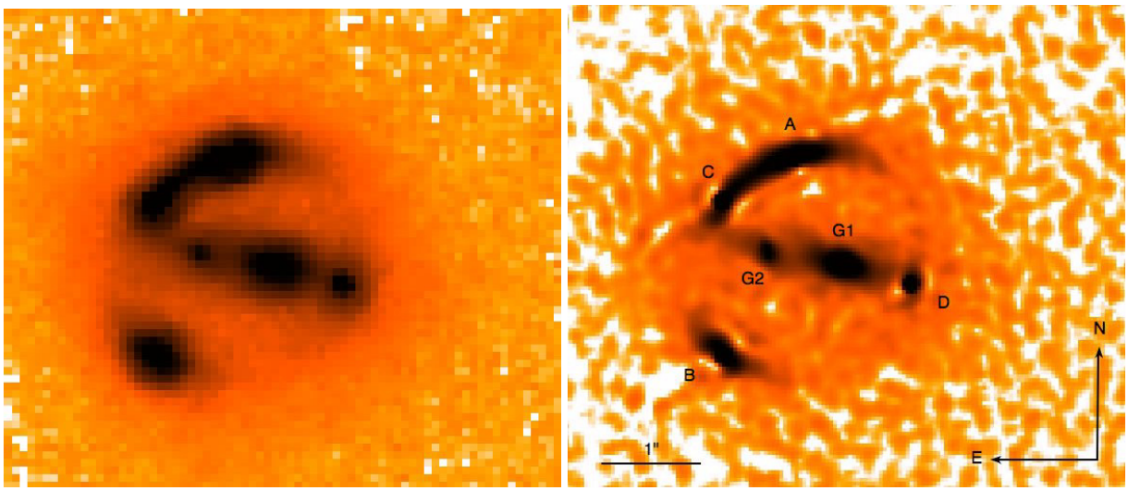

Figure 5.11: *Left:* HST image of CLASS B1608+656. *Right:* Deconvolved image. (Image courtesy: Sluse et al. 2012)

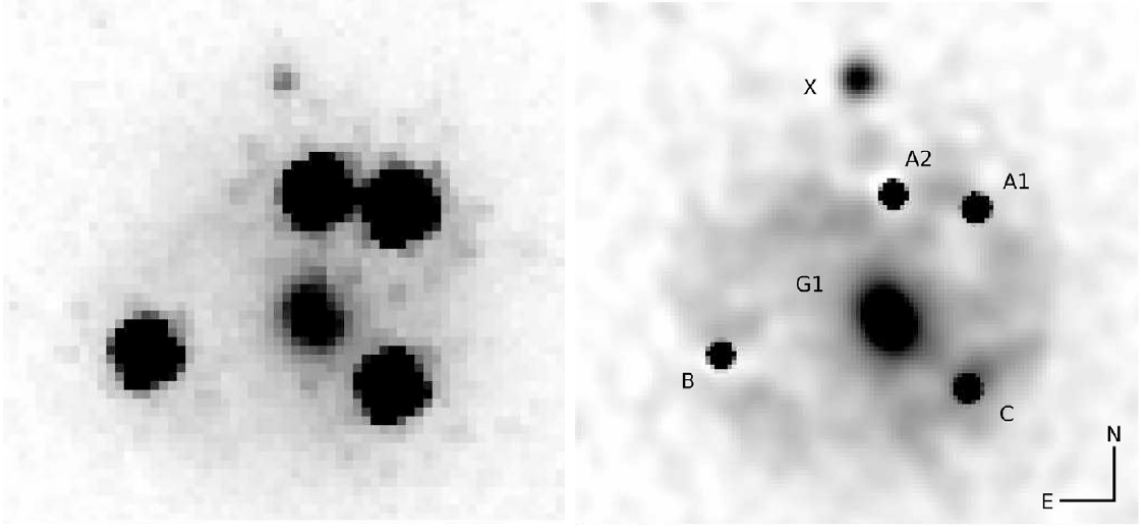

Figure 5.12: *Left:* HST image of WFI J2033−4723. *Right:* Deconvolved image. (Image courtesy: Vuissoz et al. 2008)

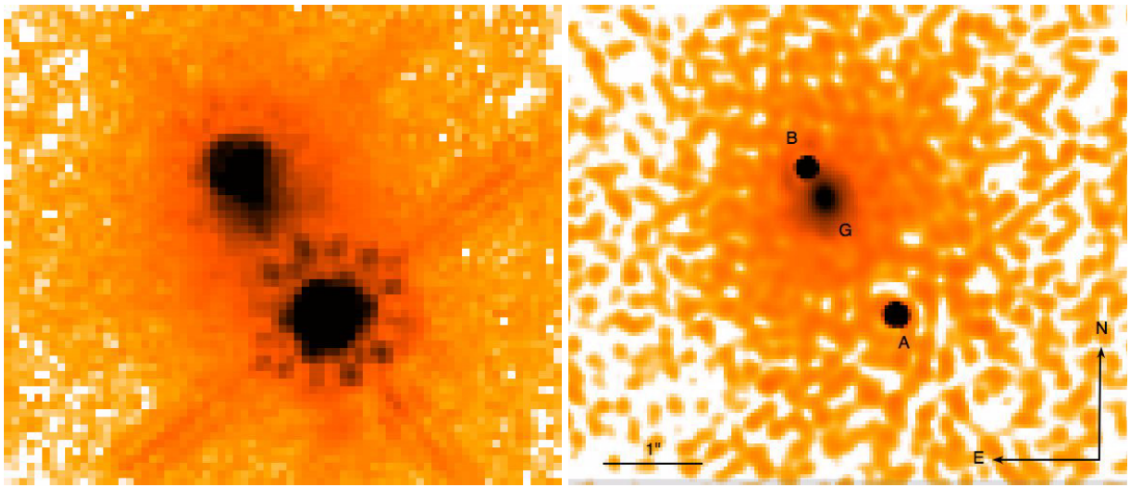

Figure 5.13: *Left:* HST image of HE 2149−2745. *Right:* Deconvolved image. (Image courtesy: Sluse et al. 2012)

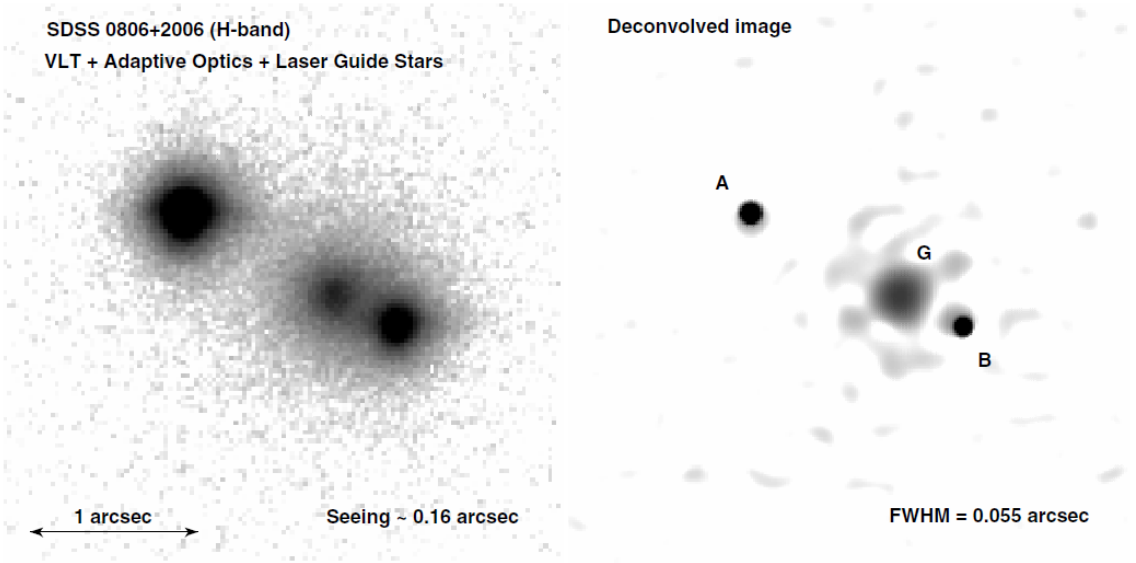

Figure 5.14: *Left:* VLT image of SDSS J0806+2006 taken with adaptive optics. *Right:* Deconvolved image. (Image courtesy: Sluse et al. 2008)

Chapter 6

Conclusion and Future prospects

Estimates of H_0, the current expansion rate of the universe, now available in literature cover a wide range of uncertainties from $\sim$2% to $\sim$10% and the values range between 60 and 75 km s^{-1} Mpc^{-1}. These are estimates found using different methods as outlined in Chapter 1. It has emerged recently (Suyu et al. 2012) that a measurement of H_0 to 1% precision and accuracy, which can provide good constraints on dark energy, spatial curvature of the universe, neutrino physics, etc., with proper accounting of random and systematic errors is within reach for several methods. It has recently been demonstrated that it is possible to measure the time-delay distance to $\sim$5% for a single lens system (Suyu et al. 2010) and that in future it is possible to bring down this error by studying more number of time delay lenses (Suyu et al. 2012). The main motivation of the present work is to (i) measure accurate time delays for a sample of lenses and (ii) consequently estimate H_0 using improved time delay estimates.

The observational strategy followed in this work is to get good quality lightcurves with dense temporal sampling for two gravitationally lensed quasars. The observations used in this work come from four different telescopes, however, all the observations were analysed following a uniform procedure. The major findings of this work are given in the sections below.

6.1 Time delay of SDSS J1001+5027

In Rathna Kumar et al. (2013), we presented the full COSMOGRAIL light curves for the two images of the gravitationally lensed quasar SDSS J1001+5027. The final data, all taken in the R band, totalize 443 observing epochs, with a mean temporal sampling of 3.8 days, from the end of 2004 to mid-2011. The COSMOGRAIL monitoring campaign for SDSS J1001+5027 is no longer in progress. It involved three different telescopes with diameters

from 1.2 m to 2 m, hence illustrating the effectiveness of small telescopes in conducting long-term projects with potentially high impact on cosmology.

We analyzed our light curves with five different numerical techniques, including the three methods described in Tewes et al. (2013a). In addition, we introduced and described a new additional method, based on representing the extrinsic variability by a smoothed version of the difference light curve between the quasar images. Finally, we also presented results obtained via the technique of Hojjati et al. (2013), based on modeling of the quasar and microlensing variations using Gaussian processes. The technique was *blindly* applied to the data by the authors of Hojjati et al. (2013), without any prior knowledge of the results obtained with the other four methods.

Aside from the dispersion-like technique, dominated by systematic errors, we find that the four other methods yield similar time-delay values and similar random and systematic error bars. Our final estimate of the time delay is taken as the mean of these four best results, together with the mean of their uncertainties: $\Delta t_{\rm AB} = -119.3 \pm 3.3$ days, with image A leading image B. This is a relative uncertainty of 2.8%, including systematic errors.

The present time-delay measurement can be used in combination with lens models to constrain cosmological parameters, in particular the Hubble parameter H_0 and the curvature Ω_k (e.g., Suyu et al. 2013a). The accuracy reached on cosmology with SDSS J1001+5027 alone or in combination with other lenses, will rely on the availability of follow-up observations to measure: (1) the lens velocity dispersion, (2) the mass contribution of intervening objects along the line of sight, and (3) the detailed structure of the lensed host galaxy of the quasar.

6.2 Time delay of SDSS J0806+2006

In Chapter 3, we present the light curves of SDSS J0806+2006 using data obtained from September 2007 till April 2012 using two different telescopes: the 2.0-m LRT and the 2.0-m HCT. These measurements are available for this source for the first time. The light curves constitute 153 independent epochs, with a mean sampling interval of about a week. Using the difference-smoothing technique, we measured a time delay of $\Delta t_{\rm AB} = -54.2 \pm 6.8$ days (1σ uncertainty, 12.5% precision), with image A leading image B. The uncertainty was estimated using simulated light curves having known time delays in a plausible range around the measured time delay. A new recipe for creating such simulated light curves is also presented in this thesis.

6.3 H_0 from well measured time-delay lenses

We have presented a homogeneous curve-shifting analysis of the light curves of 24 gravitationally lensed quasars for which time delays have been reported in the literature till date. Time delays were measured using the difference-smoothing technique and their uncertainties were estimated using realistic simulated light curves, a recipe for creating which was introduced in this thesis, having known time delays in a plausible range around the measured delay. We identified 18 systems to be having light curves of sufficiently good quality to enable the measurement of at least one time delay between the images, adjacent to each other in terms of arrival-time order, to a precision of better than 33.3% (including systematic errors). In addition to these 18 systems, we have SDSS J0806+2006 for which a new time delay measurement is presented in this thesis.

Of those 19 systems in total, we performed pixellated mass modelling using the publicly-available PixeLens software for 12 of them, which have known lens redshifts, accurate astrometric information and sufficiently simple mass distribution. We infer the value of H_0 to be 72.1 ± 5.7 km s^{-1} Mpc^{-1} (1σ uncertainty, 7.9% precision) for a spatially flat universe having $\Omega_m = 0.3$ and $\Omega_\Lambda = 0.7$. This matches well with a recent estimate of $H_0 = 69.0 \pm 6$ (stat.) ± 4 (syst.) km s^{-1} Mpc^{-1} found by (Sereno & Paraficz 2014) using a method based on free-form modelling of 18 gravitational lens systems. Our value is also consistent with the recent measurements of H_0 by Riess et al. (2011) and Freedman et al. (2012), however it has lower precision. Increasing the number of lensed systems with good quality light curves from the current 12 used in this study, can bring down the uncertainty in H_0.

In future such high precision time delays will become available from COSMOGRAIL and the International Liquid Mirror Telescope (ILMT; Sagar et al. 2012; Poels et al. 2012) project. Also, next generation cosmic surveys such as the Dark Energy Survey (DES), the Large Synoptic Survey Telescope (LSST; Ivezic et al. 2008) and the Euclid mission will detect a large sample of lenses and time delays might be available for a large fraction of them and consequently enabling measurement of H_0 to an accuracy better than 2%. Further, detection of gravitational wave signal from short gamma-ray bursts associated with neutron star binary mergers in the coming decade could constrain H_0 to better than 1% (Nissanke et al. 2013).

6.4 Future prospects

It is clear from this work that estimate of H_0 based on strong lensing time delays is currently limited by the small sample of lensed quasars with accurate delays. However, by the end of this decade, the situation is expected to change with both the availability of a large sample of gravitationally lensed quasars with time delays from the Large Synoptic Survey Telescope (LSST) (Treu et al. 2013) and improvements in mass modelling techniques. The availability of good time series data on a large number of lensed sytems in the future is also going to be complemented by good time delay estimation techniques. There is already an initiative in this direction as can be seen in "Strong lens time delay challenge" Dobler et al. (2013). I plan to contribute to the above initiative in addition to continuing the monitoring program.

Bibliography

Alexander, T. 1997, in Astrophysics and Space Science Library, Vol. 218, Astronomical Time Series, ed. D. Maoz, A. Sternberg, & E. M. Leibowitz, 163

Auger, M. W., Fassnacht, C. D., Wong, K. C., et al. 2008, ApJ, 673, 778

Bade, N., Siebert, J., Lopez, S., Voges, W., & Reimers, D. 1997, A&A, 317, L13

Barnabè, M., Czoske, O., Koopmans, L. V. E., Treu, T., & Bolton, A. S. 2011, MNRAS, 415, 2215

Bertin, E. & Arnouts, S. 1996, A&AS, 117, 393

Burud, I., Courbin, F., Magain, P., et al. 2002a, A&A, 383, 71

Burud, I., Hjorth, J., Courbin, F., et al. 2002b, A&A, 391, 481

Burud, I., Hjorth, J., Jaunsen, A. O., et al. 2000, ApJ, 544, 117

Chang, K. & Refsdal, S. 1979, Nature, 282, 561

Chavushyan, V. H., Vlasyuk, V. V., Stepanian, J. A., & Erastova, L. K. 1997, A&A, 318, L67

Cohen, A. S., Hewitt, J. N., Moore, C. B., & Haarsma, D. B. 2000, ApJ, 545, 578

Courbin, F., Chantry, V., Revaz, Y., et al. 2011, A&A, 536, A53

Courbin, F., Saha, P., & Schechter, P. L. 2002, in Lecture Notes in Physics, Berlin Springer Verlag, Vol. 608, Gravitational Lensing: An Astrophysical Tool, ed. F. Courbin & D. Minniti, 1

Dobler, G., Fassnacht, C., Treu, T., et al. 2013, ArXiv e-prints

Edelson, R. A. & Krolik, J. H. 1988, ApJ, 333, 646

Efstathiou, G. & Bond, J. R. 1999, MNRAS, 304, 75

Eigenbrod, A., Courbin, F., & Meylan, G. 2007, A&A, 465, 51

Eigenbrod, A., Courbin, F., Meylan, G., Vuissoz, C., & Magain, P. 2006, A&A, 451, 759

Eulaers, E., Tewes, M., Magain, P., et al. 2013, A&A, 553, A121

Fadely, R., Keeton, C. R., Nakajima, R., & Bernstein, G. M. 2010, ApJ, 711, 246

Fassnacht, C. D., Pearson, T. J., Readhead, A. C. S., et al. 1999, ApJ, 527, 498

Fassnacht, C. D., Womble, D. S., Neugebauer, G., et al. 1996, ApJ, 460, L103

Fassnacht, C. D., Xanthopoulos, E., Koopmans, L. V. E., & Rusin, D. 2002, ApJ, 581, 823

Fohlmeister, J., Kochanek, C. S., Falco, E. E., Morgan, C. W., & Wambsganss, J. 2008, ApJ, 676, 761

Fohlmeister, J., Kochanek, C. S., Falco, E. E., et al. 2007, ApJ, 662, 62

Fohlmeister, J., Kochanek, C. S., Falco, E. E., et al. 2013, ApJ, 764, 186

Freedman, W. L. & Madore, B. F. 2010, ARA&A, 48, 673

Freedman, W. L., Madore, B. F., Gibson, B. K., et al. 2001, ApJ, 553, 47

Freedman, W. L., Madore, B. F., Scowcroft, V., et al. 2012, ApJ, 758, 24

Goicoechea, L. J. & Shalyapin, V. N. 2010, ApJ, 708, 995

Goicoechea, L. J., Shalyapin, V. N., Koptelova, E., et al. 2008, New A, 13, 182

Hainline, L. J., Morgan, C. W., MacLeod, C. L., et al. 2013, ApJ, 774, 69

Hinshaw, G., Larson, D., Komatsu, E., et al. 2013, ApJS, 208, 19

Hjorth, J., Burud, I., Jaunsen, A. O., et al. 2002, ApJ, 572, L11

Hojjati, A., Kim, A. G., & Linder, E. V. 2013, Phys. Rev. D, 87, 123512

Howell, S. B. 2006, Handbook of CCD Astronomy, ed. R. Ellis, J. Huchra, S. Kahn, G. Rieke, & P. B. Stetson

Inada, N., Oguri, M., Becker, R. H., et al. 2006, AJ, 131, 1934

Inada, N., Oguri, M., Keeton, C. R., et al. 2005, PASJ, 57, L7

Inada, N., Oguri, M., Pindor, B., et al. 2003, Nature, 426, 810

Inada, N., Oguri, M., Shin, M.-S., et al. 2012, AJ, 143, 119

Ivezic, Z., Tyson, J. A., Acosta, E., et al. 2008, ArXiv e-prints

Jakobsson, P., Hjorth, J., Burud, I., et al. 2005, A&A, 431, 103

Kneib, J.-P., Cohen, J. G., & Hjorth, J. 2000, ApJ, 544, L35

Koopmans, L. V. E., de Bruyn, A. G., Xanthopoulos, E., & Fassnacht, C. D. 2000, A&A, 356, 391

Koptelova, E., Chen, W. P., Chiueh, T., et al. 2012, A&A, 544, A51

Lehar, J., Hewitt, J. N., Burke, B. F., & Roberts, D. H. 1992, ApJ, 384, 453

Lidman, C., Courbin, F., Kneib, J.-P., et al. 2000, A&A, 364, L62

Linder, E. V. 2011, Physical Review D, 84, 123529

Lovell, J. E. J., Jauncey, D. L., Reynolds, J. E., et al. 1998, ApJ, 508, L51

Lucy, L. B. 1974, AJ, 79, 745

Magain, P., Courbin, F., & Sohy, S. 1998, ApJ, 494, 472

Meylan, G., Courbin, F., Lidman, C., Kneib, J.-P., & Tacconi-Garman, L. E. 2005, A&A, 438, L37

Morgan, N. D., Caldwell, J. A. R., Schechter, P. L., et al. 2004, AJ, 127, 2617

Morgan, N. D., Kochanek, C. S., Pevunova, O., & Schechter, P. L. 2005, AJ, 129, 2531

Myers, S. T., Fassnacht, C. D., Djorgovski, S. G., et al. 1995, ApJ, 447, L5

Narayan, R. & Bartelmann, M. 1996, ArXiv Astrophysics e-prints

Narayan, R. & Nityananda, R. 1986, ARA&A, 24, 127

Nissanke, S., Holz, D. E., Dalal, N., et al. 2013, ArXiv e-prints

Oguri, M., Inada, N., Hennawi, J. F., et al. 2005, ApJ, 622, 106

Oguri, M., Inada, N., Keeton, C. R., et al. 2004, ApJ, 605, 78

Oguri, M., Schrabback, T., Jullo, E., et al. 2013, MNRAS, 429, 482

Paraficz, D. & Hjorth, J. 2010, ApJ, 712, 1378

Paraficz, D., Hjorth, J., Burud, I., Jakobsson, P., & Elíasdóttir, Á. 2006, A&A, 455, L1

Patnaik, A. R. & Narasimha, D. 2001, MNRAS, 326, 1403

Pelt, J., Kayser, R., Refsdal, S., & Schramm, T. 1996, A&A, 305, 97

Penzias, A. A. & Wilson, R. W. 1965, ApJ, 142, 419

Planck Collaboration. 2013, ArXiv e-prints

Poels, J., Borra, E., Hickson, P., et al. 2012, in IAU Symposium, Vol. 285, IAU Symposium, ed. E. Griffin, R. Hanisch, & R. Seaman, 394–396

Poindexter, S., Morgan, N., Kochanek, C. S., & Falco, E. E. 2007, ApJ, 660, 146

Rathna Kumar, S., Tewes, M., Stalin, C. S., et al. 2013, A&A, 557, A44

Refsdal, S. 1964, MNRAS, 128, 307

Reid, M. J., Braatz, J. A., Condon, J. J., et al. 2013, ApJ, 767, 154

Richardson, W. H. 1972, Journal of the Optical Society of America (1917-1983), 62, 55

Riess, A. G., Macri, L., Casertano, S., et al. 2011, ApJ, 730, 119

Riess, A. G., Macri, L., Casertano, S., et al. 2009, ApJ, 699, 539

Rowan-Robinson, M. 2008, Astronomy and Geophysics, 49, 030000

Sagar, R., Kumar, B., Omar, A., & Pandey, A. K. 2012, in Society of Photo-Optical Instrumentation Engineers (SPIE) Conference Series, Vol. 8444, Society of Photo-Optical Instrumentation Engineers (SPIE) Conference Series

Saha, P., Coles, J., Macciò, A. V., & Williams, L. L. R. 2006, ApJ, 650, L17

Saha, P. & Williams, L. L. R. 2003, AJ, 125, 2769

Saha, P. & Williams, L. L. R. 2004, AJ, 127, 2604

Schneider, P. & Sluse, D. 2013a, A&A, 559, A37

Schneider, P. & Sluse, D. 2013b, ArXiv e-prints

Sereno, M. & Paraficz, D. 2014, MNRAS, 437, 600

Shalyapin, V. N., Goicoechea, L. J., & Gil-Merino, R. 2012, A&A, 540, A132

Skilling, J. & Bryan, R. K. 1984, MNRAS, 211, 111

Sluse, D., Chantry, V., Magain, P., Courbin, F., & Meylan, G. 2012, A&A, 538, A99

Sluse, D., Courbin, F., Eigenbrod, A., & Meylan, G. 2008, A&A, 492, L39

Sluse, D., Surdej, J., Claeskens, J.-F., et al. 2003, A&A, 406, L43

Smette, A., Robertson, J. G., Shaver, P. A., et al. 1995, A&AS, 113, 199

Sunyaev, R. A. & Zeldovich, Y. B. 1970, *Astrophys. Spa. Sci.,* , 7, 3

Suyu, S. H., Auger, M. W., Hilbert, S., et al. 2013a, ApJ, 766, 70

Suyu, S. H., Marshall, P. J., Auger, M. W., et al. 2010, ApJ, 711, 201

Suyu, S. H., Treu, T., Blandford, R. D., et al. 2012, ArXiv e-prints

Suyu, S. H., Treu, T., Hilbert, S., et al. 2013b, ArXiv e-prints

Tewes, M., Courbin, F., & Meylan, G. 2013a, A&A, 553, A120

Tewes, M., Courbin, F., Meylan, G., et al. 2012, The Messenger, 150, 49

Tewes, M., Courbin, F., Meylan, G., et al. 2013b, A&A, 556, A22

Tonry, J. L. 1998, AJ, 115, 1

Treu, T., Marshall, P. J., Cyr-Racine, F.-Y., et al. 2013, arXiv:1306.1272

Tsvetkova, V. S., Vakulik, V. G., Shulga, V. M., et al. 2010, MNRAS, 406, 2764

Vuissoz, C., Courbin, F., Sluse, D., et al. 2008, A&A, 488, 481

Vuissoz, C., Courbin, F., Sluse, D., et al. 2007, A&A, 464, 845

Walsh, D., Carswell, R. F., & Weymann, R. J. 1979, Nature, 279, 381

Wambsganss, J. 1998, Living Reviews in Relativity, 1

Weymann, R. J., Latham, D., Roger, J., et al. 1980, Nature, 285, 641

Wisotzki, L., Koehler, T., Lopez, S., & Reimers, D. 1996, A&A, 315, L405

Wisotzki, L., Schechter, P. L., Bradt, H. V., Heinmüller, J., & Reimers, D. 2002, A&A, 395, 17